UNDERSTANDING AND CONTROLLING THE HELICAL NANOFILAMENT PHASE OF BENT-CORE MESOGENS

By

Lee Michel Foley

B.S. Chemistry Metropolitan State University of Denver, 2014

A thesis submitted to the

Faculty of the Graduate School of the

University of Colorado in partial fulfillment

of the requirement for the degree of

Doctor of Philosophy

Department of Chemistry

2019

This thesis entitled:

Understanding and Controlling the Helical Nanofilament Phase of Bent-Core Mesogens

written by Lee Michel Foley

has been approved for the Department of Chemistry

_____

Professor David M. Walba

_____

Professor Matthew Glaser

Date_____

The final copy of this thesis has been examined by the signatories, and we find that both the content and the form meet acceptable presentation standards of scholarly work in the above-mentioned discipline.

Foley, Lee M. (PhD, Chemistry)

Understanding and Controlling the Helical Nanofilament Phase of Bent-Core Mesogens

Thesis directed by Professor David M. Walba

The helical nanofilament (HNF) phase of bent-core liquid crystals (BLCs) is an exotic mesophase characterized by the spontaneous formation of twisted crystalline nanoscale filaments, approximately 30 nm in width, that can extend for microns in length. The unique characteristics of HNFs including: crystallinity, porosity, ability to be aligned, and extremely large aspect ratio, lend this phase to application in next generation organic electronics, including photovoltaic (PV) systems. Effectively functioning as nanoscale wires, the morphology of this phase provides an excellent interface for charge separation, and potentially provides a path to obtain high charge carrier mobility. To be used successfully as the active layer in a PV device, the filaments need to absorb a significant portion of the solar spectrum – a characteristic that has not yet been realized for any known HNF forming materials. The work in this thesis describes three projects developed to address this issue by attempting to expand the structure space of the HNF phase, and to improve our fundamental understanding of the nature of this phase. The first project involves the incorporation of the azulene chromophore into the structural backbone of known HNF forming compounds to probe the structure space of the phase while incorporating the desired absorbances needed for PV device application. The second project involves exploring the possibility of direct chemical modification of the HNF surface without destroying the filament structure. Finally, the third project describes an investigation into the effect nanoconfinement has on a closely related phase, the low temperature dark conglomerate (DC) phase. From these three projects a new azulene derived “bend unit” for BLCs was developed, a gel phase reaction to attach functional molecules to the HNF surface was created, and the first example of the DC phase adopting the HNF morphology using nanoconfinement is reported.

This work is dedicated to my mom Jan L. Foley,

my dad Patrick M. Foley, and my brother Wyatt P. Foley

without whom my curiosity and desire to understand our physical world

would have never existed.

There are a few people that I owe my graduate career to, Prof. David M. Walba my thesis advisor, Prof. Ethan Tsai my friend and undergraduate advisor, and Dr. Richard Shoemaker my friend and boss during my time in the NMR facility. Prof. Walba graciously accepted me into his research lab as an undergraduate during my time as an NSF REU fellow, and my research career into materials science at a major research university began. Upon completion of my undergraduate studies, he again accepted me into his group as a graduate student and gave me free reign over my project allowing me to develop my scientific creativity, and for that, I am incredibly grateful.

Prof. Tsai taught me everything I know about organic synthesis both on paper and in practice. From his expertise, I was taught many synthetic techniques few undergraduates would get to learn, and I think this gave me an advantage when I began my graduate career. Additionally, his friendship and guidance helped to develop me as an individual. All of the times fly fishing, rock climbing, and grilling will never be forgotten, and I will also never forget the times at conferences we spent together, especially the Gordon Conference on Liquid Crystals in 2015 where given a particular set of circumstances “It’s bad, it’s real bad” was one of the funniest things I have ever witnessed.

I was fortunate enough to get to work with Dr. Richard Shoemaker for one of the three years I worked as the graduate student assistant for the departmental NMR facility. During our time together, Rich showed me the incredible power of an NMR spectrometer which is easily one of the most complicated pieces of equipment ever developed. He also taught me the importance of attention to detail and the importance of doing a job correctly through his unmatched work ethic. Without his influence, Cindy and I would not have been able to keep the NMR facility running for ten months after he left CU. Rich is one of the most selfless people I have ever met, and I hope to emulate his character in my future endeavors. Listening to his band play blues rock, doing liquid helium fills, troubleshooting spectrometer issues, and enjoying craft beers with him will always be some of my favorite memories from graduate school, and I am forever indebted to him for all of his help.

Table of Contents

List of Figures

1 Fundamentals of Liquid Crystals and the HNF Phase

1.1 Introduction

Perhaps surprising to a new researcher in the field, liquid crystals are commonly found throughout nature and, in fact, may have been involved in the origin of life here on Earth.[1] If an organic chemist were to randomly synthesize materials, it is estimated that about one in every 200 would possess some type of liquid crystalline phase.[2] From their discovery in 1888 by Friedrich Reinitzer, these materials have proven to be fundamental in understanding our physical world and currently provide the platform by which almost all information is displayed. Largely constructed of organic materials, liquid crystals are quite amenable to a variety of applications and, recently, focus has centered on using these materials in a variety of novel electronics. Electronic devices that are comprised of organic materials have the potential to be produced more cheaply, made flexible, wearable, and biocompatible. As such, they provide access to technology where it would otherwise be inaccessible and fill application voids where inorganic materials fall short.

The work reported in this thesis covers efforts made and progress towards application of the helical nanofilament (HNF) phase of bent-core liquid crystals in organic solar cells and other functional nanoscale systems. Since no known HNF forming material significantly absorbs visible-light, the goal was to develop a new series of materials that have the desired absorbance properties while maintaining the formation of the HNF phase. Described are three projects that address the issue of the small structure space of the phase as the first step towards the realization of visible-light absorbing HNFs and their nanoscale application.

1.2 LC Phases

To better understand the world of liquid crystals, we should first understand what it is meant by the term “phase” when used in the context of a phase of matter. A phase of matter is a state in which a

substance exists that is physically uniform throughout and possesses definite, abrupt boundaries that distinguish it from other states of matter. These states are differentiated from one another by the way the matter organizes through varying degrees of orientational and positional order which is described by symmetry. In an isotropic fluid (as well as a gas), the molecules are free to move throughout the system and have no positional or orientational ordering, resulting in a system with no order (over sufficiently long scales) and high symmetry. In a molecular crystal, however, the molecules are all rigidly held in specific positions and orientations that are dictated by the crystal lattice. As a result, the amount of order in the crystal phase is high and the symmetry low, relative to the other phases for a particular material. For certain materials, called liquid crystals (LCs), there are phases that also exist (forming) between the crystalline solid and isotropic liquid phases. Termed *mesophases* (or more simply LC phases), these phases possess order and symmetries that are intermediate to traditional solids and liquids.

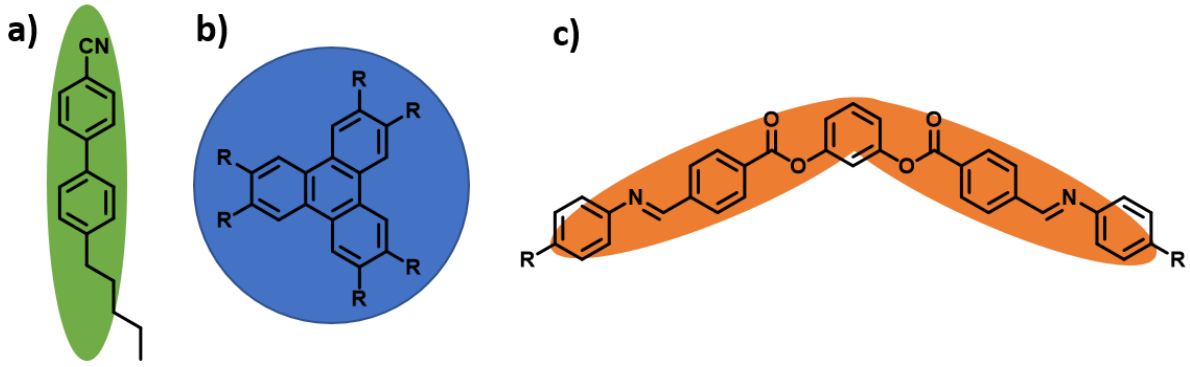

Figure 1.1 - Three common shapes for thermotropic LC molecules. a) calamitic or rod-shaped b) discotic or disk-shaped c) bent-core compounds. For all shapes the molecule is constructed of a rigid aromatic portion (drawn) and a flexible aliphatic tail (shown in [a] and abbreviated 'R' in [b] and [c])

LC phases are broadly classified by the conditions that drive the phase transition which include temperature and solvent concentration. Phase transitions of *thermotropic* LCs are a function of temperature only, while *lyotropic* LCs possess phase transitions that are a function of both temperature and solvent concentration. Both thermotropic and lyotropic LCs possess components that are mutually

exclusive, resulting in the nanoscale segregation of these components. In a thermotropic LC, these components are covalently bound to one another, and are commonly comprised of rigid aromatic cores connected to flexible aliphatic tails (**Figure 1.1**). The frustration between the rigidity and fluidity of these sections, coupled to the anisotropy (defined by a vector called the molecular director, **n**) of the molecular structure promote the formation of mesophases. LC phases exhibit varying degrees of order depending on the nature of the phase being formed, and are strongly influenced by the shape of the molecule. Traditionally, the most common shapes for LC molecules are rod-shaped (calamitic LCs), disc-shaped (discotic LCs), and more recently, bent or banana shaped (bent-core LCs or BLCs). From the perspective of a LC materials scientist, these compounds are approximated by how they behave in the phase and are considered to exist in a statistical distribution of all possible conformations and orientations from which the molecular shape and symmetries are derived. To this end, calamitic compounds are approximated as cylinders, belonging to the $D_{\infty h}$ point group (not to be confused with the symmetries of the molecules themselves itself which are commonly not in the $D_{\infty h}$ point group), with a large aspect ratio and a molecular rotation that is generally free around the long axis of the molecule. The aromatic core of calamitic compounds can be flanked by either one or two flexible tails and the molecular director **n** is parallel to the long axis of the molecule. Discotic compounds are also cylindrical in shape with the same symmetry as a calamitic, however, now the cylinder is considerably wider and flatter (like a disk), and, since they are anisotropic in two dimensions, **n** is perpendicular to the plane of the molecule which contains the aromatic core. BLCs, on the other hand, are defined by an over-all bent shape (like a banana), are traditionally constructed with the aromatic portion located in the central core, and now have two important directors **n** and **b** (shown in Figure 1.3). Due to this bent shape, the symmetry of a BLC is reduced to C_{2v}, and molecular rotation is restricted around **n** resulting in behavior that is significantly different from traditional calamitics. These shapes each possess phases

that are unique, with the calamitic materials being the most widely studied and examples of the most common calamitic phases are discussed below.

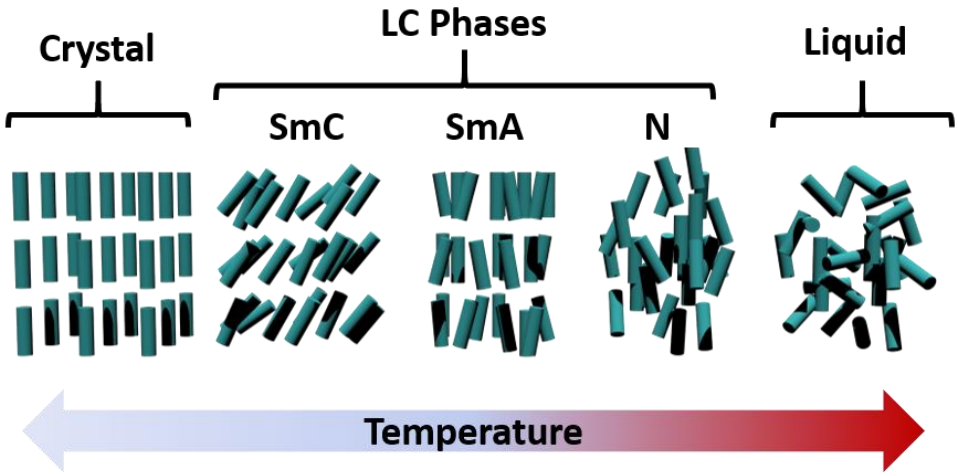

Figure 1.2 - Liquid crystal phases form between the isotropic liquid and crystalline phases. For calamitic compounds (shown here) the phases fall under the category of either nematic phases or smectic phases. The nematic phase (N) is characterized by orientational ordering where the molecules point in the same direction on average, while the smectic phases possess both orientational and positional ordering in the form of stacks of fluid layers. In the smectic A (SmA) phase the molecules are oriented perpendicular to the layer, where in the smectic C (SmC) phase the molecules are tilted at some angle relative to the layer.

The nematic (N) phase of calamitics only possesses orientational order, such that the molecules point in the same direction on average. The smectic phases, however, not only possess this orientational ordering, but also have positional ordering in the form of stacks of fluid layers of molecules and can be categorized as either being orthogonal or tilted, depending on the orientation of the molecules relative to the layer plane. The smectic A (SmA) phase is characterized by the formation of layers in which the molecules are oriented perpendicular to the layer, while the smectic C (SmC) phase is constructed of layers of tilted molecules (**Figure 1.2**). For calamitics, over ten different smectic LC phases have been reported, each with varying degrees of order in the system, and the situation becomes more complicated when a bend is introduced in the linear construction of the calamitic molecule.

1.3 Bent-Core LCs

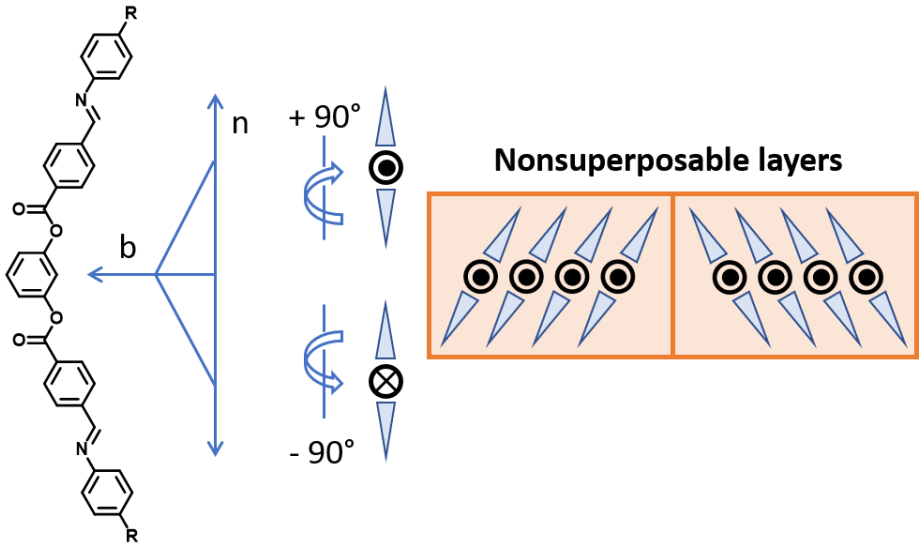

Figure 1.3 - The molecular bend of a BLC results in a polar molecular structure, **n** represents the molecular director and **b** represents the polar director. Rotation of the bent structure 90°in or out of the plane of paper is represented by the dot or cross respectively. Tilted polar molecules that layer can form two nonsuperposable layer structures generating chiral layer structures.

Bent-core liquid crystals (BLCs) are a unique class of LC that tend to behave quite differently from their calamitic counterparts, due to the reduction of symmetry in the molecular structure. BLC compounds are typically made up of a central bend unit flanked by two arms giving the molecule an overall bent structure with the angle of the bend commonly centered around 120°. Traditionally, the bend unit is comprised of a central rigid aromatic core such as resorcinol or the disubstituted 2,7-naphthyl, but more recently central units comprised of alkyl chains with an odd number of methylene units have been employed.[3] Though BLCs should be able to form traditional calamitic phases (such as the SmA and SmC) they commonly form LC phases that are unique to bent-core systems.[3] BLCs have a strong tendency to layer, making most BLC phases smectics, and materials that contain two tails in their molecular structure tend to form tilted smectics (SmC type). The chevron shape of the BLCs restrict the rotation of the molecules around their director, making them inherently polar (**Figure 1.3**). The combination of layering, molecular tilt, and polarity result in the destruction of mirror symmetry within

the layer, giving a chiral layer structure. Thus, BLCs were the first reported compounds to form chiral fluid conglomerates from achiral molecules.[3,4]

1.3.1 Overview of BLC Phases

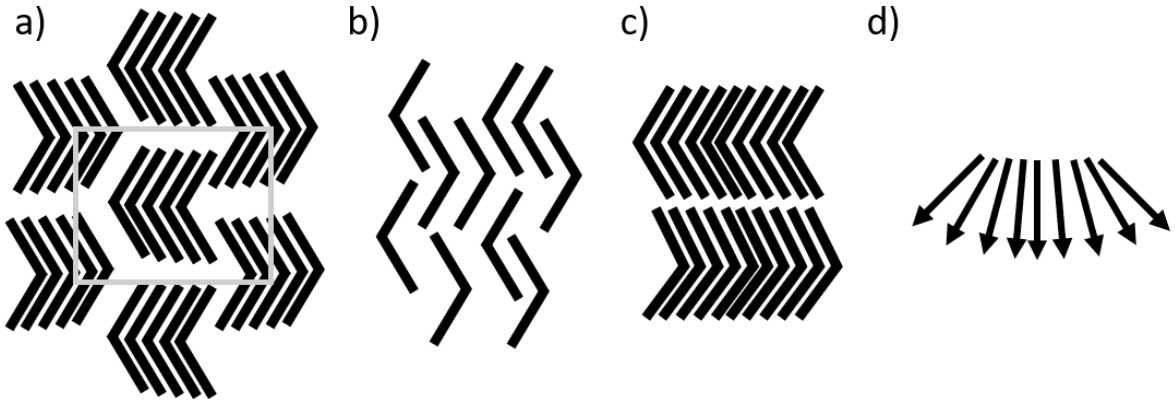

Figure 1.4 – Examples of different packing motifs for BLC materials. (a) columnar phases constructed of fragmented layers. (b) intercalated phases (c) antiferroelectric/ferroelectric layer orientations (d) splay modulated layers (top view of the layer, the arrows indicate the polar director, **b**).

As a result of the bent nature of the BLC molecular structure, BLC phases are largely formed as a response to the steric packing of the molecular bend, and by maximizing the free volume available for the tails to occupy (**Figure 1.4**).[3] To date, more than eight unique BLC phases (historically labeled B1-B8 in the order of their discovery) are known, each with its own defining characteristics.[3] These phases are characterized by how the molecules are packed relative to the smectic layer. Fragmentation of the layers into columns where the polarization direction varies from column to column, is an effective way that the B1 type phases pack (**Figure 1.4**a).[3,5] If the distance between columns becomes sufficiently small, intercalated phases are then realized where the BLC molecules nest within the bend of other neighboring molecules (**Figure 1.4**b).[3] This gives an interdigitated structure where the polar director is distributed randomly and an example of this type of phase is the B6 phase.[3] However, if the molecules have a particularly strong tendency to layer, the polar director can alternate from layer to layer and this orientation makes up certain of the B2 phases (**Figure 1.4**c).[3,4] Another method by which the BLCs pack

to maximize the free volume available to the tails is by splaying the molecules within the layer, similar to how the pages of a book behave when opened (**Figure 1.4**d). These splay modulated phases are labeled as the B7 phases and can have wave-like, undulating layers.[3,6] Additionally, a helical distribution of the layers can be realized by rotating adjacent layers at some arbitrary, but well-defined, angle relative to one another much like the twist-grain boundary (TGB) phase. Helical superstructures have also been observed for certain BLC systems, and have been labeled as the B4 or helical nanofilament (HNF) phase.[3,7]

1.3.2 The HNF Phase

The HNF phase is characterized by the spontaneous formation of crystalline, nanoscale filaments, constructed of twisted smectic layers that have a very large aspect ratio and a surface area that is divided between aromatic layer edges and aliphatic layer ends.[7,8] Typically extending several microns in length, the height and width of the filament is generally 35-50 nm with a helical pitch around 120 nm.[7] Each filament is constructed of five to six layers with the molecules within each layer held in a crystalline environment.[7] Due to the nature of this phase, it is stable down to and below room temperature, and no other known phases have been observed to form below it. The formation of the phase is driven by the orientation of the respective molecular halves as the material crystallizes.[7] Since the molecular halves are covalently bound, the crystallization of the top and bottom halves of the molecules into rectangular lattices that are orthogonal to one another causes a strain within the system that prevents the layer from maintaining a planar configuration (**Figure 1.5**).[7]

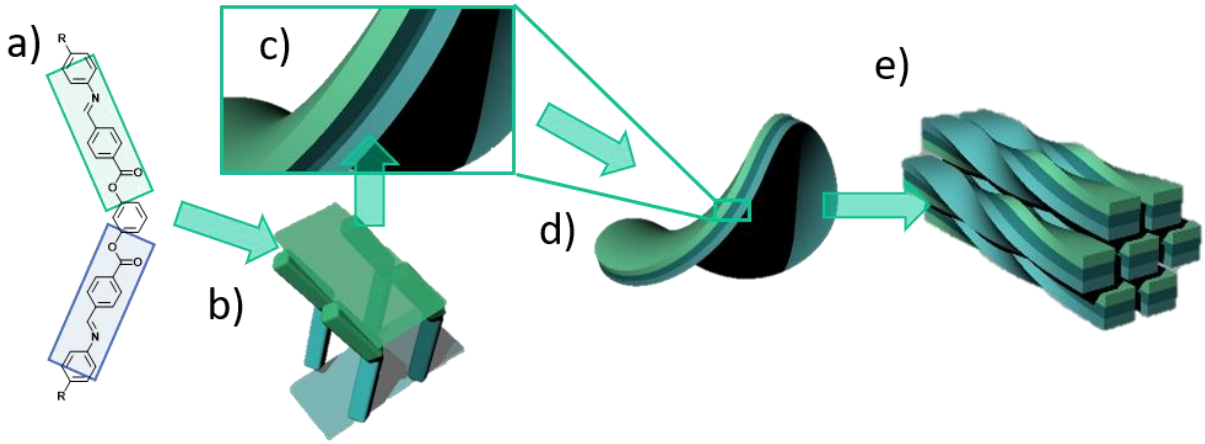

Figure 1.5 – Mechanism for the formation of the HNF phase. a) The top and bottom half of HNF forming materials crystallize in orthogonal lattices (b), causing an elastic strain in the planar layer that is relieved by deformation of the layer into saddles (c,d). These saddles can then stack to form helical filaments (e).

The strain associated with maintaining a planar layer can be relieved, however, if the layers are allowed to deform into saddles. Thus, the underlying layer structure in this system is comprised of hyperbolic paraboloids which are minimal surfaces with purely negative gaussian curvature.[7] The consequence of this is the self-limiting nature of the growth of the filaments in the two directions perpendicular to the filament axis.[9] As the filament nucleus grows and additional layers are added, the purely negative curvature of the hyperbolic paraboloid is lost as the layers become further from the filaments center of mass, resulting in only the central layer having the ideal curvature. This distance from the central layer forces the outer layers to flatten, costing strain energy.[9] As the filament approaches a critical width, the cost in strain energy becomes greater than the cost required to split and form a new surface, resulting in bifurcation of the filament tip and the formation of a new "daughter" filament branching from the parent. This gives filaments of highly uniform dimensions, and this growth mode preserves the chirality of the parent filament yielding conglomerate domains of single-handed filaments that can extend for several square microns.[9] The crystalline and one dimensional characteristics of the HNFs make HNF materials attractive for electronic applications since each

individual filament should effectively function as a nanoscale wire. This would provide an unimpeded path for charge carriers as they move to their respective electrodes.

1.4 Project Overview

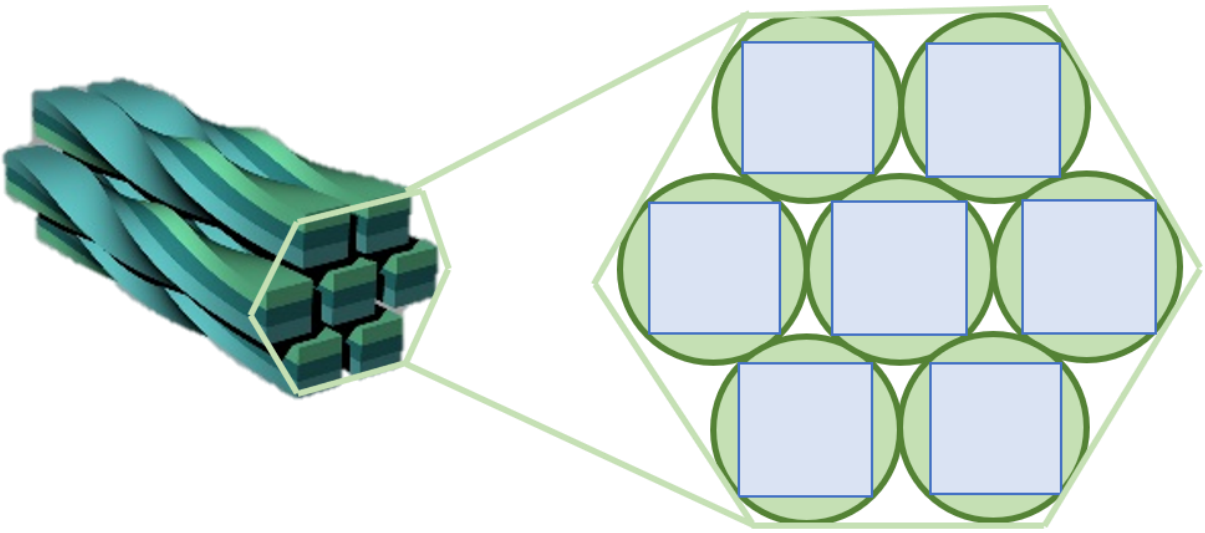

Figure 1.6 – Packing of the HNF phase. The filaments pack like cylinders to form a porous conglomerate. However, due to the square cross-section of the filament, more empty space is present between neighboring filaments than would be expected for pure cylinders.

Organic electronic devices often require features that are robustly maintained on the nanometer and larger length scales, and the nanoscale morphology of the HNF phase provides just that. Studies of the HNF phase led to the realization that the conglomerate structure of the HNF bundles is porous since the filaments are approximately cylinders, which cannot completely fill space. Additionally, since the cross-section of a filament is approximately square, the amount of empty space between the cylinders should be greater than that expected for the purely cylindrical example giving a system that contains a significant amount of empty space (**Figure 1.6**). From this, blends of HNF forming materials and a variety of small molecules and polymers were made to study the behavior of a composite HNF system. What was found was that the filament structure was robustly maintained in a variety of mixtures including mixtures made with C60 and PCBM, which are two common components used in blended bulk heterojunction solar cells.[10] For all of the samples, the second component of the mixture

was nanoconfined to the interstitial areas between the filaments, with no infiltration into the filament structure. Association of the C60's with the aromatic layer edges of the filament surface provides an ideal interface for charge transfer between the filament and the C60. Time-resolved microwave conductivity (TRMC) experiments of the HNF/C60 blends shows a nearly perfect yield of free charge carriers, indicating that the interface is highly efficient at separating charge.[11] Coupling this data with the fact that the HNFs can be aligned over large length scales using a variety of techniques, it was rationalized that the HNF morphology would be an ideal candidate for use as a component of the active layer in an ordered bulk heterojunction (OBHJ) solar cell. Unfortunately, no known HNF forming compounds absorb visible light, so the project goal was to develop an HNF forming material that absorbed visible light that could be incorporated into the active layer of an OBHJ solar cell.

1.5 Approach

The crystalline nature of the HNF phase makes the rational design of new HNF forming materials tricky at best since even slight modifications to known HNF forming materials often result in the destruction of the phase. In this thesis, I report on three complementary approaches to address this problem. The first is a *brute force* method to extend the structure space of the HNF molecules through chemical modification. The second by-passed the delicacy of the HNF phase structure space by studying ways of using the HNF as a scaffold with which to attach functional (including light-absorbing) molecules to the filament surface. The third was a direct study of the effect of nanoconfinement on a closely related phase, the low temperature dark conglomerate (DC), to effectively expand the HNF structure space by including DC forming molecules. Extension of the structure space was deemed to be the requisite first step in the search for HNF dyes because the relatively few molecular structures of the HNF structure space severely limit the options available to a synthetic chemist for the design of new materials. If the structure space could be expanded or a system developed that effectively removes this

issue all together, this would multiply the options available to the researcher to engineer visible-light absorbance in the HNF phase.

To this end, we incorporated the visible-light absorbing chromophore, azulene, into known HNF forming structures as a direct attempt to probe the structure space through chemical synthesis while obtaining the desired absorbances for solar cell devices. A complimentary approach to this direct method was functionalization of the HNF surface through modification by the Huisgen 1,3-dipolar cycloaddition reaction and was designed to bypass the need for major HNF chemical structure modification by employing the HNF as a physical scaffold on which functional molecules could be attached. This removes the burden of directly using the filaments as the active layer in a device and allows for them to be employed in a secondary role, providing physical support and alignment to template other functional molecules. Finally, the third approach was designed to investigate the underlying mechanism that differentiate the HNF and the DC phase, with the idea that a better understanding of the formation of the two phases would allow us to better design functional HNF forming materials. By using an external stimulus (nanoconfinement) to induce a change in morphology of the DC phase, we would be able to incorporate the molecular structures of the DC phase to the HNF structure space, providing new molecular structures with which to use in material design.

2 Azulene Based Bent-Core Liquid Crystals

2.1 Introduction

This project began as an investigation into whether or not visible-light absorbing helical nanofilaments could be realized for application in ordered bulk heterojunction (OBHJ) organic photovoltaics (OPVs). Previous research look into the utilization and synthesis of bent-core liquid crystals (LCs) that were based on monomers of known conducting polymers such as 2,5-bis(3-alkylthiophen-2-yl)thieno[3,2-b]thiophene (BTTT). Attempts to synthesize the bent-core LCs were unsuccessful, and efforts were turned to analyzing the electronic properties of a homologous series of calamitic compounds that were successfully synthesized. However, aside from the fact that the bent-core LCs were difficult targets to synthesize, the materials studied also did not significantly absorb visible light - a characteristic that is essential for the active layer of an OPV device. It was determined that the design of new bent-core LCs for usage in OPV applications should focus on creating materials that possess the absorbances needed and attempts at synthesis were abandoned for the monomer-based materials. New materials were designed utilizing azulene as the chromophore while many structural motifs of previously reported HNF forming materials were maintained.

2.1.1 Photovoltaic Cells

Photovoltaic cells are devices that convert light into electricity. Operating in the visible range of the solar spectrum, these devices utilize active layers of semiconductors (made up of either inorganic or organic materials) to absorb incident photons to generate free electric charges that can be collected at their respective electrodes and passed through the circuit to generate work.[12] This charge separation occurs at the interface (the junction) between the two semiconducting materials which are chosen to have different Fermi levels providing the driving force needed to allow the charges to travel to their correct electrode. On one hand, inorganic materials have the benefit of possessing high dielectric

constants which results in higher overall efficiencies. Free charge carriers can be directly generated, and the probability that two oppositely charged carriers will meet and recombine is lowered. Organic materials, on the other hand, have low dielectric constants and do not shield free charges from one another as efficiently as their inorganic counterparts.[12] This results in the formation of excitons which are coulombically bound electron/hole pairs that must be separated into free charge carriers.

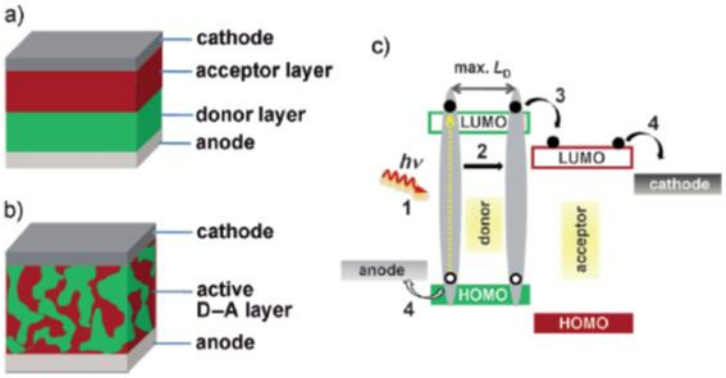

Figure 2.1 - An illustration representing (a) a planar and (b) a blended bulk heterojunction device construction. (c) schematic representation of charge generation in a BHJ device. 1) an exciton is generated by absorption of light 2) the exciton migrates to the interface 3) the exciton is split and 4) the free charges migrate to their respective electrodes.[15]

Initial work with heterojunction solar cells used a planar interface between the two components of the active layer.[13–15] Since charge separation occurs at the interface of these devices, excitons generated far from the interface would not be separated into free carriers resulting in an unproductive light absorption event.[14] Later work investigated blending the two components together, producing the BHJ scaffold.[16] This blending greatly increases the interface surface area, as well as decreases the width of the component domains both of which work in tandem to increase the efficiency of the device. However, random blending of the two materials results in the formation of completely isolated areas of one component (islands) or areas that are not directly connected to the respective electrode (cul-de-sacs).[14] Excitons generated in these areas may still be separated into free charge carriers but leave behind one carrier (either an electron or hole) that is trapped and unable to diffuse to the electrode.

These trapped charges lead to recombination sites and decrease the efficiency of the device. To circumvent this problem, ordered bulk heterojunctions (OBHJs) were developed (**Figure 2.2**).[17]

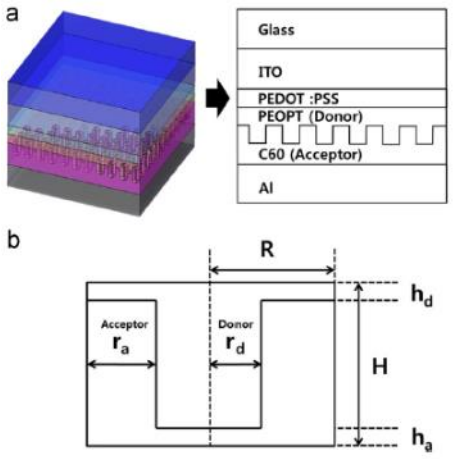

Figure 2.2 - A schematic of an ordered bulk heterojunction solar cell (a). The ideal aspect ratios of the donor and acceptor layers for an optimized OBHJ cell (b).[16] For the features of the OBHJ to be effective, the width of the features should be less twice that of the exciton diffusion length to allow for efficient charge separation.

OBHJ devices align the active layer components to provide directs paths for the separated charge carriers to their respective electrodes. Methods to synthesize these kinds of arrangements involve nanoscale printing, growth in porous media, and self-assembly.[18,19] To maximize the efficiency of the device, the length scales for the active layer features should be less than that of the exciton diffusion length. The HNF phase of bent-core LCs has the required length scales and other physical characteristics that makes it attractive for application in an OBHJ device.

2.1.2 Helical Nanofilaments

Inherent in their nature, HNFs are long, one dimensional nanoscale crystals that can extend for microns in length.[7] Studies have utilized x-ray diffraction experiments (XRD) coupled with freeze fracture transmission electron microscopy (FF-TEM) to reveal the phase characteristics and the structure of prototypical HNF forming compound P-9-OPIMB (NOBOW).[7] Cooling NOBOW from the higher temperature B2 phase, XRD experiments showed a broadened layer reflection in the small angle region

suggesting the loss of coherence over large length scales and the growth of peaks in the wide-angle region indicating the formation of intra-layer ordering (**Figure 2.3**).

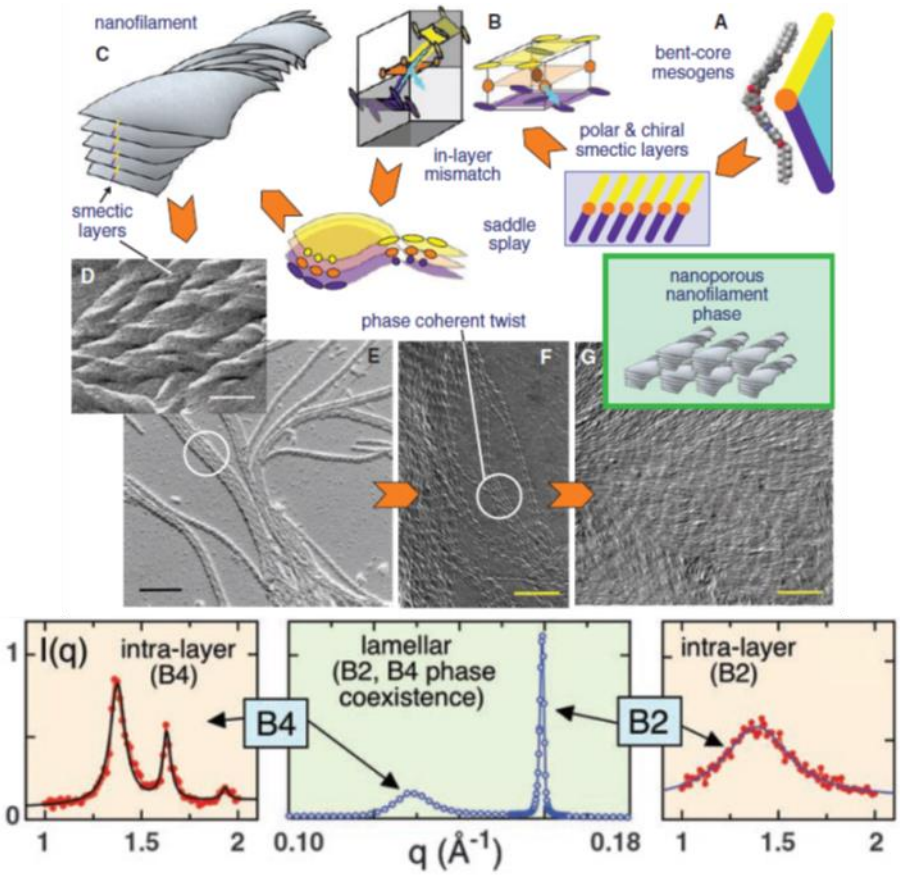

Figure 2.3 - The HNF phase is formed by BLC molecules (a) that tend to form layers (b) when these layers deform into saddles, helical filaments (c) can be formed. FFTEM images of the HNF phase (d-g). A typical XRD plot is given in the bottom image.[9] The sharp diffraction peak of the B2 layers gives way to a broad peak at lower q, indicating loss of long range correlation of the layers. The presence of three peaks at wide-angle indicate the formation of in-plane ordering.

These observations support the formation of nanoscale filaments constructed of a few smectic layers that have crystalline order. FF-TEM images confirmed bundles of twisted filaments measured to be 25-30 nm in width which corresponds to approximately 5-6 layers, and also extend for several microns in length (**Figure 2.3**). Additionally, it was reported that the filaments form large conglomerate domains with coherent twist dependent on the handedness of the parent filament from which all others stemmed.[9] Since these filaments are approximated by a cylinder, the conglomerate must be porous

since closely packed cylinders cannot completely fill space. This led to creating blends of HNFs with various types of materials including small molecules and polymers.[10] One material that is of interest is the common small molecule electron acceptor C60 and is closely related counterpart PCBM. These two materials are commonly used as the electron accepting portion of an active layer in organic solar cells. The composites showed complete confinement of the C60s in between the filaments with no incorporation of the fullerenes in filament structure. The composites were then studied using time-resolved microwave conductivity (TMRC) experiments to understand the electronic behavior of the filament fullerene interface.[11] A long-lived microwave decay signal was observed indicating the presence of long-lived free charge carries within the sample showing that the interface was efficient at separating the bound charge carriers (excitons) and preventing the charges from recombining (**Figure 2.4**).

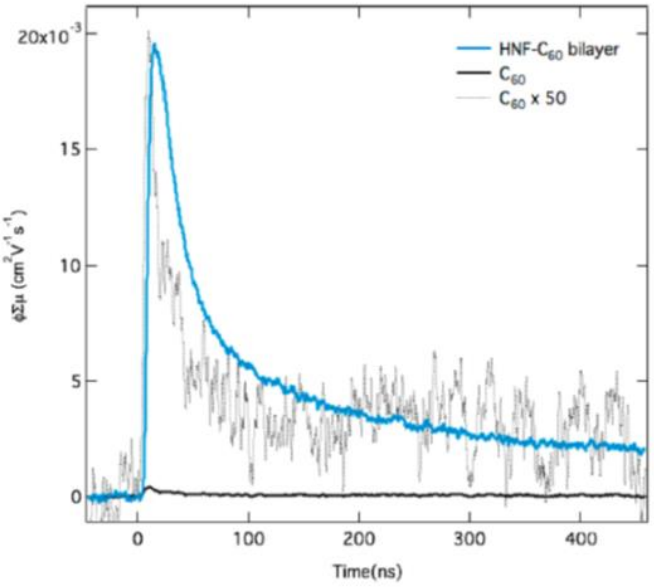

Figure 2.4 - The TRMC signal given by an HNF/C60 composite (blue line) versus C60 alone (black line).[13] The large signal due to the HNF/C60 composite indicates long-lived charge carriers, indicating the interface is highly efficient at separating charges.

Additionally, experiments to align the HNFs over large length scales showed that alignment could be achieved through using the shear forces and anisotropic thermal gradients of directional

airflow, growth in the microchannels of PDMS molds, and in the nanoscale pores of anodized aluminum oxide membranes.[20–22] These results led to the hypothesis that the HNF phase may be an ideal candidate for application in the active layer of an organic solar cell. Its crystalline nature, efficiency of charge separation, and ability to align the filaments, allows for the filaments to be used as nanoscale wires, theoretically increasing the efficiency of the device by lowering charge trap sites of "islands" and "cul-de-sacs" commonly encountered in blended bulk heterojunctions. However, the main issue yet to be addressed is the issue of absorbance. To date, all HNF forming materials have absorbances in the near UV portion of the solar spectrum. Incorporation into an active device requires that the visible portion of the solar spectrum be completely (or nearly completely) absorbed to maximize device efficiency.

2.2 Hypothesis

The crystalline nature, efficiency of charge separation, and ability to align the filaments effectively allow for the filaments to be used as nanoscale wires, increasing the efficiency of a BHJ by lowering charge trap sites of "islands" and "cul-de-sacs" commonly encountered. However, the main hurdle yet to be addressed is the issue of absorbance. To date, all HNF forming materials have absorbances in the near-UV portion of the solar spectrum. Incorporation into an active device requires that the visible portion of the solar spectrum be completely (or nearly completely) absorbed to maximize device efficiency. To do this we reasoned that through molecular design we could develop a new material that retained the HNF phase while also having an absorbance encompassing most of the visible spectrum.

2.3 Molecular Design

The design of new LC materials is largely empirical and based upon identifying certain characteristic features of known materials that give the desired phase. These characteristics are then

incorporated into the new molecular structure and synthesized. Certain phases lend themselves to molecular modification and are said to have a large or broad “structure space”. The structure space of a phase simply refers to the number of different types of molecular structures that make up that phase. For example, the SmA phase is comprised of countless different structures and types of structures, is one of the most common LC phases, and is said to have a very large structure space. The HNF phase of bent-core LCs, however, has a very narrow structure space and this issue must be addressed when designing new molecules. With this in mind, new modifications can achieve two goals if done properly. They can probe the boundaries of the structure space if they are done in small increments, and they can impart new functionality to the material.

2.3.1 Tuning absorption

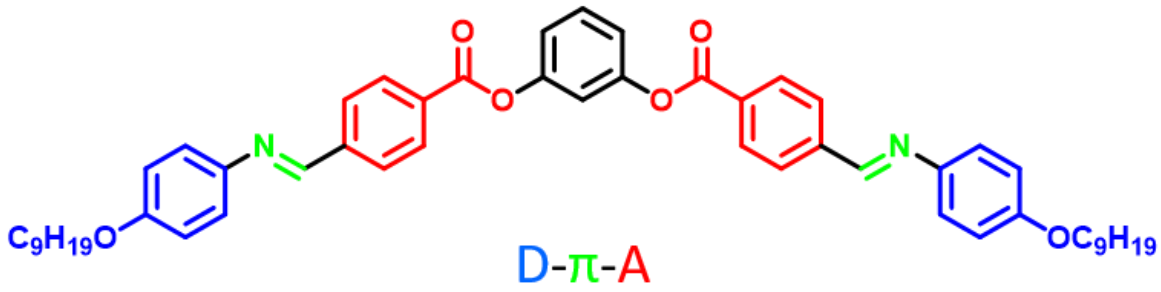

Figure 2.5 - The molecular structure of prototypical HNF forming compound NOBOW highlighted to emphasize the donor-pi-acceptor (D-π-A)system. Initial work focused on exploiting the built-in D-π-A nature of the NOBOW core to design new BLCs with red-shifted absorbances. Unfortunately, the absorbances were only slight, and the HNF phase was not maintained.

The absorption of a material can be modified in different ways. In the synthesis of dyes, it is common practice to utilize what is known as a Donor-Pi-Acceptor system (D-π-A) in which a strong electron donating group is attached to a strong electron accepting group by a conjugated pi spacer. The optical band gap of a material can be approximated by the energy difference between the highest occupied molecular orbital (HOMO) and lowest unoccupied molecular orbital (LUMO) of the compound. This energy difference corresponds to the lowest possible electronic transition a molecule can undergo.

Since the energy of a photon is inversely related to its wavelength, a smaller HOMO/LUMO gap results in the ability to absorb photons of longer wavelength. Modification of the strength of the electron donor/acceptor effectively destabilize/stabilize these orbitals brining their energies closer together. Increasing the length of the conjugated pi spacer increases the "box" length available to the electron, increasing its wavelength and lowering its energy. It was observed that the prototypical HNF forming materials have this D-π-A scaffold already in place and is highlighted in NOBOW (**Figure 2.5**). Initial work designed molecules with different donors and acceptors incorporated into the backbone of NOBOW but resulted in insufficient red-shifting of the absorbance, and destruction of the HNF phase. This route was subsequently abandoned.

Another way to tune the absorbance of a molecule is to incorporate a chromophore, that already has the absorbance needed, into the molecular structure. Instead of incrementally red-shifting the absorbance through modification, the chromophore effectively does all the work. This approach resolves the issue of the insufficient absorption experienced earlier by implementing the D-π-A method and allows for focus to be put on design of the molecular structure. Design of the new class of materials then focused on incorporation of azulene as the chromophore in the bent-core liquid crystals.

2.3.2 Azulene

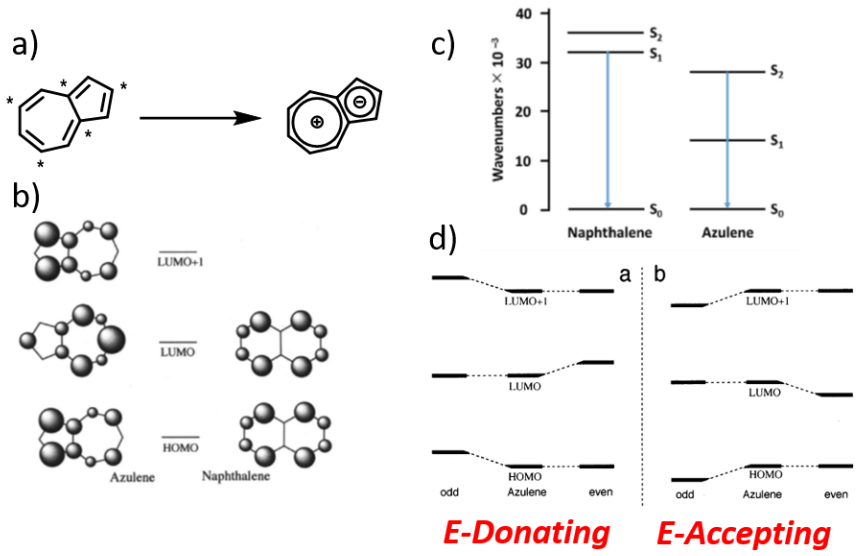

Figure 2.6 (a) The non-alternant and dipolar nature of azulene. (b) Charge distribution of azulene versus naphthalene.[26] (c) Energy level differences of the first and second singlet excited states for naphthalene and azulene.[26] (d) Shifting of the frontier molecular orbital energies of azulene as a function of functional group character and position on the ring.

Azulene is a non-alternant aromatic compound that displays a deep blue color and significant dipole; characteristics that are unusual as it is an isomer of naphthalene, a nonpolar colorless hydrocarbon (**Figure 2.6**). Its anomalous absorbance can be attributed to its non-alternant nature, and the effect that has on the distribution of the molecular orbitals.[23] Alternant molecular systems have orbitals that are paired through symmetry, and as such, have their HOMO and LUMO occupying the same areas (atoms) in space.[24] Since both orbitals share the same space, an electron excited from the HOMO to the LUMO experiences a strong repulsive force from the electron left behind and the energy difference between the two orbitals is large.[23] However, for non-alternant systems, the orbitals are often not paired though symmetry and has a result can occupy different atoms on the molecule. This separation of charge minimizes the repulsion felt by the two electrons, allowing for the difference in orbital energy to be smaller yielding absorbances that are red shifted from what may have been expected. Chemically, the energetics of the orbitals in azulene can also be manipulated by attaching

electron donating/accepting functional groups to the odd/even carbons.[25] In the case where electron donating groups are attached to the odd number carbons, the HOMO and LUMO+1 orbitals are destabilized as the highest degree of electron density resides on these atoms. Conversely, the opposite effect is observed when an electron accepting group is positioned there and the opposite trend is seen for the even numbered carbons (**Figure 2.6**).

Electronics

Traditional organic electronics have been based on various aromatic and conjugated systems with moieties generally focused around phenyl, naphthyl, thiophenyl, and other such ring systems. It has only been recently that azulene has gained attention for applications in organic optoelectronics and this may be attributed to the fact that only recently have new strategies for functionalizing the azulene unit been developed.[24] Within the past decade work has been done to incorporate azulene into organic field effect transistors (OFETs) and organic photovoltaic (OPV) devices. Interestingly, a number of n-type organic semiconducting materials have been synthesized, though organic compounds are generally p-type hole transporting materials. The unusual n-type characteristics of the azulene base materials is a result of the tuneability of the frontier molecular orbitals of the azulene unit which are dependent on the positioning and nature of the attached functional group.[26] Materials in which the HOMO is largely localized only on one portion of the molecule tend to have a LUMO that is spread across the entire backbone of the molecule allowing for more efficient electron transport for electrons, rather than holes. Additionally, other materials have shown to be ambipolar in nature, allowing for balanced transport of holes and electrons throughout the entire material.[27] Mobilities within these materials range from moderate ($1x10^{-4}$ cm^2/Vs) to good (1 cm^2/Vs) depending on the nature of the conjugation within the system, and the molecule's ability to pack.[24] Decent power conversion efficiencies have also been reported in OPV devices constructed with both small molecule and polymer materials containing azulene.[24]

Synthesis

The asymmetric distribution of orbitals azulene also results in interesting behavior chemically for azulene and must be considered when designing functionalized versions. Two approaches exist to synthesize substituted azulenes; direct functionalization of azulene itself, or construction of the structure with the substituents already in place.[24]

Direct Functionalization

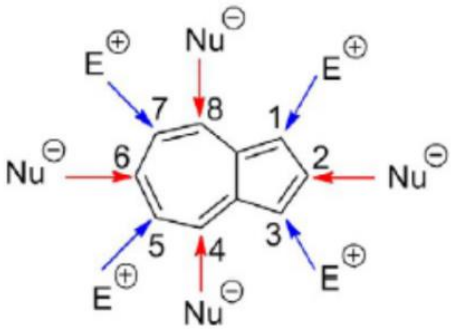

Figure 2.7 - The reactivity of azulene towards electrophiles and nucleophiles. Do to the non-alternant nature of azulene, the distribution of the molecular orbitals is no longer related by symmetry. This leads to the majority of the electron density in the HOMO being localized on the odd numbered carbons. As a result, the reactivity towards electrophiles/nucleophiles alternates on the azulene skeleton.[26]

Direct functionalization of azulene lends itself to substitution on the five membered ring. The one and three positions have the greatest amount of electron density and are there for the most nucleophilic positions on the molecule. Electrophilic aromatic substitution (EAS) reactions easily react at these positions and a variety of functional groups can be placed here selectively.[28] If both positions are blocked, access to the seven membered ring is achieved mainly through the five and seven numbered positions. Nucleophilic addition occurs exclusively at the seven membered ring usually giving a mixture of isomers at the four six and eight positions. Discrimination between the either the four/eight position and the six position can be obtained by using hard or soft nucleophiles. Hard nucleophiles preferentially add to the four and eight positions where soft nucleophiles add to the six position.[29,30] Though the two position on the five membered ring lacks the electron density completely, the negative characteristic of

the five membered ring, as a result of the charge separation, prevents traditional reactions from functionalizing this position. Recently, however, C-H activation reactions have been developed to selectively react at this site.[31] Due to the rarity of azulene itself (commercially and in nature), it can be more practical to synthesize the carbon skeleton with the desired functionality already in place, rather than through direct functionalization.

Construction of the Azulene Skeleton

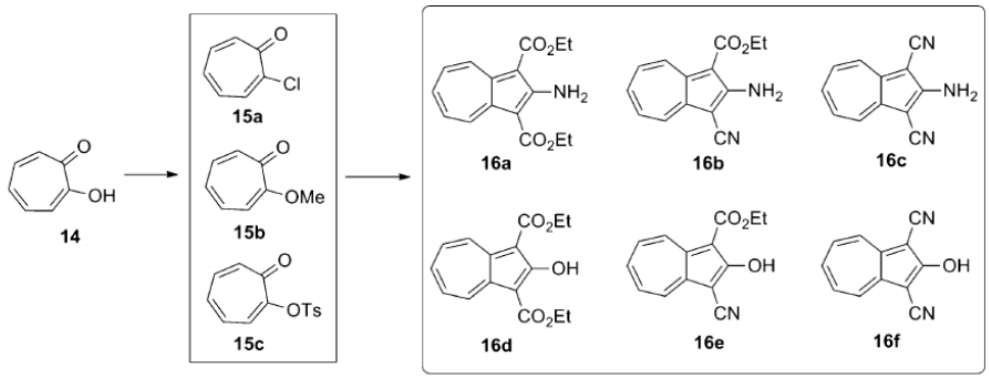

Figure 2.8 - Tropolone as a route to various functionalized azulenes. Activation of the tropolone hydroxyl group followed by the condensation with a variety of malonic derivatives and 1,3-disubstitued acetones results in substitution of the five membered ring with a variety of functional groups that can then be manipulated later.[26]

Construction of the azulene skeleton can be executed in a variety of ways. Work by Nozoe laid the foundation for constructing the azulene ring starting from tropolone (**Figure 2.8**).[32] The tropolone hydroxyl group can be activated towards nucleophillic attack from malonic type systems or 1,3-disubstituted acetones. After the condensation is complete, the seven membered ring is available for substitution as all positions on the five membered ring are blocked. Removal of the ester groups can be achieved through sequential decarboxylation reactions giving a straight forward route to synthesizing 2,6-disubstituted azulenes which are desired for organic optoelectronic applications, albeit often over the course of four or more steps. The Ziegler-Hafner method uses activated pyridines and the cyclopentadienylide (Cp) anion to provide access to selective substitution on the seven membered ring

as the substituents come are maintained in the same positions as they were on the pyridine.[33] Additionally, the Cp anion can be functionalized as well leading to another route to 2,6-disubstituted azulenes though the 1,6-disubstituted isomer is also formed (**Figure 2.9**). Takase developed a method to construct functionalized and fused ring systems of azulene by reacting 2-oxazulanone with various enamines to functionalize the five membered ring.[34] The 2-oxazulanone intermediate was synthesized from an active tropolone in a manner similar to the chemistry developed by Nozoe. Di-oxides of substituted thiophenes can also produce azulenes with substitution on the seven membered ring through reactions with fulvalenes.[35] Due to its straight forward nature, one-pot synthetic nature, and facile formation of the 2,6-disubstituted isomer, the Ziegler-Hafner method was chosen as the desired reaction our purposes.

The Ziegler-Hafner Method

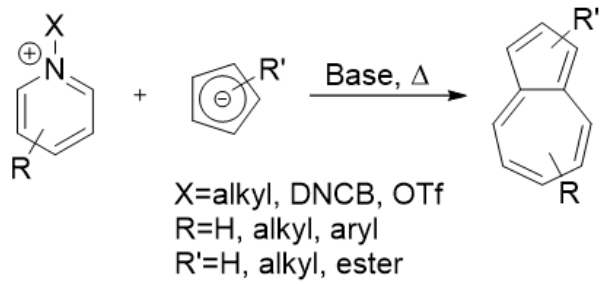

Figure 2.9 - General scheme for the Ziegler-Hafner method for azulene synthesis. Activated pyridines are the key to construction of the azulene skeleton. Functionality on the pyridine ring is maintained throughout the synthesis on the seven membered ring. Substitution of the Cp anion provides functionality on the five membered ring.

Of the various synthetic routes to functionalized azulenes, the Ziegler-Hafner method is especially useful for selective functionalization at the seven membered ring and provides a route to di-substitution if both the prerequisite pyridine and Cp anion are functionalized. This method utilizes the reactivity of activated pyridines with nucleophiles to construct the azulene carbon back bone. Initial work exploited “Zincke” chemistry where the pyridine was activated with 2,4-dinitrochlorobenzene (DNCB) through a nucleophillic aromatic substitution to give the Zincke salt.[33] Later it was shown that

activation could be achieved via several activating agents including alkyl halides and triflic anhydride depending on the nucleophilicity of the pyridine nitrogen.[36] For more nucleophilic pyridines, the alkyl halide is strong enough of an electrophile to alkylate the nitrogen forming the pyridinium salt.[37] However, for deactivated pyridine rings (with attached electron accepting functional groups), stronger electrophiles (e.g. triflic anhydride) are needed to form the desired pyridinium salt. Once formed, the ring is opened by a nucleophilic attack of a small secondary amine such as dimethyl or diethyl amine. The resulting intermediate is a brightly colored cyanine type dye that is now receptive to condensation with the Cp anion to establish the initial carbon skeleton. Finally, a thermally allowed 10-π electrocyclization followed by re-aromatization results in the completed azulene ring. Depending on the orientation of the five membered ring in the intermediate (given that substitution in this position is present) during the electrocyclization step, the resulting azulene may either have a 1,6 or 2,6 substituted nature, with both isomers forming over the course of the reaction.[33] The ambiguity of regiochemistry may be exploited in the design of new bent-core liquid crystals as the linearity of the 2,6-isomer may be utilized in the arm portion of the molecule, while the 1,6-isomer can be used as a novel bend unit.

2.3.3 Coupling HNF Materials with Azulene

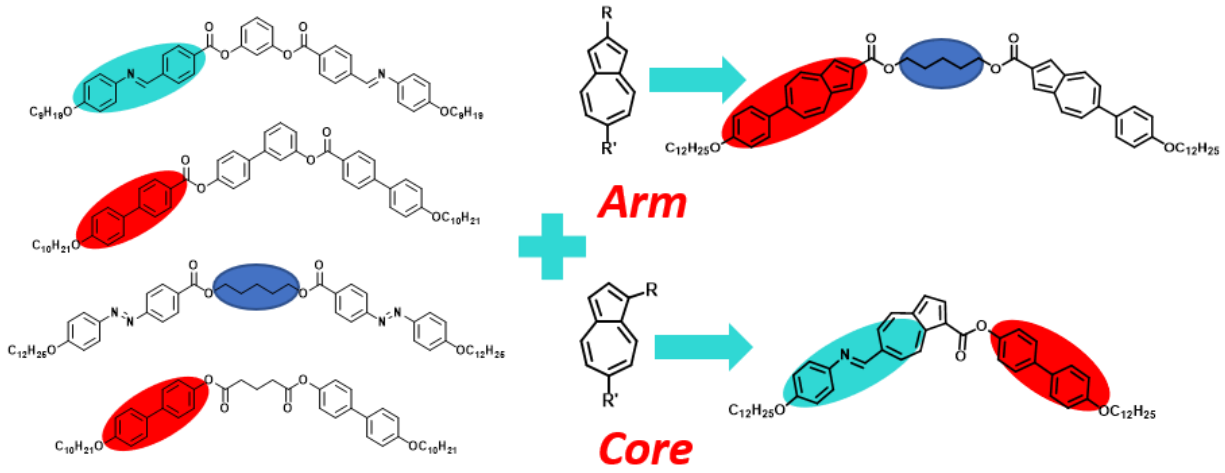

Figure 2.10 - Design principles for azulene based BLCs. The compounds on the left represent the structure space for the HNF phase. Highlighted are the pieces thought to promote the formation of the phase. Since synthesis of the azulene ring involves the formation of two isomers, each isomer may be utilized as either part of the arm or core for the new compounds. Retention of the defining functional groups generates new bent-core compounds with azulene incorporated in hopes to maintain the HNF phase while imparting the absorbance properties on the material.

In order to give the designed materials the "best chances" of forming the HNF phase, efforts were made to incorporate the Schiff base, biphenyl, alkoxy tails, and overall bent structure into the final targets. Placement of the azulene was then attempted in such a way as to not disrupt the essence of the known HNF forming materials and great care was taken to make the modifications as slight as possible.

Arm

Exploitation of the fact that the Ziegler-Hafner method gives two regioisomers of di-substituted azulenes led to the design of new bent-core LCs with the linear 2,6-disubstituted azulene incorporated into the rigid arms of the molecules. Parent structures for this type of molecular design were based off the 12OAM5AMO12 dimer structure reported by Khoa, biphenyl twins reported by Gorecka and Tsai, as well as NOBOW.[7,8,38,39] In all cases, a phenyl ring was replaced with the 2,6-disubstituted azulene, giving the phenyl azulene compound W1006 and phenyl azomethine azulene compounds W1009 and W1014.

The 1,6-disubstituted isomer was also incorporated into the arm of molecules W1013 and W1015 to investigate the effect the angle of the central bend unit has on the behavior of the molecule.

Core

The 1,6-disubstituted isomer has a bend angle of 125° which is right in the ideal range (~120°) of angles for bent-core compounds. This isomer was used to replace the traditional cores of BLC materials such as resorcinol and Tsai's bisphenol core.[39] By introducing the formyl and ester groups at the 6 and 1 positions respectively, the ability to maintain the HNF promoting Schiff base and biphenyl ester was apparent. Its utilization in the core gave materials W1007 and W1008.

2.3.4 Synthesis

Phenyl Azulene

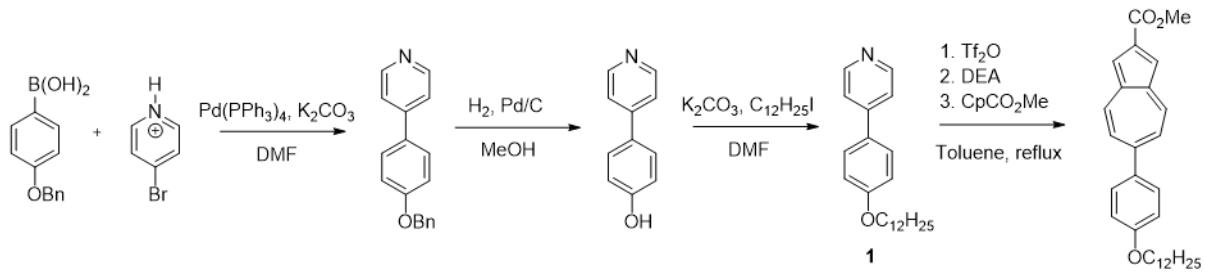

Figure 2.11 – General reaction scheme to synthesize the phenyl azulene intermediate needed to synthesize the bent-core compounds.

The synthesis of the phenyl azulene derivative (meant to mimic the biphenyl system of Gorecka's dimers and Tsai's asymmetric molecules) required the synthesis of 4-[4-(dodecyloxy)phenyl]pyridine (**1**) as the desired pyridine precursor. This was achieved by coupling [4-(benzyloxy)phenyl]boronic acid with 4-bromopyridinium bromide under Suzuki conditions to yield 4-[4-(benzyloxy)phenyl]pyridine. The deprotection of the benzyl ether was achieved by submitting the compound to reducing conditions with H_2 and palladium on carbon to give 4-(pyridin-4-yl)phenol which was then reacted with 1-bromododecane under Williamson conditions to afford the desired 4-[4-

(dodecyloxy)phenyl]pyridine intermediate. The azulene skeleton could now be established by reaction with sodium 1-methyl-cyclopentadienylidecarboxylate by the Ziegler-Hafner method giving methyl 6-[4-(dodecyloxy)phenyl]azulene-2-carboxylate, which was subsequently hydrolyzed and reacted with 1,7-dibromoheptane in an S_N2 fashion to give the desired bent-core compound.

2.3.4.1 Phenyl Azomethine Azulene

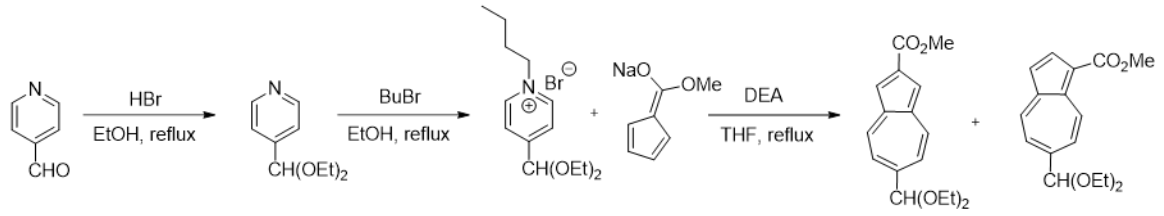

Figure 2.12 - General scheme to synthesize the acetal protected azulene isomers needed to synthesis the phenyl azomethine azulene BLCs.

Synthesis of the phenyl azomethine azulene derivatives (which retained the Schiff base linker of NOBOW) required synthesis of the acetal protected pyridine as the precursor needed to establish the appropriately substituted azulene rings. This was readily accomplished by submitting 4-formylpyridine to a solution of HBr in ethanol, followed by removal of water and ethanol through azeotropic distillation with toluene. The crude material was then treated with butyl bromide in ethanol at reflux to activate the pyridine for the next step. Finally, establishment of the azulene ring was achieved under Ziegler-Hafner conditions to give the desired disubstituted azulenes, available for the final reaction steps required to establish the bent-core molecules.

2.4 Materials

STRUCTURE	W Number	λ_{max}	Phase Sequence
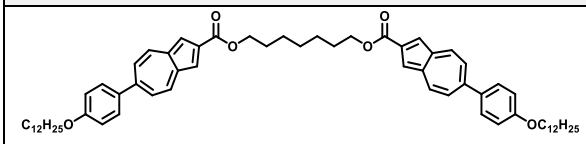	W1006	600 nm	Iso(202 °C)Sm$\tilde{A}$(125 °C)Sm$\tilde{E}$
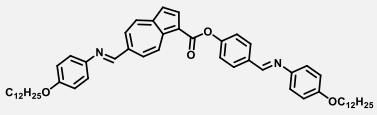	W1007	576 nm	Iso(186 °C)Col?(138 °C)Sm?/X (110 °C)Glass
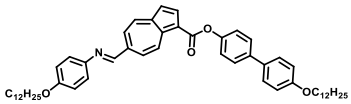	W1008	580 nm	Iso(176 °C)Col?(149 °C)Sm?/X (120 °C)Glass
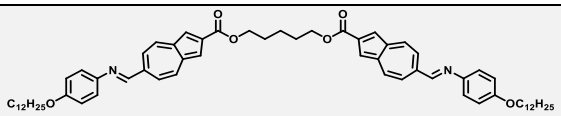	W1009	656 nm	Decomposed on heating
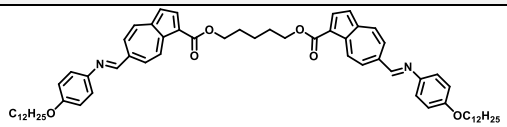	W1013	592 nm	Iso(115 °C)(N)(110 °C)X
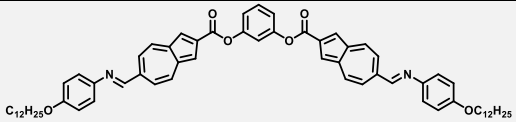	W1014	656 nm	Decomposed on heating
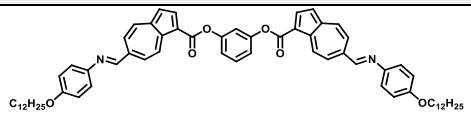	W1015	582 nm	Decomposed on heating

2.4.1 W1006

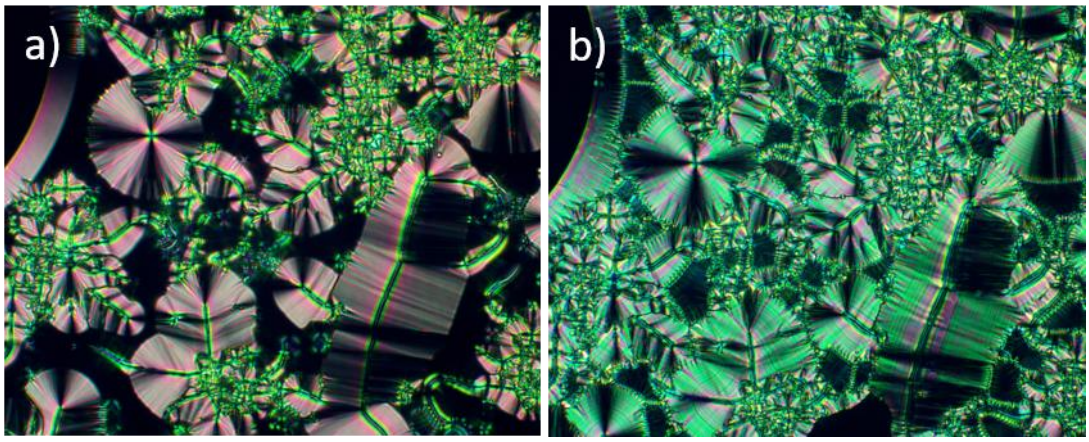

Figure 2.13 - POM images of W1006 at 20x magnification in a 4 µm planar aligned cell at 203 °C (a) and 99 °C (b). Large ribbon-like domains with smaller disordered rope-like domains are apparent in both images. The extinction brushes are aligned with the polarizer and analyzer in both cases indicating the optic axis is parallel to the layer normal. The formation of concentric rings in (b) indicate the formation of in-plane ordering.

Under the POM, W1006 grew in with large ribbon-like domains along with focal conics and disordered twisted rope areas. As the material cooled, flower petal features became more pronounced around the focal conics and along the edges of the ribbons. The material also changed birefringence from red to green. Further cooling showed the formation of concentric rings that were distributed radially from the center of the focal conics and were maintained all the way down to room temperature. In both phases, the extinction brushes are aligned along the polarizer and the analyzer indicating that the optic axis is aligned parallel to the layer normal.

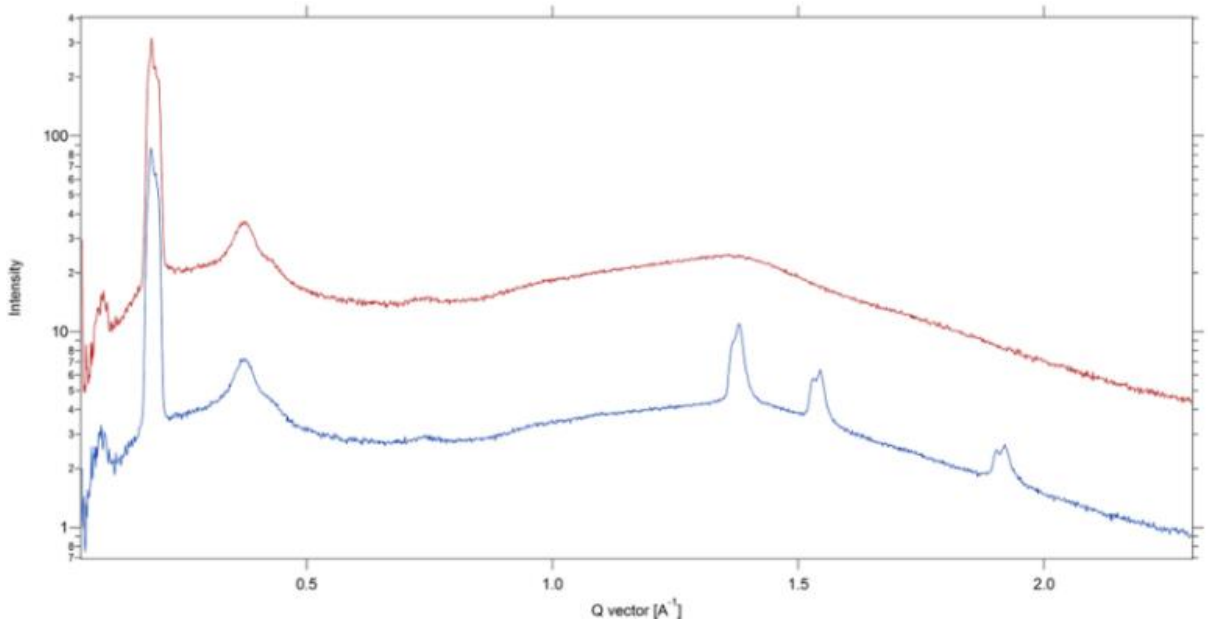

Figure 2.14 - XRD plot of W1006 at 170 °C(red) and 80 °C(blue). A strong signal centered at 0.2 $Å^{-1}$ and the broad peak at 0.4 $Å^{-1}$ are observed for both phases. Neither peak change as the material undergoes a phase transition, indicating the layer structure does not change as the material cools. The presence of three peaks in the wide-angle region for the lower temperature phase indicate the formation of in-plane ordering and supports the observations of ordering in the POM.

XRD experiments showed a strong, unchanging peak around 0.2 $Å^{-1}$ which corresponds to an approximate periodicity of 30 Å, or half the molecular length. Additionally, a broad peak centered at 0.4 $Å^{-1}$ corresponding to a periodicity of 16 Å was present for both phases. The presence of these peaks indicates possible intercalation as the reflections are due to the half and quarter layers respectively. The lower temperature phase had three peaks present in the wide-angle region indicating the formation of hexatic in plane ordering. These observations coupled with the POM data suggest the formation of two intercalated phases that may have layer structures similar to that of the SmA and SmE phases respectively. This data mimics the LC behavior of the calamitic arm of W1006 (see Appendix), indicating that the phase morphology is strongly driven by the nature of the azulene core. This material does not form the HNF phase.

2.4.2 W1007

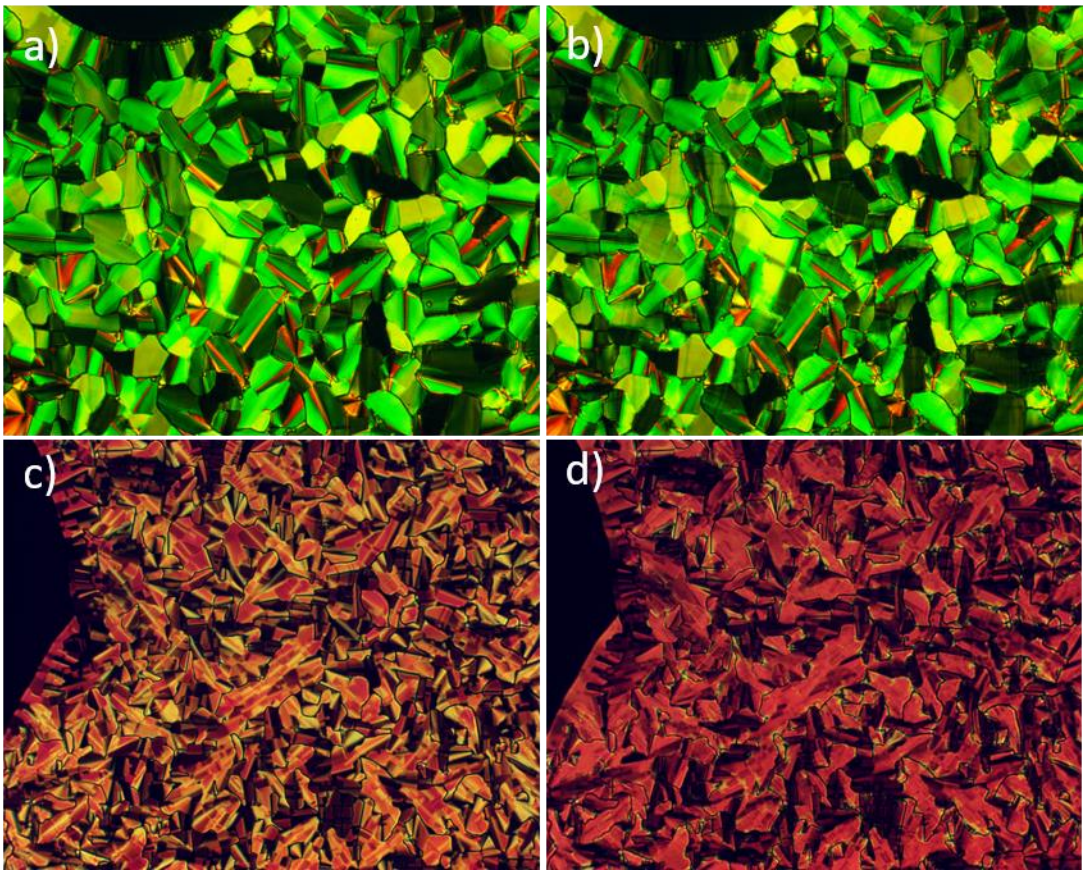

Figure 2.15 - POM images of W1007 at 20x magnification in a 4 µm cell under crossed polarizers at 169 °C (a), 148 °C (b). A mosaic texture is observed for the higher temperature phase indicating potential columnar ordering. This texture is largely maintained with only very subtle evidence of striping seen as the material cools into the lower temperature phase. The texture in a 5 µm cell with no field applied at 170 °C (c) and with a 16V/µm field applied perpendicular to the plane of the page at 170 °C (d). The change in birefringence is maintained even after the removal of the electric field.

Under the POM, W1007 showed a mosaic texture that grew in upon cooling from the isotropic in a 4 µm planar aligned cell (Figure 15a,b). Upon application of an electric field, the domains did not change but the birefringence of the sample increased uniformly (Figure 15c,d). After the electric field was removed, the birefringence stayed the same, indicating that the change was not reversible. This is likely due to a reorientation of the molecules along the field and is not an electrooptic response. Further cooling yielded a highly birefringent and broken texture indicating crystallization had occurred.

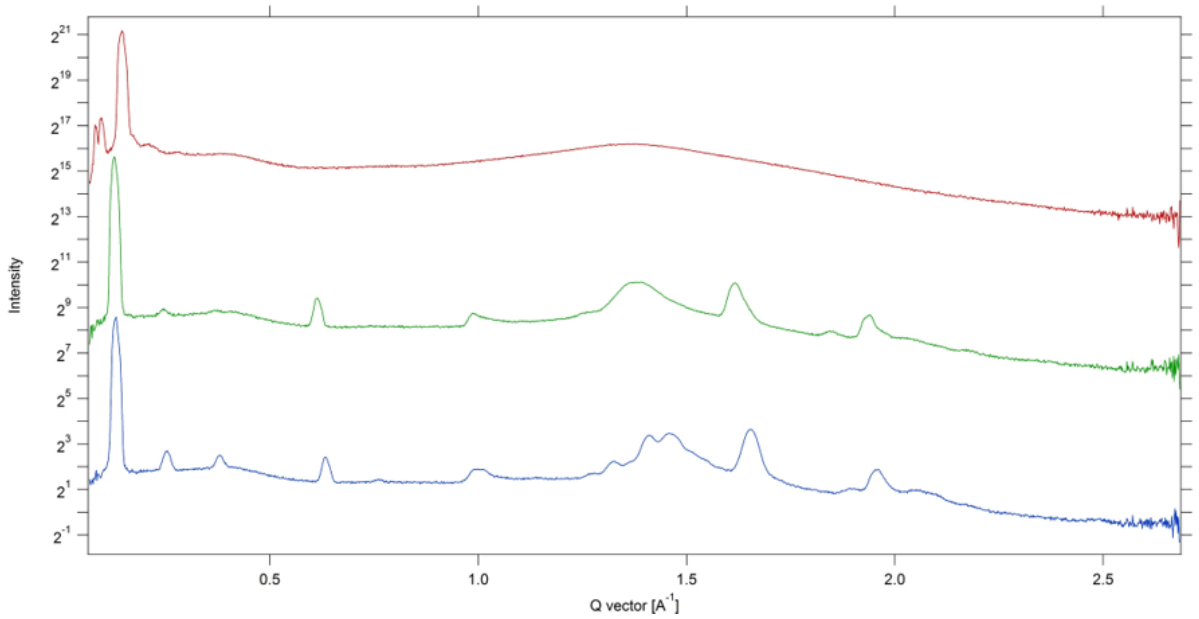

Figure 2.16 - XRD plot of W1007 at 160 °C (red), 130 °C (green), and70°C (blue). The small-angle region shows multiple peaks at q values representing periodicities of 43.9 Å, 72.9 Å, and 89.7 Å for the high temperature phase. These features are lost as the material cools, giving way to a strong reflection centered at 50 Å. Additionally, the lower temperature phases show in plane ordering that becomes more pronounced as the material cools.

In the highest temperature phase, XRD experiments show the presence of multiple features in the small angle region with a broad hump appearing in the wide angle. The small-angle peaks correspond to distances of 89.7 Å, 72.9 Å, and 43.9 Å, respectively, indicating there are multiple features in this phase larger than the molecule itself. Generally, the presence of multiple features in the small angle region indicate columnar ordering. As the temperature is lowered, peaks grow in in the wide-angle region indicating the presence of intralayer ordering, and the small angle peaks are lost, giving one reflection centered at 50 Å, or the molecular length. This could be due to the formation of coherent layers that extend throughout the bulk with the molecules oriented parallel to the layer normal. From this it can be concluded that the highest temperature phase is most likely a columnar phase (possibly B1), followed by a layered, highly-ordered smectic phase and crystalline phase forming underneath. Unfortunately, these results do not support the formation of the HNF phase.

2.4.3 W1008

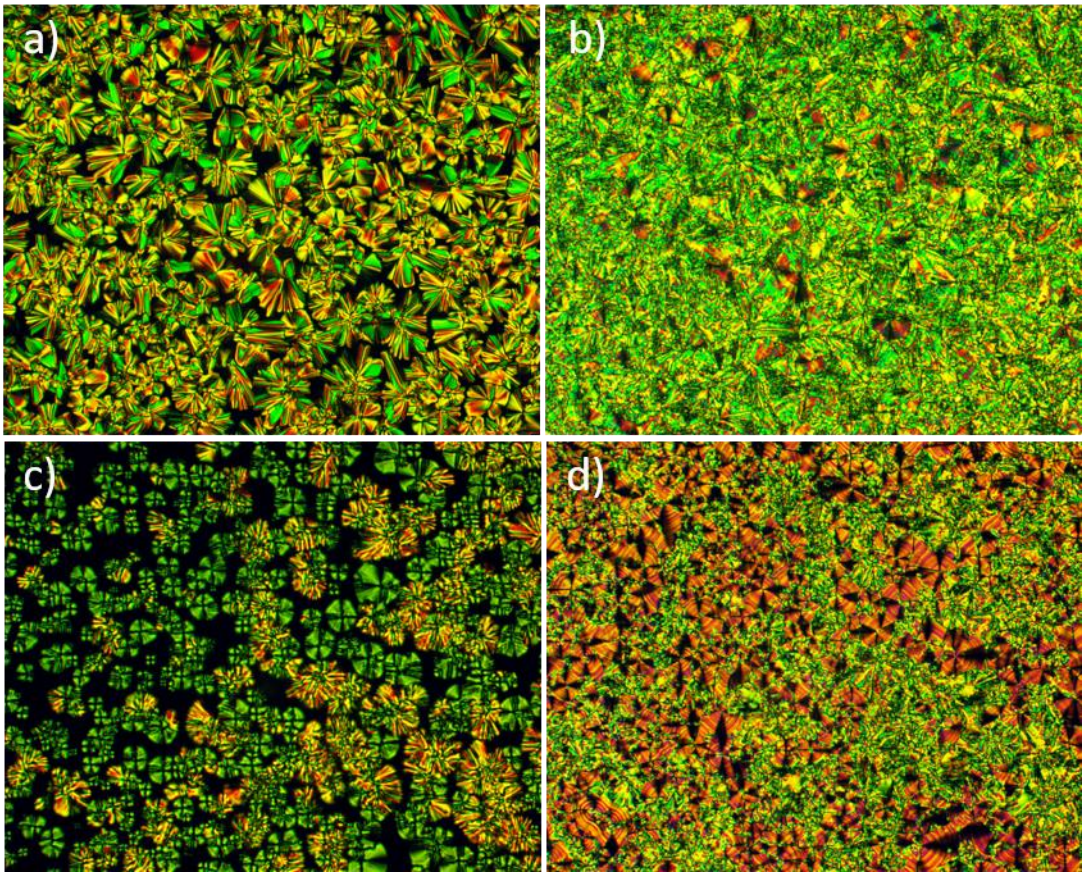

Figure 2.17 - POM images of W1008 in a planar cell at 174 °C (a) and 140 °C (b), and homeotropically aligned cells at 178 °C (c) and 140 °C (d) taken at 20x magnification under crossed polarizers. The planar aligned image in (a) shows and interesting texture composed of highly birefringent, star-like domains, that grow in very quickly from the isotropic. The domains show additional periodicity in the form of lines that outline the shape of the domain. The same phase observed in a homeotropic cell (c) gives domains that suggest columnar ordering. Further cooling shows the formation of a highly ordered Sm phase though the identity is not clear as the texture in (b) is highly disordered and broken which would seem to point to a type of crystal.

Cooling from the isotropic in 4 µm planar aligned cell, W1008 quickly grows in as star-shaped domains with stripes that follow the outline of the shape of the domain. The stripes become more pronounced as the material is cooled further, until a broken grainy texture quickly appears indicating crystallization of the material. When the material is cooled in a glass planchette, a focal conic/mosaic type texture is observed that is different from the planar cell indicating regions of homeotropic anchoring. Further cooling of the cell yields a decrease in the birefringence of the homeotropic regions

indicating the molecules are adopting an orthogonal orientation with respect to layer normal. Finally, a highly birefringent texture, with stripes emanating from the center of the focal conics, forms along with the grainy areas observed form the planar regions, indicating the formation of a highly ordered smectic phase. DSC data show a broad peak forming below the formation of the lower temperature phase, suggesting a glass transition.

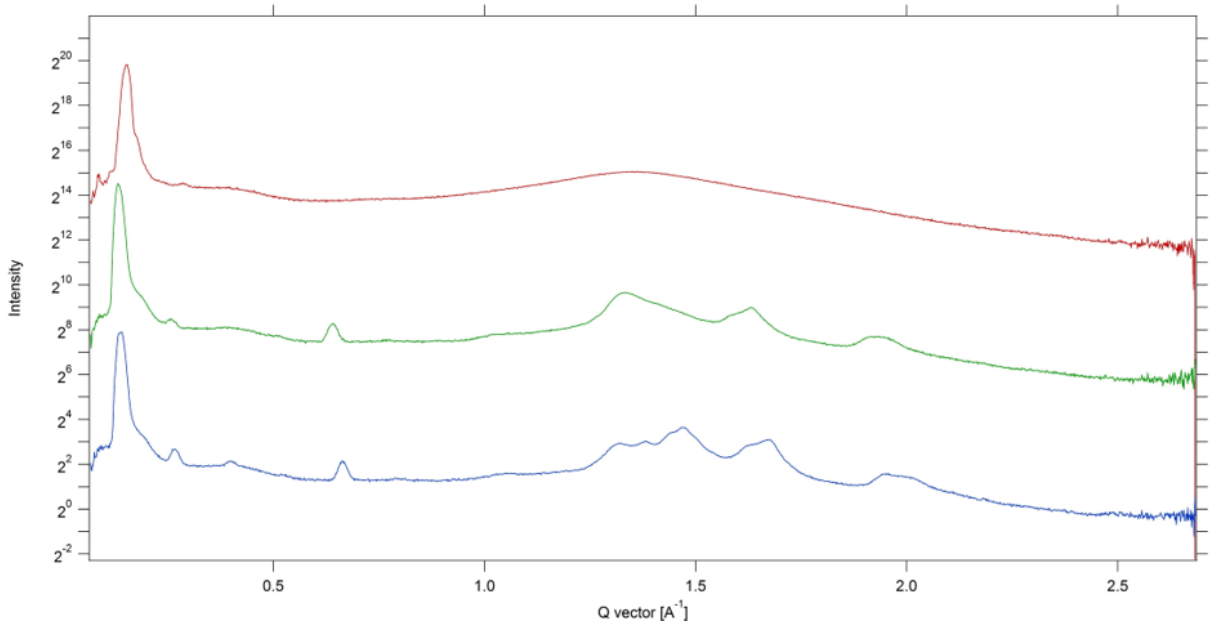

Figure 2.18 - XRD of W1008 at 165 °C (red), 140 °C (green), and 70 °C (blue). The high temperature phase shows multiple features in the small-angle region appearing at 0.13 $Å^{-1}$ and 0.14 $Å^{-1}$ which correspond to distances of 41.3 Å and 43.3 Å , roughly the molecular length. Faint peaks are also observed at 33.8 Å, 36.6 Å, 88.5 Å, and 172.4 Å. These features are lost as the material cools giving way to a broad, shouldered peak centered around 46.8 Å along with the formation of multiple peaks in the wide-angle region indicating the formation of in-plane order.

XRD experiments assessing the high temperature phase, indicate fluid in plane order with a broad featureless wide-angle region. However, the small-angle region shows multiple features with a strong peak at 41 Å which is close to the molecular length. The features very close to the peak centered at 41 Å are close to the molecular length as well, but do not correspond to harmonics or known ratios of the parent peak, indicating that there are domains with slightly different layer spacings. As the material continues cooling, these small-angle features are lost, giving way to a broader peak centered around 47

Å along with the formation of peaks in the wide-angle region. This indicates the slight variation in the layer spacing is blurred, giving a more broadly distributed layer spacing, as well as the formation of crystalline in plane ordering. Again, these results do not suggest the formation of the HNF phase.

2.4.4 W1013

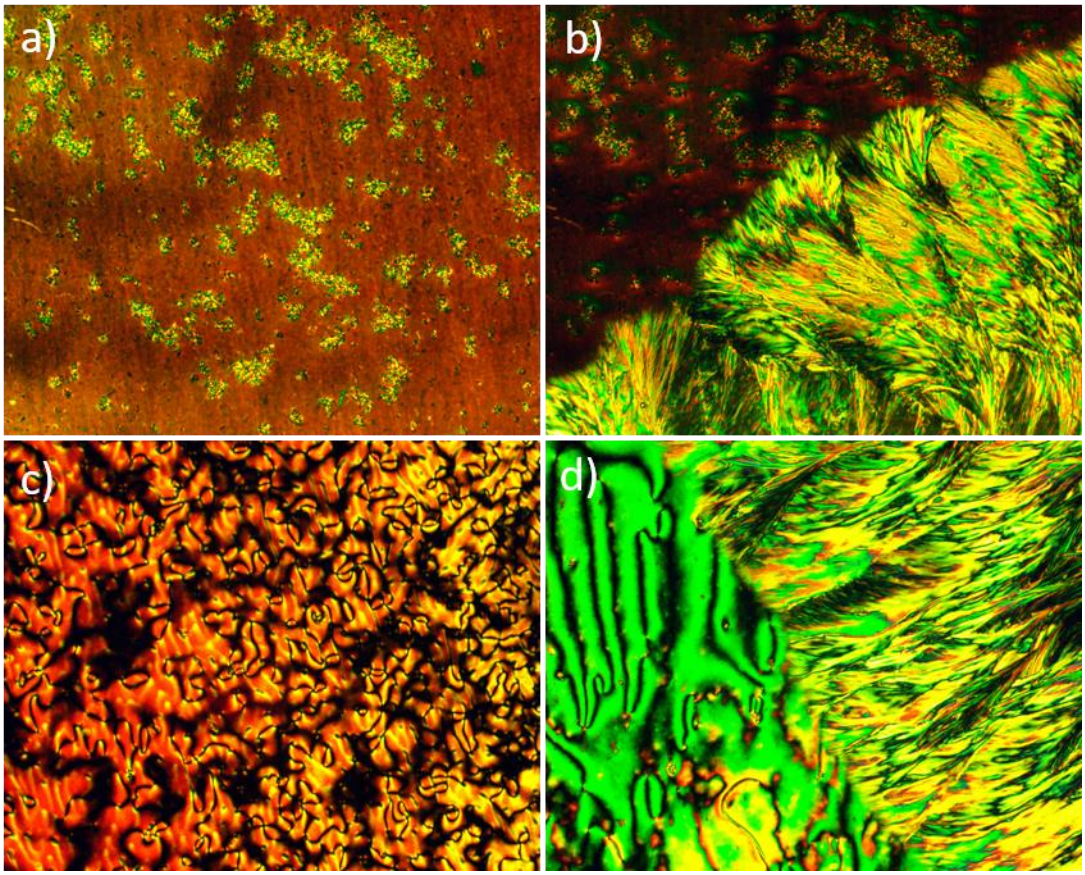

Figure 2.19 – POM images of W1013 in a planar aligned cell at 119 °C (a) and 113 °C (b) and in a glass planchette at 116 °C (c) and 110 °C (d). Picture (a) gives a clear planar nematic texture of uniform birefringence with Brownian motion distinctly observed. (b) shows growth of the highly birefringent crystal front as the material crystallizes. Picture (c) again confirms the nematic phase with the traditional schlieren texture that changes in color as the material cools, giving way to the crystal phase in (d).

Upon cooling from the isotropic in a 4 µm planar aligned cell, a smooth uniformly birefringent texture that shimmered, indicative of the nematic phase, was observed. As the material continued to cool, the birefringence changed continuously from green to orange until the crystal grew in. In the glass planchette, a typical schlieren texture of nematics was seen, confirming the formation of the nematic

phase. Further cooling yielded the same crystalline texture observed for the planar aligned cell. Interestingly, the melting point for W1013 was significantly lowered relative to the other azulene BLCs indicating substitution at the 1-position destabilizes the crystal structure. XRD experiments were determined to not be necessary as the POM textures were thought to be conclusive enough for phase determination. This material also did not form the HNF phase.

2.4.5 W1009, W1014, W1015

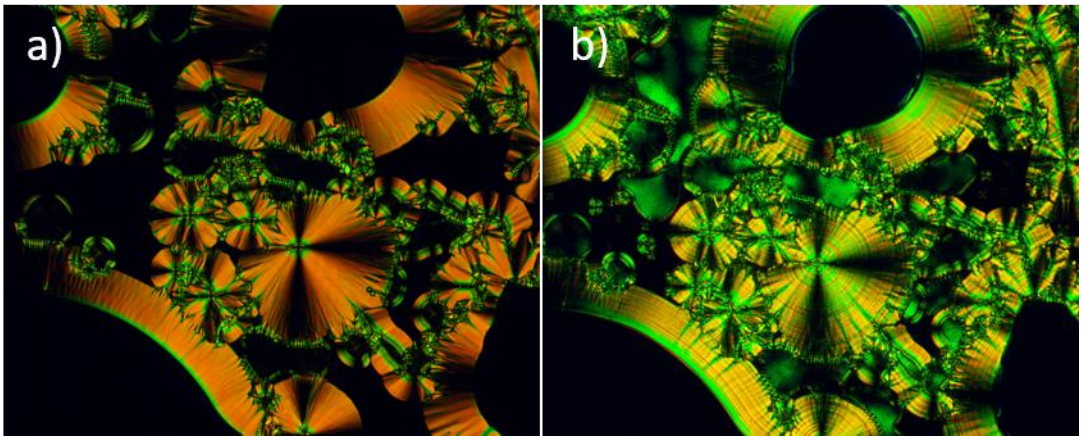

Figure 2.20 – POM Images of W1014 during the first cooling cycle in a 4 µm planar aligned cell. (a) The material at 220 °C showing large ribbon-like domains and focal conics with uniform birefringence. The extinction brushes are aligned with the polarizer and analyzer indication and orthogonal phase. (b) The same region at 105 °C showing the formation of concentric rings, indicating the formation of intralayer ordering. This behavior similar to W1006, a similar compound with the difference in structure being the lack of azomethine linker.

Unfortunately, these materials were not thermally stable and degraded upon heating. Upon initial observation in the POM the textures observed resembled those seen for W1006 (**Figure 2.20**). The materials melted over very broad temperature ranges (10-20 °C) after the first heating cycle in the DSC suggesting that the materials were decomposing in some fashion. In the POM the phase transitions were also observed to be very broad for each material. Interestingly for W1014, the first observation in a cell revealed a texture that resembled that of the HNF phase. Approximately 10% of the field of view had a low birefringent texture that had a faint blue hue. Upon uncrossing the polarizers in either direction revealed domains that switched colors with sign of the decrossing, indicative of the formation of chiral

domains. This, of course, is not sufficient evidence to confirm the presence of filaments, however, it does suggest that the material may be able to adopt either the HNF or DC morphology if given the right conditions (e.g. blended with a small amount of a known HNF forming material.

2.5 Discussion

Unfortunately, none of the synthesized materials formed the HNF phase. Though care was taken to incorporate as many of the defining characteristics of HNF forming compounds as possible, this is further evidence of the sensitive nature of the HNF structure space, confirming the crystalline nature of the filaments. However, though the HNF phase was not realized in these compounds, three new BLC materials with azulene incorporated into either the arm (W1006) or used as the bend-unit (W1007 and W1008) were successfully synthesized. The phenyl azulene material, W1006, with azulene incorporated into the arm was observed to be much more thermally robust than the azomethine linked materials as the compound was successfully cycled through several heating and cooling cycles. The azomethine linker may be susceptible to the strongly nucleophillic 1 and 3 positions on the azulene ring. The high (>220 °C) clearing points of these materials may provide enough energy for the molecules to react with one another, resulting in decomposition of the material. For the flexibly linked materials, the presence of intercalated phases is not unusual, especially when the length of the flexible spacer is comparable to the length of the alkyl tails.[40] Interestingly, the LC behavior of W1006 mimics that of its calamitic arm, which was studied for liquid crystallinity prior to final synthesis of W1006 (see Appendix). This indicates that the azulene core is strongly influencing the behavior of the two phases and is able to overcome any effects from the bent flexible spacer, effectively causing the material to behave as if it were strictly calamitic as opposed to bent. This may be due to the strong polar nature of azulene and the significant enthalpic gain associated with the interaction of neighboring azulene rings.

Compounds W1007 and W1008 with azulene used as the bend-unit were thermally robust, perhaps due to the lowered clearing points of the 1-substituded azulene derivatives and possessed

interesting LC behavior. The polar character of the Schiff base linked azulene portion of the molecule may strongly promote aggregation of these portions of the molecules at the exclusion of the other arm of the bent-core. This coupled with the asymmetry of the compounds could drive the formation of the observed columnar phases as other asymmetrically shaped BLCs form the columnar B1 phase.[39] The fracturing of planar layers (as observed in the B1 phase) into columns would accommodate this type of molecular arrangement and is thought to be the phase observed, though further characterization is necessary.

Compound W1009 and W1014 were observed to have interesting characteristics even though the materials themselves were not thermally stable. W1009 showed an ability to gellate in toluene which is an indication of the formation of a filamentous network structure. Additionally, compound W1014 showed a texture identical to that of the HNF phase in the POM upon loading initial into a cell. The texture was present in only about 10% of the field of view and was dominated by another crystalline texture. However, the characteristic blue color of the HNF phase was seen, and decrossing the polarizers in both directions revealed the formation of large conglomerate domains. It is unclear if there was an anchoring condition that led to the formation of the texture, or if it was a true behavior of the material itself. After heating and cooling, the texture was not observed again giving way to the other crystalline texture. This indicates, at least for W1014, certain conditions exist that may promote the formation of the HNF phase. It would be interesting to make blends of W1014 with a known HNF forming compound (e.g. NOBOW) to see if the morphology of the mixture favored HNF formation.

2.6 Future Work

Historically, investigations into applying azulene to LC systems focused solely on calamitic systems. Bent-core LCs are interesting since they behave as bent calamitic compounds, resulting in polar phases which are symmetry broken. This is highly unusual as the BLC molecules do not need to be chiral, and incorporation of a chromophore into these phases may result in interesting chiral optical

phenomena. Continued work should step back from solely focusing on the HNF phase and study the behavior of all bent-core azulene based LCs as a new family of BLC compounds. The newly developed synthetic methods for synthesis of substituted azulenes can be exploited in creating new BLCs whose structures are only limited by the chemist's imagination.

2.7 Experimental Procedures

All reagents and chemicals were commercial grade, purchased from Sigma-Aldrich or TCI America and were used without purification unless otherwise noted. ^{1}H and ^{13}C NMR spectra were obtained on a 300 MHz Bruker Avance NMR and 500 MHz Varian INOVA spectrometers with chemical shifts reported in ppm relative to $CHCl_3$. Liquid crystallinity was characterized by polarized optical microscopy, differential scanning calorimetry, and x-ray diffraction. Absorption spectra were obtained using spectrophotometric grade dichloromethane as the solvent. Purification by chromatography was done on silica gel with mixtures of hexanes/ethyl acetate as the elution solvent.

2.7.1 Total Synthesis of W1006

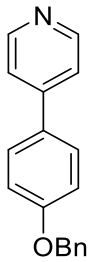

*4-[4-(benzyloxy)phenyl]pyridine (**1**)* – To a flame dried and argon purged 250 mL flask equipped with a stir bar was added 60 mL anhydrous DMF. 4-bromopyridinium bromide (3.92 g, 0.021 mol), 4-(benzyloxy)phenylboronic acid (4.69 g, 0.021 mol), and K_2CO_3 (11.44 g, 0.083 mol) were added and the mixture was sparged with argon form 30 minutes. $Pd(PPh_3)_4$ (2.31 g, 5 mol%) was then added and the solution sparged again with argon and heated to 90 °C and allowed to react for three days. Upon completion of the reaction, the solution was cooled to room temperature and poured into 300 mL water. The aqueous mixture was then extracted with ether, the layers separated, and the organic portion dried over $MgSO_4$. The solvent was removed in vacuo and the crude material was purified by column chromatography using a gradient of 1:1 hexanes/ethyl acetate to 4:1 ethyl acetate/hexanes to give 2.65 of **1** as a white powder in a 50% yield. This is a previously reported compound. ^{1}H NMR (500 MHz, Methylene Chloride-d_2) δ 8.70 – 8.55 (m, 2H), 7.72 – 7.61 (m, 2H), 7.53 – 7.51 (m, 2H), 7.51 – 7.48 (m, 2H), 7.46 – 7.41 (m, 2H), 7.40 – 7.36 (m, 1H), 7.17 – 7.06 (m, 2H), 5.16 (s, 2H).

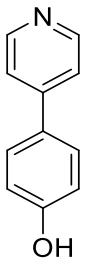

4-(pyridin-4-yl)phenol (**2**) – To a flame dried and argon purged 250 mL flask equipped with a stir bar was added 100 mL absolute methanol. Compound **1** (2.63 g, 0.010 mol) was added to the solution along with

Pd/C (0.293 g, 10% by mass) and the mixture was cycled through seven vacuum/back fill with argon cycles to purge the system of air. The mixture was then placed under an atmosphere of H_2 gas and reaction progress was monitored by TLC. Every hour more Pd/C was added to replenish any poisoned catalyst for three hours and the reaction was allowed to proceed overnight when it finally came to completion. Upon completion the reaction mixture was placed under an atmosphere of argon, and filtered through a celite pad to remove the catalyst. Removal of the solvent in vacuo yielded 1. 52 g of **2** as a white powder in an 88% yield. This is a previously reported compound. ^{1}H NMR (500 MHz, DMSO-d_6) δ 9.83 (s, 1H), 8.63 – 8.44 (m, 2H), 7.69 – 7.64 (m, 2H), 7.64 – 7.59 (m, 2H), 6.93 – 6.85 (m, 2H).

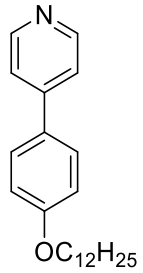

4-[4-(dodecyloxy)phenyl]pyridine (**3**) – To a 100 mL flask equipped with a stir bar was added 30 mL DMF. Compound **2** (1.52 g, 0.088 mol) was dissolved in the DMF and K_2CO_3 (1.92 g, 0.014 mol) was added and allowed to react for five minutes. 1-bromododecane (2.5 mL, 0.010 mol) was then added via syringe and the solution was heated to 70 °C for two days. Upon completion of the reaction, the mixture was poured into 300 mL water and extracted with ether. The layers were separated, and the organic layer was dried over $MgSO_4$. The solvent was evaporated in vacuo and the crude material was columned in 1:1 hexanes/ethyl acetate to give 2.51 g **3** as a white powder in an 83% yield. This is a previously reported compound. ^{1}H NMR (300 MHz, Methylene Chloride-d_2) δ 8.65 – 8.56 (m, 2H), 7.69 – 7.61 (m, 2H), 7.55 – 7.47 (m, 2H), 7.07 – 7.00 (m, 2H), 4.04 (t, *J* = 6.6 Hz, 2H), 1.83 (dq, *J* = 8.2, 6.6 Hz, 2H), 1.50 (qd, *J* = 7.3, 6.8, 4.0 Hz, 2H), 1.42 – 1.18 (m, 7H), 0.96 – 0.87 (m, 3H).

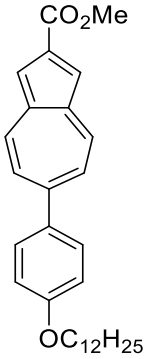

Methyl-6-[4-(dodecyloxy)phenyl]azulene-2-carboxylate (**4**) – To a flame dried and argon purged 500 mL three neck flask equipped with a reflux condenser and a stir bar was added 300 mL anhydrous toluene. Compound **3** (3.30 g, 0.010 mol) was dissolved completely in the toluene and the solution was cooled to 0 °C in an ice bath. Triflic anhydride (2.6 mL, 0.015 mol) was slowly added dropwise and a yellow precipitate quickly formed. Distilled diethylamine (5.5 ml, 0.053 mol) was slowly added dropwise and the solution quickly turned bright red then dark red. $CpCO_2Me$ (2.92 g, 0.020 mol) was then added in one portion and the solution turned black. The mixture was then heated to reflux overnight. Upon completion of the reaction, the mixture was cooled to room temperature, silica was added, and the solvent was removed in vacuo. The silica was then loaded on a column and the purple and blue spots were collected by elution in $HCCl_3$. Final purification was obtained by recrystallization in hexanes to give 1.11 g **4** as blue crystals in a 22% yield. ^{1}H NMR (300 MHz, Methylene Chloride-d_2) δ 8.58 – 8.40 (m, 2H), 7.76 (s, 2H), 7.72 – 7.60 (m, 2H), 7.47 (ddd, *J* = 9.9, 1.1, 0.5 Hz, 2H), 7.11 – 6.99 (m, 2H), 4.07 (t, *J* = 6.6 Hz, 2H), 3.97 (s, 3H), 1.85 (dt, *J* = 14.3, 6.6 Hz, 2H), 1.56 (s, 3H), 1.45 – 1.21 (m, 15H), 1.04 – 0.80 (m, 3H).

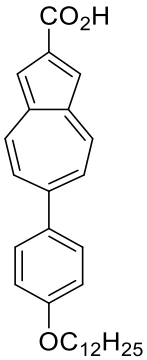

6-[4-(dodecyloxy)phenyl]azulene-2-carboxylic acid (**5**) – In a 50 mL flask equipped with a stir bar and reflux condenser was added 10 mL THF. Compound **4** (1.11 g, 0.0022 mol) was dissolved completely, and 10 mL water was added. LiOH*H_2O (0.982 g, 0.023 mol) was added and the solution was brought to reflux and reacted overnight. Upon completion of the reaction, the solution was cooled to room temperature, acidified to pH=1 and filtered to give 0.800 g of **5** as a blue powder in a 74% yield. ^{1}H NMR (300 MHz, DMSO-d_6) δ 8.32 (d, *J* = 10.2 Hz, 2H), 7.74 – 7.59 (m, 2H), 7.45 (s, 2H), 7.31 (d, *J* = 10.2 Hz, 2H), 7.15 – 6.96 (m, 2H), 4.04 (t, *J* = 6.5 Hz, 2H), 1.73 (q, *J* = 7.0 Hz, 2H), 1.26 (s, 13H), 0.95 – 0.74 (m, 3H).

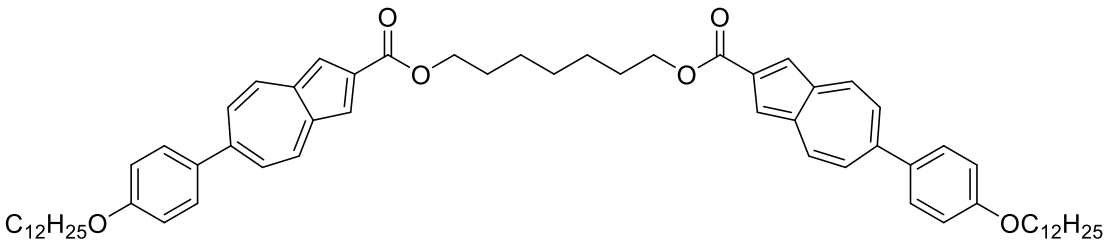

7-{6-[4-(dodecyloxy)phenyl]azulene-2-carbonyloxy}heptyl-6-[4-(dodecyloxy)phenyl]azulene-2-carboxylate (**6**) **W1006** – To a flame dried and argon purged pear flask equipped with a stir bar was added 4 mL anhydrous DMF. Compound **5** (0.400 g, 0.0009 mol) was dissolved in the DMF and Cs_2CO_3 (0.596 g, 0.0018 mol) was added. The mixture was then heated to 90 °C and stirred for one hour. 1,7-dibromoheptane (0.109 g, 0.0004 mol) was added dropwise via syringe and the reaction was allowed to proceed for two days. The reaction mixture was then cooled to room temperature and poured into water and filtered through a Hirsch funnel. The crude solid was purified by column chromatography in $HCCl_3$ and recrystallized twice from toluene to give 0.070 g (**6**) **W1006** as a blue powder in a 17% yield. ^{1}H NMR (500 MHz, Methylene Chloride-d_2) δ 8.50 – 8.38 (m, 4H), 7.76 (s, 4H), 7.67 – 7.58 (m, 4H), 7.48 – 7.37 (m, 4H), 7.07 – 6.98 (m, 4H), 4.39 (t, *J* = 6.6 Hz, 4H), 4.05 (t, *J* = 6.6 Hz, 4H), 1.93 – 1.78 (m, 8H), 1.32 (d, *J* = 13.0 Hz, 29H), 1.01 – 0.80 (m, 6H). ^{13}C NMR (75 MHz, Methylene Chloride-d_2) δ 165.57, 160.03, 153.88, 139.59, 129.78, 124.06, 118.87, 114.82, 68.26, 64.62, 54.12, 53.76, 53.40, 53.04, 52.68, 31.91,

29.65, 29.63, 29.60, 29.58, 29.38, 29.34, 29.22, 28.70, 25.99, 25.96, 22.68, 13.85. HRMS $[M-H]^+$ -1.4 ppm at 961.6346.

2.7.2 Total Synthesis of W1007, W1008, W1013, W1014, W1015

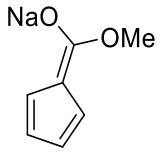

Sodium 1-methyl-cyclopentadienylidecarboxylate (**7**) – This compound was synthesized using a modified procedure from [ref]. To a flame dried and argon purged flask was added a 2.4 M solution of sodium cyclopentyldienylide (49 mL, 0.118 mol) in THF via syringe. To the reddish pink solution was added dimethyl carbonate (11 mL, 0.131 mol) and the resulting mixture was brought to reflux overnight. The resultant reddish-brown solution was cooled to room temperature and the solvent was removed in vacuo giving a greyish pink solid. The solid washed with ether, filtered, and washed again with 200 mL ether until the filtrate ran clear. The grey powder was dried under vacuum giving 13.73 g of **7** in an 80% yield. 1H NMR (300 MHz, DMSO-d6) δ 6.17 – 5.98 (m, 2H), 5.57 – 5.41 (m, 2H), 3.45 (s, 3H). 13C NMR (75 MHz, DMSO-d6) δ 166.47, 111.56, 109.38, 108.48, 49.07, 48.94.

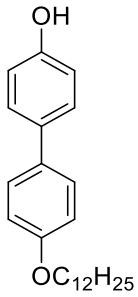

4'-(undecyloxy)-[1,1'-biphenyl]-4-ol (**8**)– This compound was synthesized according to the procedure reported in reference X. ^{1}H NMR (300 MHz, Chloroform-*d*) δ 7.46 (ddd, *J* = 9.9, 6.0, 2.6 Hz, 4H), 7.09 – 6.75 (m, 4H), 4.81 (s, 1H), 4.01 (t, *J* = 6.6 Hz, 2H), 1.82 (dq, *J* = 8.2, 6.6 Hz, 2H), 1.32 (d, *J* = 15.7 Hz, 18H),

0.99 – 0.80 (m, 3H). ^{13}C NMR (75 MHz, Chloroform-*d*) δ 154.57, 127.93, 127.66, 127.65, 115.57, 114.77, 114.76, 77.21, 68.13, 31.92, 29.67, 29.64, 29.60, 29.59, 29.41, 29.35, 29.32, 26.07, 22.69, 14.11.

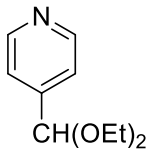

4-(diethoxymethyl)pyridine (**9**) – This is a previously reported compound and was prepared using a procedure used by Estdale et al. with slight modifications and is described below. To a flame dried and argon purged flask was added 88 mL of absolute ethanol. The flask was cooled to 0° C in an ice bath and acetyl bromide (12.0 mL, 0.162 mol) was added dropwise. The ice bath was removed and to the resulting pale, clear tan solution was dropwise added 4-pyridinecarboxaldehyde (9.5 mL, 0.128 mol). The solution was stirred at room temperature overnight and a white precipitate formed. 85 mL of toluene was then added and the solvents were removed *in vacuo*. To the resulting bright yellow solid was added 120 mL of a 10% by weight solution of K_2CO_3 giving a pale-yellow oil. The solution was extracted 3X75 mL ether and the organic layer was dried over $MgSO_4$. The ether was removed *in vacuo* resulting in a clear oil that was used in the next step without further purification. ^{1}H NMR (300 MHz, Chloroform-*d*) δ 8.61 (dt, *J* = 4.5, 1.0 Hz, 2H), 7.45 – 7.30 (m, 2H), 5.49 (s, 1H), 3.71 – 3.41 (m, 4H), 1.41 – 1.09 (m, 6H). ^{13}C NMR (75 MHz, Chloroform-*d*) δ 191.44, 149.89, 121.62, 99.77, 61.16, 15.12.

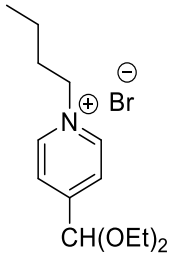

1-butyl-4-(diethoxymethyl)pyridin-1-ium bromide (**10**) – This is a previously reported compound and was prepared using the procedure reported by Estdale et al. Compound **9** (4.99g, 0.028 mol)was massed into

a flask equipped with a reflux condenser and dissolved in 14 mL of absolute ethanol. Butyl bromide (4.6 mL, 0.041 mol) was added to the pale-yellow solution and heated to reflux overnight. The reflux condenser was replaced with a distillation head and the ethanol and butyl bromide were distilled off leaving a viscous, dark amber oil that was used without further purification in the next step. ^{1}H NMR (300 MHz, Chloroform-*d*) δ 9.73 – 9.63 (m, 2H), 8.09 – 8.00 (m, 2H), 5.59 (s, 1H), 4.99 (t, *J* = 7.4 Hz, 2H), 3.55 (q, *J* = 7.0 Hz, 4H), 2.06 – 1.92 (m, 2H), 1.45 – 1.29 (m, 2H), 1.18 (t, *J* = 7.0 Hz, 6H), 0.95 – 0.82 (m, 3H). ^{13}C NMR (75 MHz, Chloroform-*d*) δ 157.53, 145.36, 126.05, 98.24, 62.38, 61.15, 33.86, 19.26, 15.02, 13.51, 13.47.

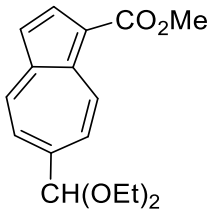

Methyl-6-(diethoxymethyl)azulene-1-carboxylate (**11**) – To a flame dried and argon purged flask was massed compound **10** (7.13 g, 0.022 mol). Freshly distilled THF (50 mL) was added via syringe and the dark solution was cooled to 0° C in an ice bath. Diethylamine (11.5 mL, 0.111 mol) was added dropwise via syringe and the solution turned a dark red/brown. The ice bath was then removed and compound **7** was added in one portion. The mixture was then heated to reflux. After 60 Hours at reflux, the black solution was cooled to room temperature and silica gel was added. The silica was then dry loaded on to a column and the purple and blue spots were eluted using a 9:1-8:2 hexanes/ethyl acetate gradient. Once the purple and blue bands were collected, the solvents were evaporated, and the mixture was loaded on to a column and eluted using a 95:5-9:1 gradient of hexanes/ethyl acetate yielding 1.31 g of **10** as a dark purple oil in a 21% yield. ^{1}H NMR (300 MHz, Methylene Chloride-d_2) δ 9.65 (d, *J* = 10.4 Hz, 1H), 8.54 (d, *J* = 10.1 Hz, 1H), 8.36 (d, *J* = 4.2 Hz, 1H), 7.75 (ddd, *J* = 18.2, 10.3, 1.5 Hz, 2H), 7.33 (d, *J* = 4.1 Hz, 1H), 5.58 (s, 1H), 3.96 (s, 3H), 3.80 – 3.53 (m, 4H), 1.28 (t, *J* = 7.0 Hz, 6H). ^{13}C NMR (75 MHz,

Methylene Chloride-d_2) δ 166.08, 150.45, 144.87, 140.82, 140.69, 138.13, 137.47, 126.85, 125.99, 118.13, 117.42, 104.44, 62.66, 51.48, 15.56.

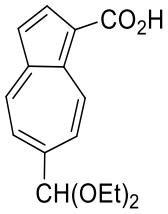

6-(diethoxymethyl)azulene-1-carboxylic acid (**12**) – Compound **11** (0.724 g, 0.0025 mol) was dissolved in THF (12 mL) and water (12 mL) was added. LiOH*H_2O (1.05 g, 0.025 mol) was added in one portion and the solution was brought to reflux and allowed to reflux for five days until TLC indicated consumption of the starting material. The solution was then cooled to 0° C in an ice bath and conc. HCl was added dropwise until the solution was pH=1. The solution was then quickly extracted three times with 25 mL of $HCCl_3$ and the organic layer was dried over $MgSO_4$. The solvent was evaporated, and the crude material was sonicated in hexanes to yield 0.540 g of purple crystals of **12** in a 79% yield. ^{1}H NMR (300 MHz, Methylene Chloride-d_2) δ 12.41 (s, 1H), 9.73 (d, *J* = 10.4 Hz, 1H), 8.59 (d, *J* = 10.1 Hz, 1H), 8.50 (dd, *J* = 4.1, 1.1 Hz, 1H), 7.84 (ddd, *J* = 21.0, 10.3, 1.5 Hz, 2H), 7.38 (d, *J* = 4.2 Hz, 1H), 5.61 (s, 1H), 3.84 – 3.51 (m, 4H), 1.30 (t, *J* = 7.0 Hz, 6H). ^{13}C NMR (75 MHz, Methylene Chloride-d_2) δ 170.65, 150.17, 145.20, 141.14, 141.10, 137.81, 137.17, 126.97, 126.20, 124.50, 121.41, 117.99, 115.86, 112.00, 103.73, 62.10, 14.97.

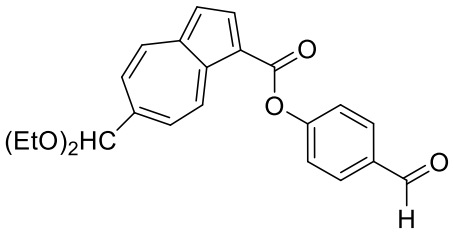

4-formylphenyl 6-(diethoxymethyl)azulene-1-carboxylate (**13**) – Compound **12** (0.303 g, 0.0011 mol) was massed into a 50 mL round bottomed flask equipped with a stir bar. DCM (11 mL) was added and resulted in a dark purple solution. 4-hydroxybenzaldehyde (0.273 g, 0.0023 mol), DMAP (cat.), and EDC

(0.247 g, 0.0013 mol) were added and allowed to react at room temperature for two days. Upon completion of the reaction, the reaction mixture was washed with water, the layers separated, and the organic portion dried over $MgSO_4$. The solvent was removed in vacuo, and the crude material purified by column chromatography using 4:1 hexanes/ethyl acetate as the elution solvent giving 0.157 g **13** as a purple oil in a 38% yield. ^{1}H NMR (300 MHz, Chloroform-*d*) δ 10.06 (s, 1H), 9.69 (d, *J* = 10.3 Hz, 1H), 8.62 – 8.51 (m, 2H), 8.07 – 7.97 (m, 2H), 7.97 – 7.77 (m, 2H), 7.55 – 7.45 (m, 2H), 7.37 (d, *J* = 4.2 Hz, 1H), 3.79 – 3.54 (m, 4H), 1.29 (td, *J* = 7.1, 4.3 Hz, 6H).

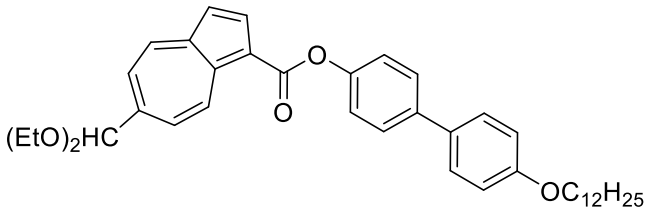

4'-(undecyloxy)-[1,1'-biphenyl]-4-yl-6-(diethoxymethyl)azulene-1-carboxylate (**14**) – To a 25 ml flask equipped with a stir bar was massed compound **11** (0.326 g, 0.0012 mol) and compound **8** (0.846 g, 0.0024 mol). 10 mL of DCM was then added along with one crystal of DMAP. To the resulting purple suspension was added EDC (0.258 g, 0.0013 mol) and stirred at room temperature for six days. Upon completion of the reaction, the reaction mixture was diluted with DCM and silica gel was added. The solvent was removed in vacuo and the dry silica was added to the top of a column and eluted with 9:1 hexanes/ethyl acetate to give **14** as a purple solid (0.356 g) in a 49% yield. ^{1}H NMR (300 MHz, Methylene Chloride-d_2) δ 8.66 – 8.54 (m, 1H), 7.83 (ddd, *J* = 14.7, 10.4, 1.5 Hz, 1H), 7.72 – 7.63 (m, 1H), 7.63 – 7.45 (m, 1H), 7.45 – 7.31 (m, 1H), 7.08 – 6.92 (m, 1H), 4.03 (dt, *J* = 9.8, 6.6 Hz, 1H), 3.81 – 3.55 (m, 2H), 1.92 – 1.77 (m, 1H), 1.41 – 1.23 (m, 11H), 0.98 – 0.87 (m, 1H).

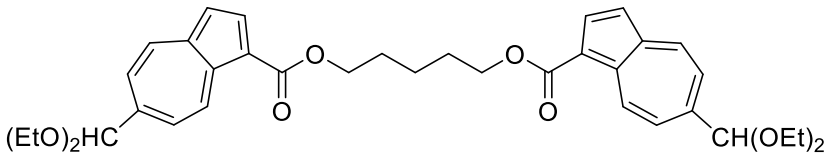

5-[6-(diethoxymethyl)azulene-1-carbonyloxy]pentyl 6-(diethoxymethyl)azulene-1-carboxylate (**15**) – Compound **12** (0.570 g, 0.002 mol) was massed into a 10 mL round bottomed flask equipped with a stir bar and reflux condenser. 4 mL of anhydrous ACN was added along with K_2CO_3 (0.613 g, 0.0044 mol) and one crystal of KI. Then 1,5-dibromopentane (0.202 g, 0.001 mol) was added via syringe and the solution was brought to reflux for five days. Upon completion of the reaction, the reaction mixture was filtered, and the solvent was removed *in vacuo*. The crude material was purified by column chromatography using 9:1 hexanes/ethyl acetate as the elution solvent to give 0.520 g of **15** as a viscous dark purple oil in a 96% yield. ^{1}H NMR (300 MHz, Methylene Chloride-d_2) δ 8.64 (s, 2H), 8.42 – 8.21 (m, 4H), 8.16 – 8.00 (m, 4H), 7.67 – 7.47 (m, 1H), 7.41 – 7.16 (m, 7H), 7.05 – 6.90 (m, 4H), 4.03 (t, *J* = 6.6 Hz, 4H), 1.83 (dt, *J* = 14.0, 6.7 Hz, 4H), 1.32 (s, 40H), 1.02 – 0.81 (m, 6H). ^{13}C NMR (75 MHz, Methylene Chloride-d_2) δ 156.11, 130.45, 128.45, 122.42, 119.35, 114.98, 68.35, 29.62, 29.58, 29.38, 29.33, 26.00, 22.67.

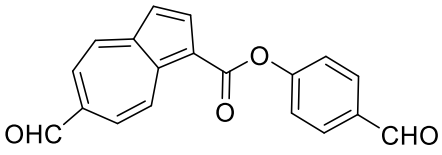

4-formylphenyl-6-formylazulene-1-carboxylate (**16**) – Compound **13** (0.157 g, 0.0004 mol) was dissolved in 17 mL of DCM and transferred to a 50 mL round bottomed flask equipped with a stir bar. 8.5 mL of 2M HCl was added and the mixture was stirred vigorously. After four days of stirring, the reaction was stopped, and the layers were separated. The organic layer was dried over $MgSO_4$ and the solvent was removed *in vacuo* giving 0.068g of **15** as a greenish powder in a 54% yield. ^{1}H NMR (500 MHz, Chloroform-*d*) δ 10.23 (s, 1H), 10.07 (s, 1H), 9.86 (d, *J* = 10.0 Hz, 1H), 8.76 – 8.71 (m, 2H), 8.15 (dd, *J* = 10.1, 1.4 Hz, 1H), 8.10 (dd, *J* = 9.9, 1.4 Hz, 1H), 8.07 – 8.00 (m, 2H), 7.54 – 7.47 (m, 3H). The compound was too insoluble to obtain a ^{13}C NMR.

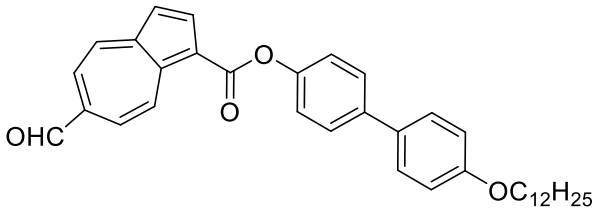

4'-(undecyloxy)-[1,1'-biphenyl]-4-yl-6-formylazulene-1-carboxylate (**17**) – Compound **14** (0.356 g, 0.0006 mol) was massed into a 50 mL flask with stir bar. 25 mL of DCM were added and to the purple solution was added 12 ml 2M HCl dropwise. The reaction proceeded at room temperature for two days. Upon completion of the reaction the layers were separated, and the organic layer was dried over $MgSO_4$. The crude material was triturated with refluxing hexanes and filtered resulting in 0.191 g of green crystals in a 61% yield. ^{1}H NMR (500 MHz, Methylene Chloride-d_2) δ 10.23 (s, 1H), 9.88 (d, *J* = 10.1 Hz, 1H), 8.80 – 8.74 (m, 2H), 8.15 (dd, *J* = 10.1, 1.4 Hz, 1H), 8.09 (dd, *J* = 9.9, 1.4 Hz, 1H), 7.71 – 7.65 (m, 2H), 7.63 – 7.57 (m, 2H), 7.56 (d, *J* = 4.1 Hz, 1H), 7.39 – 7.33 (m, 2H), 7.05 – 6.99 (m, 2H), 4.04 (t, *J* = 6.6 Hz, 2H), 1.88 – 1.79 (m, 2H), 1.56 – 1.46 (m, 2H), 1.36 – 1.29 (m, 14H), 0.95 – 0.88 (m, 3H). The material was too insoluble to obtain a ^{13}C NMR.

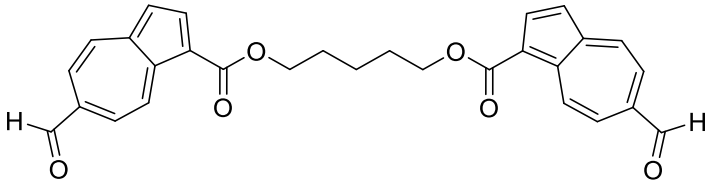

5-(6-formylazulene-1-carbonyloxy)pentyl-6-formylazulene-1-carboxylate (**18**) – Compound **15** (0.495 g, 0.0008 mol) was massed into a 10 mL round bottomed flask equipped with a stir bar. The solid was dissolved in 2 mL THF and 2 mL of a 10% v/v HCl solution was added and the reaction was allowed to proceed overnight. Upon completion, the reaction was neutralized with saturated aqueous $NaHCO_3$, and the aqueous portion was extracted with $HCCl_3$. The organic layer was dried over $MgSO_4$ and the solvent was removed *in vacuo*. The crude material was purified by column chromatography using 7:3 hexanes/ethyl acetate as the elution solvent to yield 0.170 g of **18** as a green solid in a 45% yield. ^{1}H

NMR (300 MHz, Chloroform-*d*) δ 10.16 (s, 2H), 9.79 (d, *J* = 10.1 Hz, 2H), 8.61 (d, *J* = 9.9 Hz, 2H), 8.54 (d, *J* = 4.1 Hz, 2H), 8.05 – 7.91 (m, 4H), 7.37 (d, *J* = 4.1 Hz, 2H), 4.48 (t, *J* = 6.4 Hz, 4H), 2.10 – 1.91 (m, 4H), 1.85 – 1.71 (m, 2H). This compound was too insoluble to obtain a ^{13}C NMR.

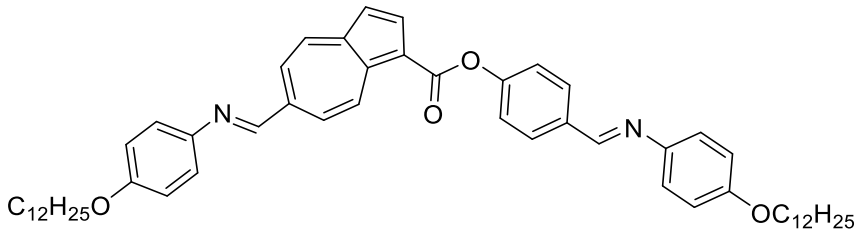

4-[(E)-{[4-(undecyloxy)phenyl]imino}methyl]phenyl-6-[(E)-{[4-(undecyloxy)phenyl]imino}methyl]azulene-1-carboxylate (**19**) **W1007** – Compound **16** (0.0.069 g, 0.00022 mol) was massed into a 25 mL flask with a stir bar. 10 mL 200 proof ethanol was added via syringe and 4-dodecyloxy aniline (0.258 g, 0.0009 mol) was massed into the reaction mixture. One drop acetic acid was added along with a reflux condenser. The reaction mixture was refluxed overnight. Upon completion of the reaction, the mixture was cooled in the freezer and the crude material was filtered and washed with cold ethanol. The crude material was recrystallized in toluene and DCM to give 0.176g of **18** as green crystals in a 94% yield. ^{1}H NMR (500 MHz, Methylene Chloride-d_2) δ 9.76 (d, *J* = 10.4 Hz, 1H), 8.76 (s, 1H), 8.68 (d, *J* = 10.2 Hz, 1H), 8.60 (d, *J* = 4.1 Hz, 1H), 8.57 (s, 1H), 8.28 (ddd, *J* = 29.0, 10.4, 1.5 Hz, 2H), 8.07 – 7.98 (m, 2H), 7.51 – 7.35 (m, 5H), 7.33 – 7.24 (m, 2H), 7.06 – 6.92 (m, 4H), 4.03 (dt, *J* = 10.8, 6.6 Hz, 4H), 1.82 (pd, *J* = 6.7, 4.6 Hz, 4H), 1.50 (d, *J* = 15.6 Hz, 4H), 1.44 – 1.24 (m, 32H), 0.91 (td, *J* = 7.0, 1.4 Hz, 6H). This compound was too insoluble to obtain a ^{13}C NMR. HRMS $[M-H]^+$ -1.7 ppm off at 823.5414.

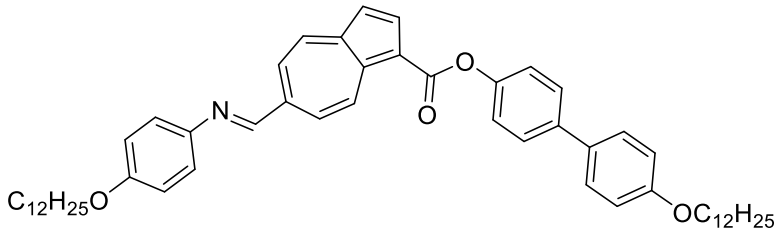

4'-(undecyloxy)-[1,1'-biphenyl]-4-yl-6-[(E)-{[4-(undecyloxy)phenyl]imino}methyl]azulene-1-carboxylate (**19**) **W1008** – Compound **17** (0.183 g, 0.0004 mol) was massed into a 25 mL flask with a stir bar. 10 mL 200 proof ethanol was added via syringe and to the resulting suspension was added 4-dodecyloxy aniline. A reflux condenser was added, and the reaction mixture was refluxed for two days. Upon completion of the reaction, the reaction mixture was cooled in the freezer. The crude material was filtered and washed with cold ethanol and finally recrystallized three times in DCM to give 0.209 g of **W1008** as green crystals in a 77% yield.^{1}H NMR (500 MHz, Methylene Chloride-d_2) δ 9.76 (d, *J* = 10.4 Hz, 1H), 8.76 (s, 1H), 8.67 (d, *J* = 10.3 Hz, 1H), 8.61 (d, *J* = 4.2 Hz, 1H), 8.27 (ddd, *J* = 28.8, 10.3, 1.5 Hz, 2H), 7.70 – 7.64 (m, 2H), 7.63 – 7.57 (m, 2H), 7.45 (d, *J* = 4.1 Hz, 1H), 7.44 – 7.39 (m, 2H), 7.39 – 7.33 (m, 2H), 7.07 – 6.95 (m, 4H), 4.04 (td, *J* = 6.6, 2.8 Hz, 4H), 1.83 (pd, *J* = 6.7, 2.6 Hz, 4H), 1.54 – 1.46 (m, 4H), 1.31 (s, 32H), 0.91 (td, *J* = 7.0, 1.6 Hz, 6H). This compound was too insoluble to obtain a ^{13}C NMR. HRMS $[M-H]^+$ -2.4 ppm off at 987.6251.

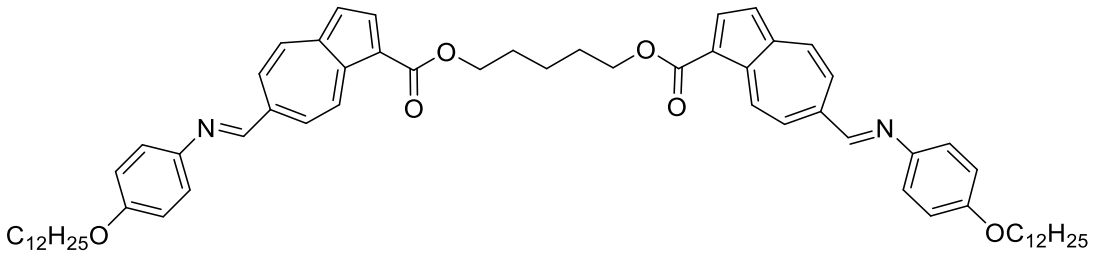

5-{6-[(E)-{[4-(dodecyloxy)phenyl]imino}methyl]azulene-1-carbonyloxy}pentyl-6-[(E)-{[4-(dodecyloxy)phenyl]imino}methyl]azulene-1-carboxylate (**20**) **W1013** – Compound **18** (0.150 g, 0.0003 mol) was massed into a flame dried and argon purged 10 mL pear flask equipped with a stir bar. 4-dodecyloxyaniline (0.336 g, 0.0012 mol) was added along with 4 mL 200 proof ethanol. Two drops of

glacial acetic acid were added, and the solution was brought to reflux overnight. The reaction was then cooled in the freezer and filtered through a Hirsch funnel. The crude material was purified by recrystallization from hexanes to give 0.263 g of **W1013** as green crystals in a 74% yield. ^{1}H NMR (300 MHz, Methylene Chloride-d_2) δ 9.66 (d, J = 10.4 Hz, 2H), 8.63 (s, 2H), 8.53 (d, J = 10.2 Hz, 2H), 8.38 (d, J = 4.1 Hz, 2H), 8.16 (dd, J = 10.2, 1.5 Hz, 2H), 8.07 (dd, J = 10.5, 1.5 Hz, 2H), 7.43 – 7.31 (m, 4H), 7.27 (d, J = 4.1 Hz, 2H), 7.05 – 6.94 (m, 4H), 4.47 (t, J = 6.3 Hz, 4H), 4.03 (t, J = 6.6 Hz, 4H), 1.99 (p, J = 6.7 Hz, 4H), 1.91 – 1.73 (m, 7H), 1.57 (s, 6H), 1.48 – 1.27 (m, 37H), 0.98 – 0.87 (m, 6H). ^{13}C NMR (75 MHz, Methylene Chloride-d_2) δ 159.06, 141.33, 136.98, 136.34, 127.96, 125.99, 122.77, 118.20, 115.03, 68.37, 63.65, 54.12, 53.76, 53.40, 53.04, 52.68, 29.66, 29.63, 29.60, 29.58, 29.40, 29.34, 29.27, 28.65, 26.01, 22.68. HRMS $[M-H]^+$ -1.7 ppm off at 987.6251.

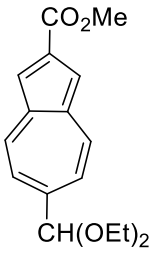

Methyl 6-(diethoxymethyl)azulene-2-carboxylate (**21**) - To a flame dried and argon purged flask was massed compound **10** (7.13 g, 0.022 mol). Freshly distilled THF (50 mL) was added via syringe and the dark solution was cooled to 0° C in an ice bath. Diethylamine (11.5 mL, 0.111 mol) was added dropwise via syringe and the solution turned a dark red/brown. The ice bath was then removed and compound **7** was added in one portion. The mixture was then heated to reflux. After 60 Hours at reflux, the black solution was cooled to room temperature and silica gel was added. The silica was then dry loaded on to a column and the purple and blue spots were eluted using a 9:1-8:2 hexanes/ethyl acetate gradient. Once the purple and blue bands were collected, the solvents were evaporated, and the mixture was loaded on to a column and eluted using a 95:5-9:1 gradient of hexanes/ethyl acetate yielding 1.31 g of **21** as dark blue crystals in a 21% yield. ^{1}H NMR (300 MHz, Chloroform-*d*) δ 8.45 (d, *J* = 10.6 Hz, 2H), 7.79 (s, 2H), 7.77 – 7.65 (m, 1H), 7.48 – 7.38 (m, 2H), 5.48 (s, 1H), 3.98 (d, *J* = 3.3 Hz, 3H), 3.78 – 3.52 (m, 4H), 1.28 (t, *J* = 7.1 Hz, 6H).

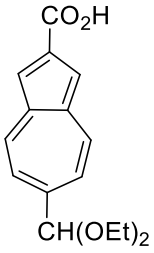

6-(diethoxymethyl)azulene-2-carboxylic acid (**22**) – Compound **21** (0.930 g, 0.0033 mol) was massed into a 50 mL flask with a stir bar. 30 mL of a 1:1 THF/Water solution was then added and giving a dark blue solution. LiOH*H_2O (1.44 g, 0.035 mol) was then added to the solution and brought to reflux overnight.

The reaction was cooled to room temperature and transferred to a 100 mL flask using water. The solution was then cooled to 0 °C in an ice bath and con HCl was added to bring the pH of the solution to 1. The mixture was then quickly extracted with chloroform, the layers separated, and the organic portion dried over $MgSO_4$. After removal of the solvent, the crude solid was recrystallized from ethanol to give 0.720g **22** as blue crystals in an 81% yield. ^{1}H NMR (300 MHz, Chloroform-*d*) δ 8.53 – 8.44 (m, 2H), 7.86 (s, 2H), 7.46 (d, *J* = 10.1 Hz, 2H), 5.50 (s, 1H), 3.66 (ddq, *J* = 30.5, 9.4, 7.1 Hz, 4H), 1.29 (t, *J* = 7.1 Hz, 6H).

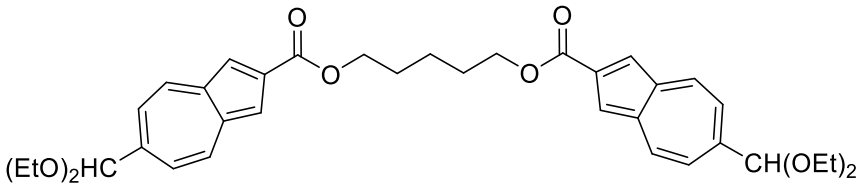

5-[6-(diethoxymethyl)azulene-2-carbonyloxy]pentyl 6-(diethoxymethyl)azulene-2-carboxylate (**23**) – 26 mL of DMF was added to a 50 mL flask with stir bar. Compound **22** (0.720 g, 0.0026 mol) was then massed and dissolved in the DMF to give a blue solution. K_2CO_3 (1.58 g, 0.011 mol) was added and allowed to react for five minutes. 1,5-dibromopentane (0.250 g, 0.001 mol) was then added via syringe and a few KI crystals were added. The reaction proceeded for two days at room temperature. Upon completion, the reaction was quenched with 75 mL water and extracted with ether. The organic layer was separated and dried over $MgSO_4$ and the solvent was removed in vacuo. The crude material was purified via column chromatography with a 4:1 hexanes/ethyl acetate to pure ethyl acetate gradient, giving 0.550 g **23** as a viscous blue oil in an 82% yield. ^{1}H NMR (300 MHz, Chloroform-*d*) δ 8.49 – 8.35 (m, 2H), 7.78 (s, 2H), 7.42 (d, *J* = 10.1 Hz, 2H), 5.48 (s, 1H), 4.45 (t, *J* = 6.5 Hz, 2H), 3.65 (ddq, *J* = 30.7, 9.4, 7.0 Hz, 4H), 1.95 (p, *J* = 6.8 Hz, 2H), 1.73 (tt, *J* = 9.9, 5.8 Hz, 1H), 1.29 (t, *J* = 7.0 Hz, 6H).

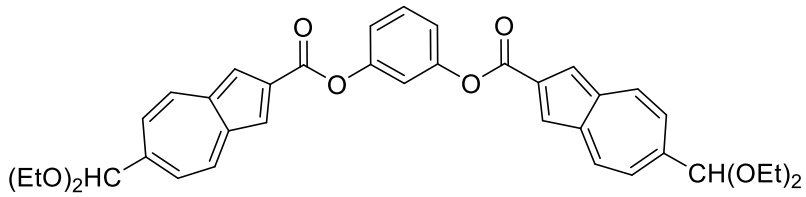

3-[6-(diethoxymethyl)azulene-2-carbonyloxy]phenyl 6-(diethoxymethyl)azulene-2-carboxylate (**24**) – compound **22** (0.165 g, 0.0006 mol) and resorcinol (0.027g, 0.0003 mol) were massed into a 25 ml flask with a stir bar. DCM (6 ml) was added along with one crystal of DMAP. EDC (0.133 g, 0.0007 mol) was then added and the reaction was stirred for six days. Upon reaction completion, the reaction mixture was diluted with DCM and washed with conc. $NaHCO_3$ solution. The organic layer was separated and dried over $MgSO_4$ and the solvent was removed in vacuo. The crude material was purified via column chromatography using 4:1 hexanes/ethyl acetate as the elution solvent giving 0.180g **22** as a blue solid in a 48% yield. ^{1}H NMR (300 MHz, Methylene Chloride-d_2) δ 8.60 – 8.51 (m, 4H), 7.95 (s, 4H), 7.58 (ddd, *J* = 8.3, 7.8, 0.5 Hz, 1H), 7.54 – 7.46 (m, 4H), 7.35 – 7.23 (m, 3H), 5.50 (s, 2H), 3.68 (ddq, *J* = 32.0, 9.4, 7.1 Hz, 8H), 1.29 (t, *J* = 7.1 Hz, 13H). ^{13}C NMR (75 MHz, Methylene Chloride-d_2) δ 163.63, 151.83 (d, *J* = 21.7 Hz), 140.50, 139.69, 137.05, 129.75, 122.98, 119.26, 119.24, 115.99, 104.03, 62.15, 54.12, 53.76, 53.40, 53.04, 52.68, 14.97.

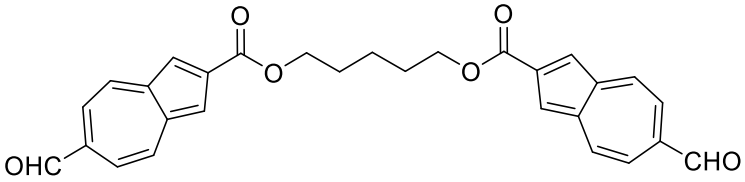

5-(6-formylazulene-2-carbonyloxy)pentyl 6-formylazulene-2-carboxylate (**25**) – Compound **23** (0.550 g, 0.0009 mol) was dissolved in 40 mL DCM in a 250 mL flask equipped with a stir bar. 20 mL of a 2M aqueous HCl solution was added and the reaction proceeded for two days. Upon completion the layers were separated, the organic layer was dried over $MgSO_4$, and the solvent was removed in vacuo. The crude material was recrystallized from hexanes to give 0.337g of **25** as blue green crystals in an 81%

yield. ^{1}H NMR (300 MHz, Chloroform-*d*) δ 10.10 (s, 1H), 8.57 – 8.48 (m, 2H), 7.86 (s, 2H), 7.73 – 7.64 (m, 2H), 4.48 (t, *J* = 6.4 Hz, 2H), 1.97 (p, *J* = 6.7 Hz, 2H), 1.82 – 1.66 (m, 1H).

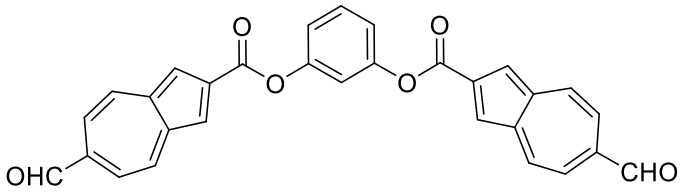

3-(6-formylazulene-2-carbonyloxy)phenyl 6-formylazulene-2-carboxylate (**26**) – Compound **24** (0.103 g, 0.00017 mol) was dissolved in 7 mL of DCM and transferred to a 25 mL flask with a stir bar. 3.5 mL of 2M HCL was added to the solution and stirred at room temperature overnight. Concentrated Na_2CO_3 was then added to neutralize the solution and the DCM was evaporated. The solids were then filtered off, washed with water, and sonicated in acetone to give 0.030 g of **26** as a green solid in a 39% yield. ^{1}H NMR (300 MHz, Methylene Chloride-d_2) δ 10.16 (s, 2H), 8.82 – 8.67 (m, 4H), 8.08 (s, 4H), 7.82 (d, *J* = 10.1 Hz, 4H), 7.61 (dd, *J* = 8.6, 7.8 Hz, 1H), 7.42 – 7.24 (m, 3H).

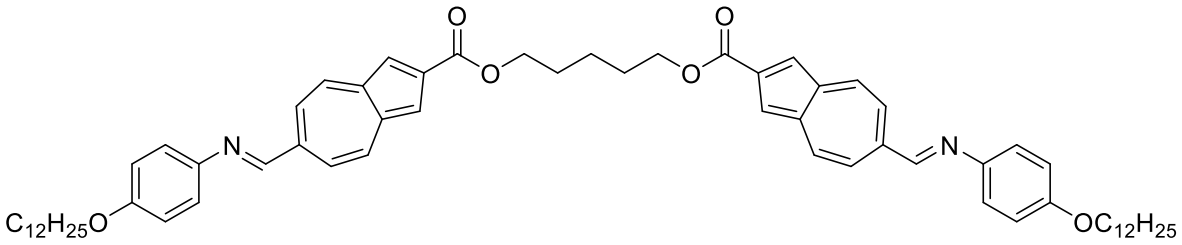

5-{6-[(E)-{[4-(dodecyloxy)phenyl]imino}methyl]azulene-2-carbonyloxy}pentyl-6-[(E)-{[4-(dodecyloxy)phenyl]imino}methyl]azulene-2-carboxylate (**27**) **W1014** – Compound **25** (0.107 g, 0.0002 mol) was massed into a 25 mL flask with bar and reflux condenser. 10 mL 200 proof ethanol was added along with 4-dodecyloxyaniline (0.253 g, 0.0008 mol) and one drop glacial acetic acid. The reaction was refluxed overnight. Upon completion, the reaction was cooled in the freezer, filtered, and the solids washed with cold ethanol. The crude material was recrystallized from DCM to give 0.189 g of **W1014** as

a green powder in a 84% yield. This compound was too insoluble to obtain a usable ^{1}H and ^{13}C NMR. HRMS $[M-H]^{+}$ -1.3 ppm off at 987.6251.

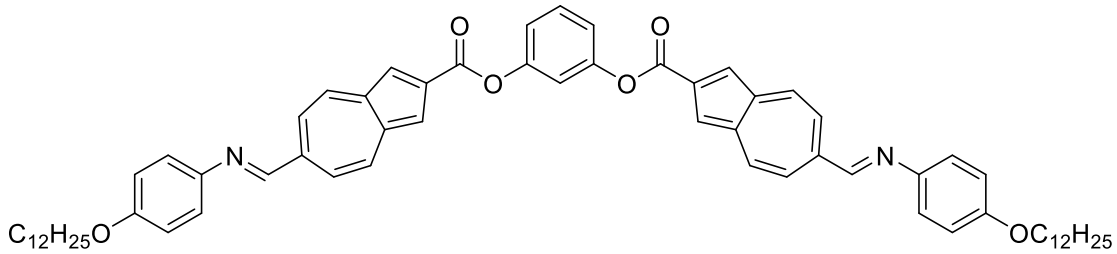

3-{6-[(E)-{[4-(dodecyloxy)phenyl]imino}methyl]azulene-2-carbonyloxy}phenyl-6-[(E)-{[4-(dodecyloxy)phenyl]imino}methyl]azulene-2-carboxylate (**28**) **W1015** – Compound **26** (0.021 g, 0.00004 mol) and 4-dodecyoxy aniline (0.029 g, 0.00009 mol) were massed into a 10 mL pear flask with a stir bar. 5 mL 200 proof ethanol was added along with one drop of glacial acetic acid and the solution brought to reflux for three days. After completion of the reaction, the mixture was cooled in the freezer, filtered, and the solids were washed with cold ethanol. The crude solid was recrystallized from toluene and DCM to give 0.016 g of compound **W1015** as a green solid in a 38% yield. This compound was too insoluble to get proton or carbon NMRs. HRMS $[M-H]^{+}$ -2.9 ppm off at 993.5782.

3 HNF Surface Functionalization

3.1 Introduction

The titled project developed from the desire to create a system to functionalize the filament surface for a variety of applications, as well as potentially understand the liquid crystalline dynamics of the HNF phase. Since it is known that modifications of the HNF structure, especially in the core, generally result in the destruction of the phase, we wanted to be able to functionalize the filament surface after it had been formed. This post-crystallization functionalization could be applied in the development of a variety of functional systems since it makes the surface of the filaments available for functionalization with a range of different molecules. By utilizing the HNF morphology as a physical scaffold to provide support for functional molecules, the other characteristics that make the HNF phase desirable for nanoscale device applications (alignment, porosity, nanoscale structure, etc.) could instead be targeted in a device. Additionally, the use of the HNF surface as a platform to attach small molecules, would create a network of filaments with applications dictated by the functionality of the added molecules ranging from chiral separations to circularly polarized luminescence.[41]

The focus of the project centered on developing a system that would attach molecules to the HNF surface. Since half of the surface area of the filaments is constructed of alkyl tails, it was reasoned that by placing a reactive functional group at the end of the tail, chemistry could be accomplished at the surface of the filament after the crystallization had occurred. The functional groups would be held in a glassy/crystalline environment and would heavily populate the aliphatic portion of the filament surface which may affect the types of reactions available for this type of transformation. Modification of self-assembled monolayers (SAMs) on silica substrates has been reported before, and serves as a model system for developing the conditions needed to modify the filament surface, given the molecules of the SAM are held in a similar fashion to the tails on the filament surface (**Figure 3.1**).[42] The appropriate

reactions conditions to modify the SAMs were reported to require reactions that have high reaction yield, functional group tolerance, and no need for catalysts.[42] Certain of these criteria coincide with the requirements for a reaction to be considered a "click" reaction, and this family of reactions served as a pool of qualified reactions to choose from for the purposes of modifying the SAMs.[43] Following suit, we chose to utilize click-type chemistry as well and specifically focused on the 1,3-Dipolar Huisgen cycloaddition reaction (though not technically a click reaction) as the appropriate reaction platform for our system.

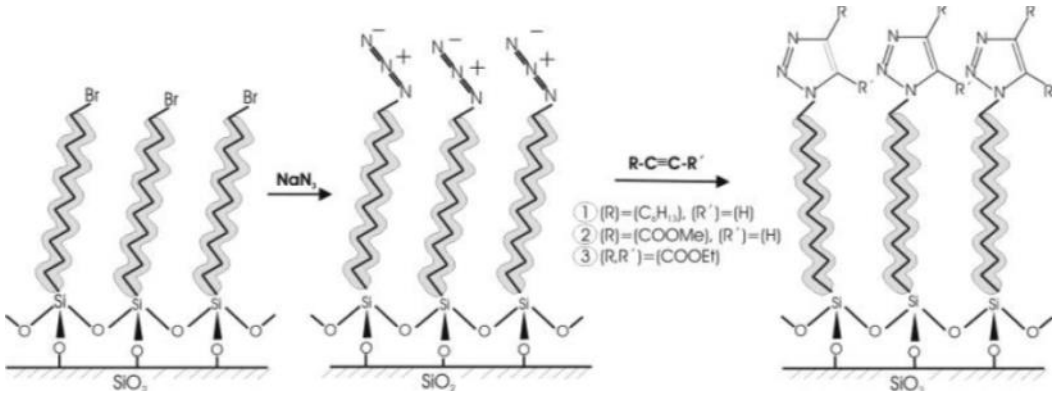

Figure 3.1 – An illustration of the densly packed nature of SAMs on a silica substrate. Many conventional chemical transformations are not suitable to be carried out under these conditions, however click type reactions show promise form these purposes.[43]

3.1.1 Huisgen 1,3-Dipolar Cycloaddition Reaction

From the development of "click" chemistry and the push for "greener" synthetic methods, the Huisgen cycloaddition reaction of 1,3-dipoles with dipolarophiles has recently received mounting interest. The reaction proceeds as a thermally allowed cycloaddition reaction between a variety of 1,3-dipoles (such as azides, nitrile oxides, ozone, and diazoalkanes), with dipolarophiles (such as alkenes, alkynes, and their heteroatom containing equivalents)(**Figure 3.2**).[44]

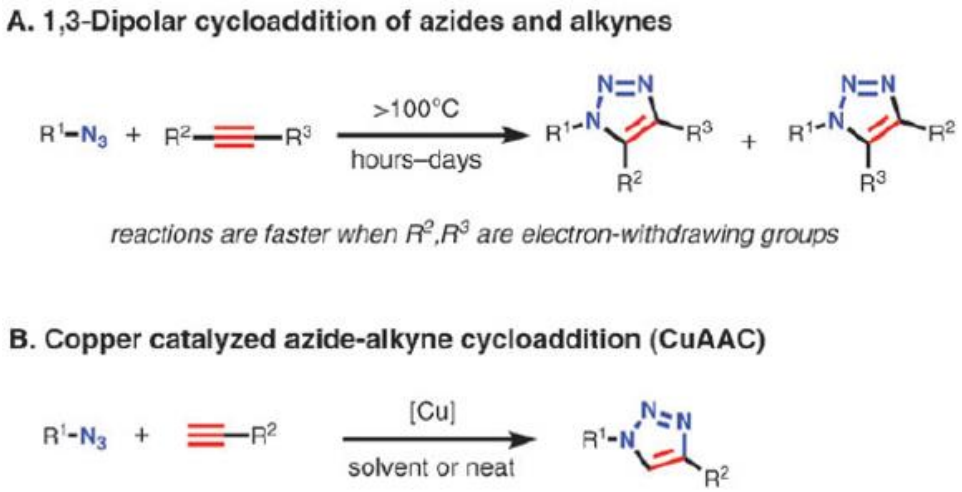

Figure 3.2 – (a) The Huisgen reaction between an azide and an alkyne is shown to give 1,4 and 1,5-disubstituted triazole rings at elevated tempuratures and long reaction times. (b) The copper catalyzed varient of the Husgen reaction between azides and alkynes gives solely the 1,4-disubstitution product and proceeds under mild conditions and in the presence of water.[45]

The reaction results in the formation of a new five membered ring whose construct is dependent on the dipole and dipolarophile used. The reaction specifically between alkynes and azides has been the subject of recent focus because azides are easily installed synthetically, are stable to a variety of reaction conditions thus lowering the need for the use of protecting groups, and possess considerable energy density making them amenable to mild reaction conditions.[43] As with all pericyclic cycloaddition reactions, this reaction is governed by the relative energies of the frontier molecular orbitals of the reactants and is dictated by the electronics of both species. For example, electron withdrawing groups on the alkyne promote the interaction of the alkyne LUMO with the azide HOMO as the relative energy levels of the two orbitals are more closely matched.[44] As a result, the reaction rate can vary in length from hours to days at elevated temperatures depending on the relative orbital energetics. In the case of asymmetric alkynes, regioselectivity is not maintained with both isomers forming in nearly equal amounts, which can be undesirable for certain synthetic applications. However, the copper (I) catalyzed version of the Huisgen reaction between alkynes and azides (CuAAC) proceeds

readily at room temperature, in the presence of oxygen and water, often within a few hours, and the reaction is robustly regioselective giving predominantly the 1,4 regioisomer.[43]

Huisgen 1,3-Dipolar reaction for Surface Functionalization

To complete the reaction at the filament surface, the reaction conditions should be kept as simple as possible, minimizing purification steps which may not be compatible with keeping the filament structure intact. Ideally, the constituent functional groups will react under ambient conditions without the need for a catalyst and led to utilization of the Huisgen reaction for our system as opposed to the CuAAC reaction. Here, the regioselectivity of the reaction is not important since we simply want the functionality to be attached to the filament surface in any orientation. Next, we needed to figure out how to promote the bond formation at room temperature for a reaction that commonly proceeds at elevated temperatures. Since the reaction is governed by the energetics of the frontier molecular orbitals, manipulation of these orbitals can help to minimize their difference in energy, allowing for the reaction to proceed at room temperature. This is carried out most easily by modifying the acetylene portion of the reaction leading to our utilization of the activated acetylene, diethyl acetylene dicarboxylate (DEAD), as the ideal compound for reaction with filaments that are decorated with the requisite azide functionality. Though DEAD was used to probe suitable reaction conditions, there is no apparent reason that other activated acetylenes could not be designed and synthesized to react under similar conditions.

Another hurdle that had to be addressed in the planning stages of the development of this system was this issue of running the reaction neat versus in solution. An issue with attempting the reaction neat is making a mixture of the HNF forming material and the Huisgen reaction counterpart without the two reacting prematurely. Traditionally, mixtures of BLC molecules and other materials are formed by melting the respective materials and physically blending them in the melt. Since the clearing points of BLC compounds are commonly above 150 °C and can extend well above 200 °C, this route

becomes impossible due to the thermal instability of azides and their violent decomposition upon heating. Further, the reaction is thermally allowed so heating the two materials in the presence of one another would result in some degree of reaction prior to HNF formation. To work around this issue, we decided that utilizing the gelating behavior of HNF forming materials would be beneficial. A reaction in the gel phase would maintain the filament structure, and retain aspects of solution phase chemistry by allowing a functional molecule to be dissolved into the gel solvent which could then diffuse through the gel network and interact with the filament surface.

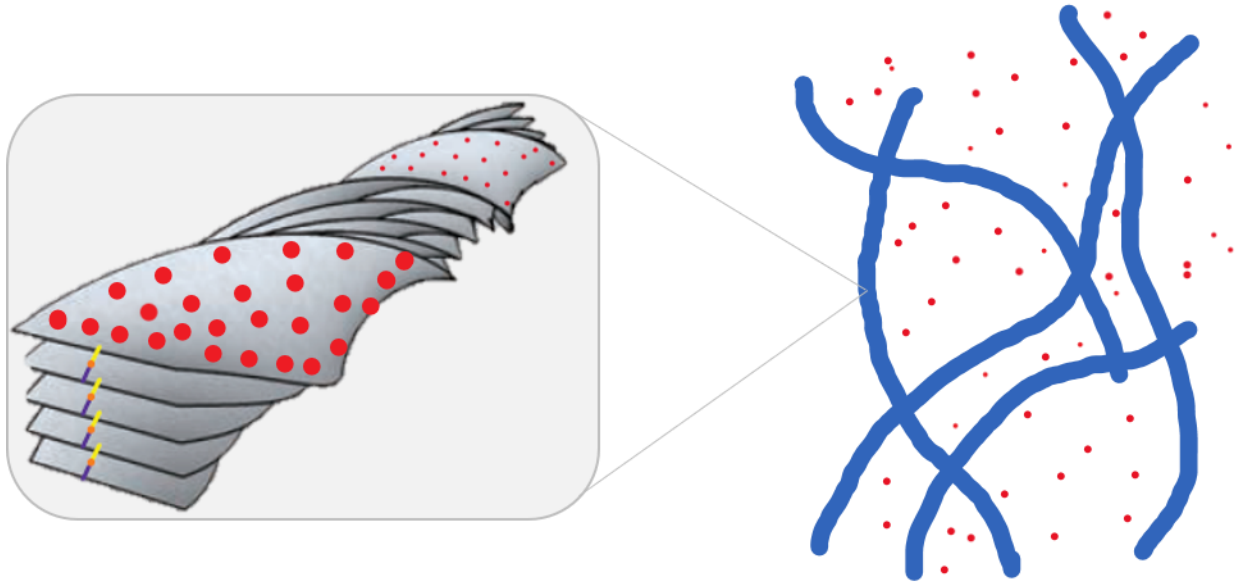

Figure 3.3 – The gel network of HNF froming BLCs is constructed of long helical filaments (blue) surrounded by solvent and reactive molecules (red). By having functional groups at the surface of the filaments, the reactive molecules, dissolved in the solvent that surrounds the gel network, can diffuse to the HNF surface as they would in a normal solution based reaction, allowing for reactions to occur at the filament surface.

3.1.2 Low Molecular Weight Organogelators

Traditional gelating materials are constructed by crosslinked polymer networks and can be categorized by the type of crosslinker present within the system. Chemical gels are constructed by covalently bound polymer chains within which a multifunctional crosslinking agent has been mixed in with the monomer to provide the branching needed to form the gel network.[45] Conversely, physical

gels are made up of crosslinks formed through electrostatic interactions and involve the presence of multi-coordinate ions to provide the junctions between polymer chains (**Figure 3.4**).[45] For both systems, the crosslinks are considered to be permanent, or at the least time invariant, and provide the platform by which traditional viscoelastic behavior is bypassed, producing a system that can support its own weight for sufficiently long length scales (the traditional qualitative test for gel formation).[45]

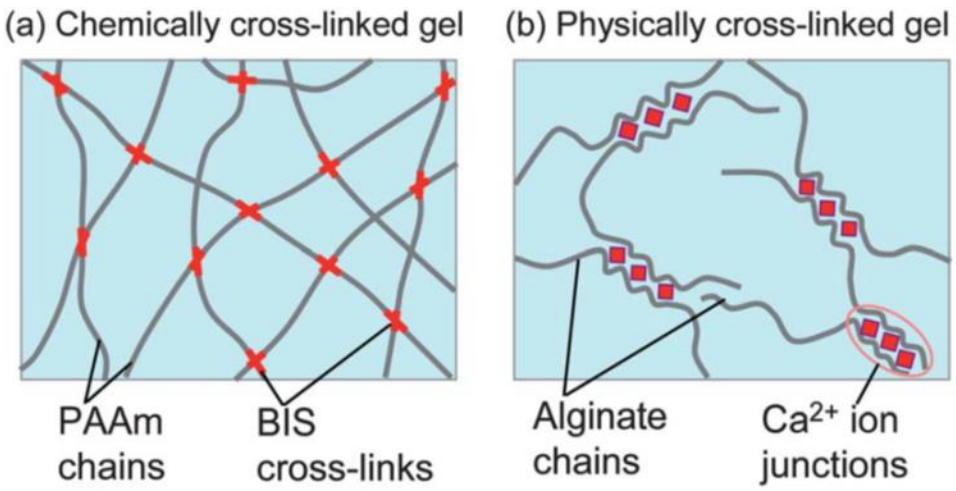

Figure 3.4 – (a) An illistration representing the chemically cross-linked gel network of polymers. The red junction zones are covalent linkages between neighboring ploymer chaines. (b) Another illustration that represents plymeric gels composed of physical cross-links. The red squares indicate multi-coordinate ions (Ca^{2+}) that holding the neighboring polymer (alginate) chains together to form the gel network.[46]

From this it seems that gel formation from nonpolymeric small molecule systems should not be possible as there are seemingly no junction zones between the molecules to provide the rigidity needed to form the gel network. However, many such systems are known, and are formed as the result of the self-assembly of small molecules from an isotropic solution into highly anisotropic filamentous structures.[45] For the gel to form, the low molecular weight organogelators (LMOGs) are dissolved in a chosen solvent at high temperatures to produce a sol and then allowed to cool forming the gel network as the molecules aggregate and come out of solution. However, it is not sufficient to have only filaments or chains present in the system for a gel to form and this is apparent knowing that non-crosslinked polymers commonly give traditional viscoelastic solutions.[45] For these self-assembled structures to

form gels, the filaments need to be significantly longer than polymer chains and should extend for microns in length.[45] Additionally, the filaments need to be fairly stiff, to give rigidity to the network and allow for the storage of strain energy. Finally, the filaments should interact in such a way that they do not simply glide past or around one another which is achieved by: attractive forces between the filaments, areas where the filaments become entangled, or sites where the filament terminus is lodged into another filament chain (**Figure 3.5**).[45] Finally, these criteria can result in the formation of a gel provided that the filament structure formed by the small molecules is sufficiently long-lived and not subject to constant breaking/reforming events. Due to the nature of the HNF phase, gelation is typically looked for in the characterization process of bent-core liquid crystals (BLCs). Materials that possess the HNF phase are good organogelators and this characteristic has served as a means to differentiate the HNF phase and the closely related low temperature DC phase.[38]

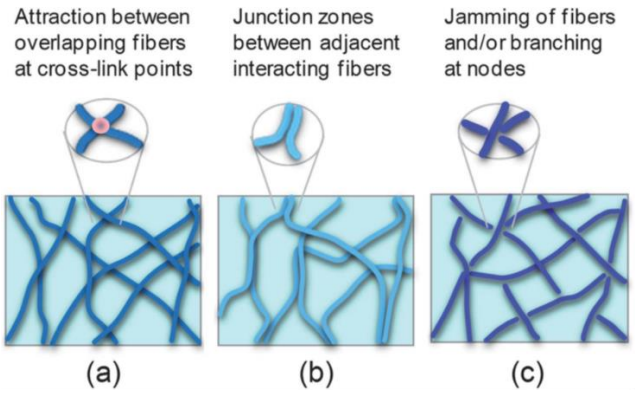

Figure 3.5 – The different types of interactions that may be present in gels constructed by LMOGs. (a) attractive overlapping cross-links between neighboring filaments, (b) Entaglement zones of the filaments, and (c) areas where the filament ends become jammed or lodged.[46]

3.1.2.1 Gelation in the HNF phase

Gelation has been observed for homologues of the P-n-OPIMB series of compounds, the dimeric twin compounds reported by Gorecka, and in the asymmetric compounds reported by Tsai, all of which were confirmed to form HNFs as the bulk phase.[10,38,39,46] Blends of P-9-OPIMB with hexadecane and octanol resulted in the formation of stable gels after the materials were dissolved in the solvents at high

temperatures and allowed to cool.[10] The gelated samples of P-9-OPIMB in the hexadecane contained 98% by weight hexadecane indicating the strong gelation ability of the BLC material. Using freeze fracture transmission electron microscopy (FFTEM), images were taken of the free surface of the gel and it was observed that the gel network was constructed of a dense intertwined system of helical filaments (**Figure 3.6**).[10] In the octanol solution, individual filaments are apparent although interestingly the degree of layering seems to be different from the bulk HNF samples.[7,10]

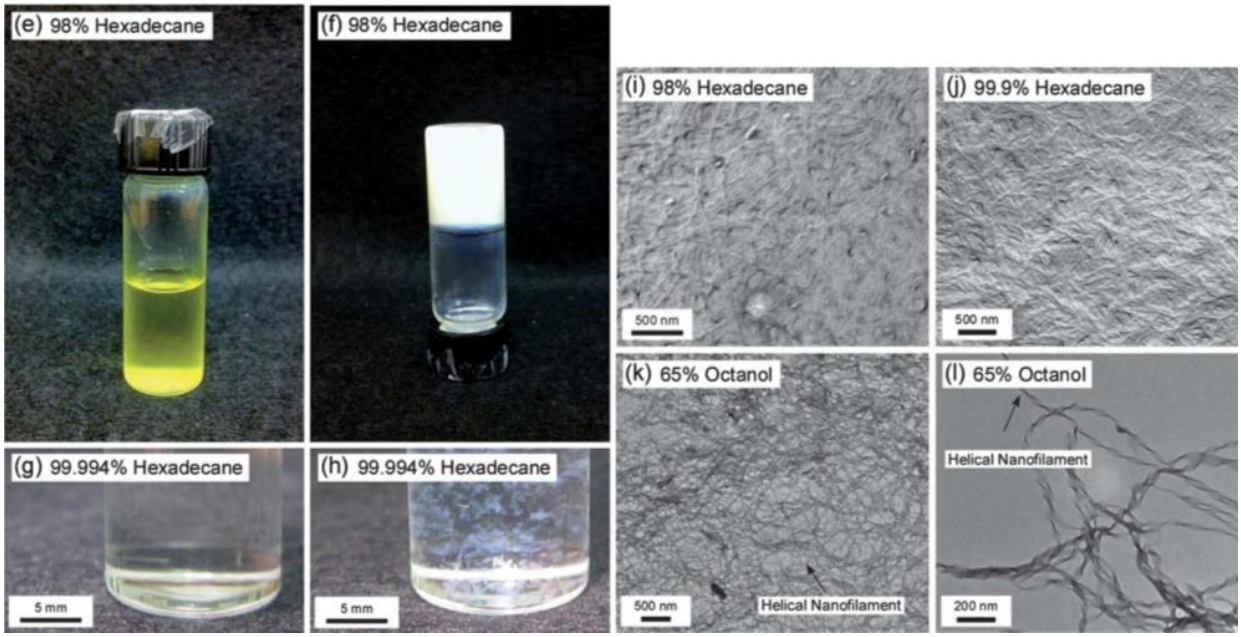

Figure 3.6 – Images of the gelating behavior of P-9-OPIMB in hexadecane and octanol. (e) shows the sol state of the material in hexadecane, (f) an image of the resulting gel upon cooling of the sol, (g,h) the behavior of the material at extremely dilute concentrations, (i-l) FFTEM images of the gel network after evaporation of the solvent clearly showing the presence of helical filaments.[12]

The dimeric biphenyl twin series of compounds show strong gelating ability for a variety of organic solvents including toluene, nitrobenzene, (R)-(+)-methylcylcohexanone, (+)-menthone, and (-)-menthone.[38] X-ray diffraction experiments on the gels reveal the crystalline nature of the filaments that make up the gel network for these molecules. Scanning electron micrographs (SEM) show the same general gel network construction as the gels formed for the P-9-OPIMB gels although the filaments take on a slightly different helical structure. For the biphenyl twins, the filaments are helical tubules as

opposed to helices made up of negative gaussian curvature.[38] This could indicate a that there is a difference in the growth of the filaments from solution for the two types of compounds. Different compounds constructed of the same biphenyl arms, but this time with a rigid aromatic core, were also reported to form the HNF phase and function as good organogelators with interesting gel morphology. In gels formed from these materials, filaments constructed of mono and bi-layers were observed in coexistence with filaments made up of the more traditional five to eight layer construction (**Figure 3.7**).[46] This phenomenon is unprecedented and not has not been reported for bulk samples of HNFs.

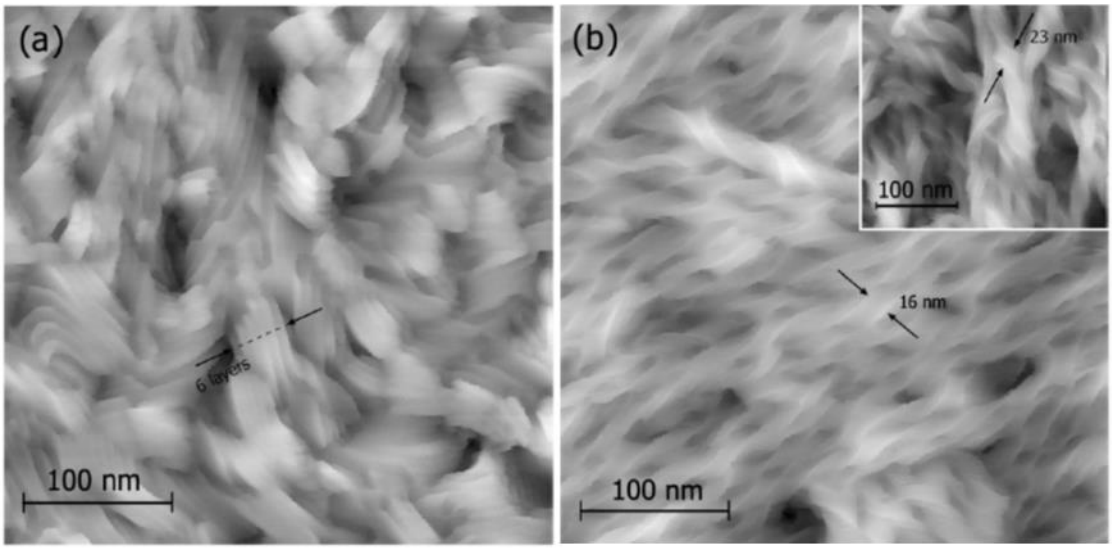

Figure 3.7 – AFM images of the gel networks of the HNF forming biphenyl materials. (a) shows the traditional layering and layer curvature of the helical filaments. (b) shows areas of filaments constructed of single and double layers.[47]

3.2 Approach

To functionalize the HNF surface, a reactive functional group (alkyne/azide) must be available at the surface in order to covalently link a functional molecule. Since the HNF surface area is made up of aromatic layer edges and aliphatic layer ends, attaching an appropriately selected functional group to the tail of a known HNF forming compound will result in exposure of that functional group at the HNF

surface. By utilizing the strong gelating nature of all HNF forming compounds, conducting the reaction in the gel phase will allow for the functional group to be exposed to solvent while remaining immobilized on the filament surface. This simultaneously retains aspects of solution phase chemistry in that the reaction is still taking place in a solvent environment, while also maintaining the desired filament structure. To investigate these conditions, two materials, W899 and W900, were designed and synthesized with the azide and alkyne termini respectively (**Figure 3.8**).

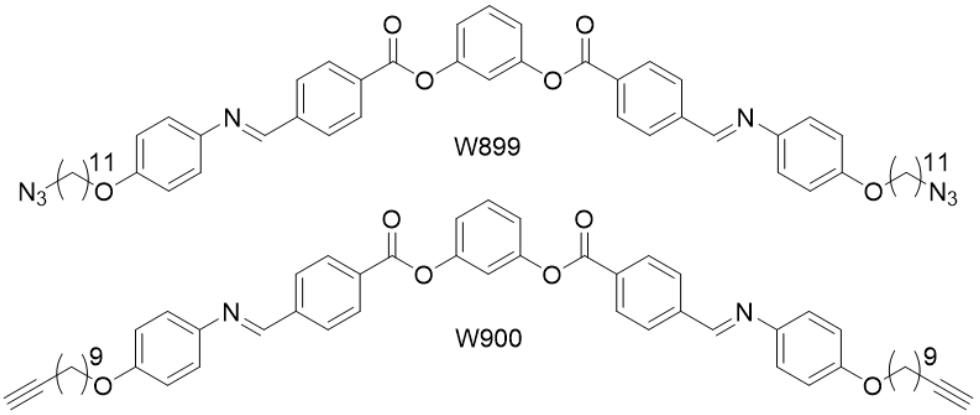

Figure 3.8 – Molecular structure of the synthesized compounds W899 with the azide terminated tail, and W900 with the alkyne terminated tail..

3.3 Experimental Set-Up

3.3.1 W899

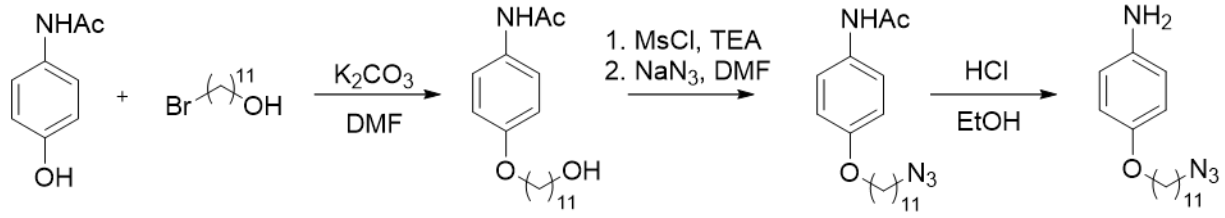

Figure 3.9 – Reaction scheme for synthesis of the azide terminated tail.

Synthesis of the azide tail was carried out by first reaction of 4-acetamidophenol with 11-bromo-1-undecanol under Williamson conditions to give

N-{4-[(10-bromodecyl)oxy]phenyl}acetamide as the intermediate with which to establish the azide functionality (**Figure 3.9**). Several conditions were then screened to exchange the alcohol for the azide group including using phosphoryl azide under Mitsunobu conditions, but were unsuccessful. The most successful route was the two-step process of, first, mesylating the terminal alcohol to activate it towards the S_N2 attack of the azide anion in the second step. This resulted in an much simpler purification of the azide and the final deprotection of the acetamide protecting group gave the final intermediate, 4-[(10-azidodecyl)oxy]aniline, ready for the condensation with the di-aldehyde core. The final condensation reaction was carried out in absolute ethanol with catalytic acetic acid to give W899 which was then purified by multiple recrystallizations in toluene to give the pure product.

Characterization

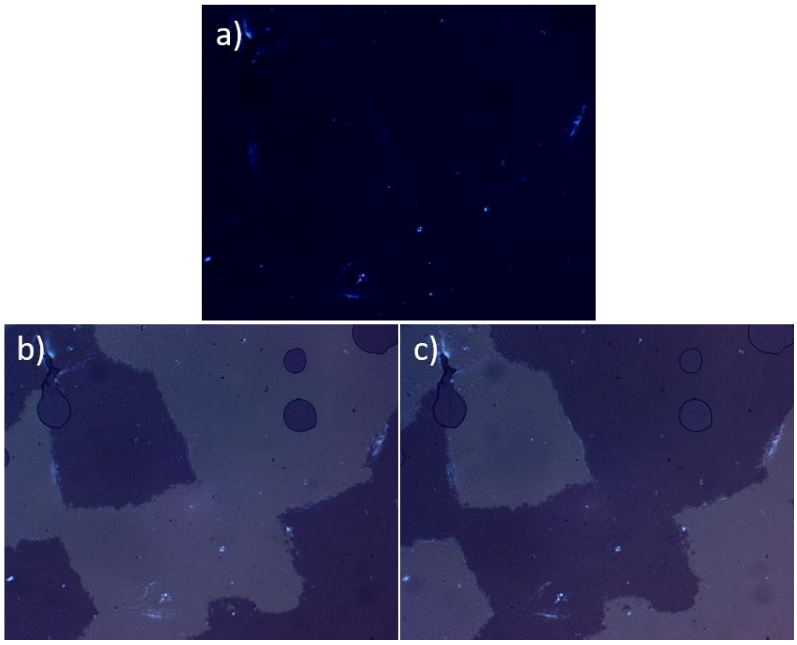

Figure 3.10 – POM images of W899 in a glass planchette taken at 100 °C. (a) The characteristic dark blue coloring of the HNF phase under crossed polarizers. (b,c) When the polarizers are decrossed in opposite directions, chiral domains are obserrved for the sample that interchange depending on the sign of decrossing.

Differential scanning calorimetry (DSC) experiments showed the formation of a single phase followed by a glass transition upon cooling from the isotropic. Polarized optical micrographs (POM) of

the material cooled from the isotropic in a 4 μm planar aligned cell showed the formation of a low birefringent, dark blue texture between crossed polarizers. Upon decrossing the polarizers in either direction, very clear domains of strong circular birefringence were apparent and interchanged depending on the sign of the decrossing (**Figure 3.10**). This indicates the formation of large chiral domains and is evidence for the formation of HNFs but must also be confirmed by FFTEM.

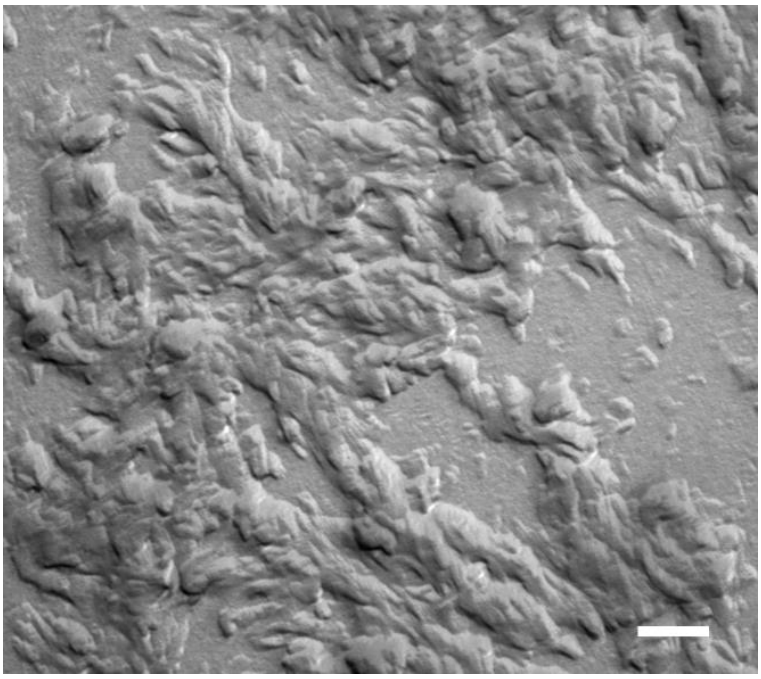

Figure 3.11 – FFTEM micrograph of W899 showing areas of saddle deformed layers truncated filametns. The filament structure isn't as well developed as it is for other materials, but the structures observed are still indicative of HNF formation. The scale bar represents 200 nm.

FFTEM images of the material did not seem to show clearly formed, well defined filaments, but more truncated filament type structures that possessed saddle deformed layers (**Figure 3.11**). There were areas in the field of view that showed flame tip and bamboo type structures that have been observed for HNF forming materials forming near a glass substrate.[47] These helped to confirm the formation of the HNF phase. The poorly formed filament morphology has been seen in other HNF forming materials (e.g. the asymmetric biphenyl compounds reported by Tsai) and in these cases, blends with rod shaped LC compounds may be beneficial as they dilute the system and allow for the full

realization of the phase's nanostructure.[39] Experiments of this type were determined to be unnecessary as the structures seen in the FFTEM micrographs resembled the previously reported structures of HNF forming materials and the phase was confidently assigned as being the HNF phase.

3.3.1.1 Gelation

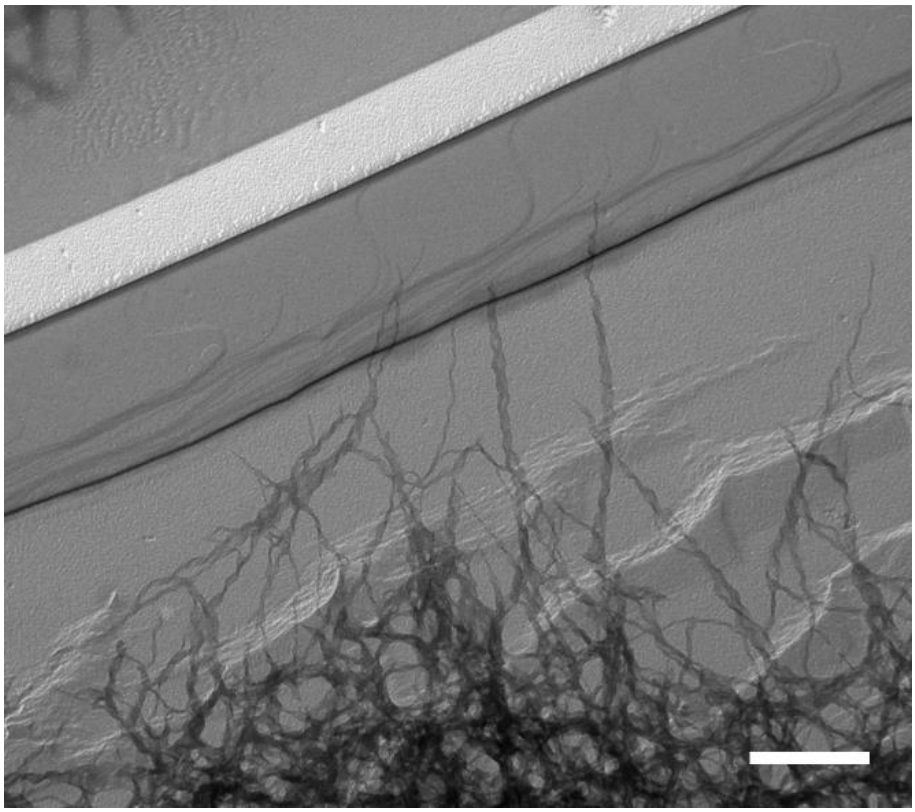

Figure 3.12 – FFTEM micrograph of the gel network formed from W899 in dodecane after evaporation of the solvent. Residual gel material can be observed and is seen to be made up of helical filaments with varying degrees of layering. The scale bar represents 500 nm.

Several solvents, including toluene, dichloromethane, cyclohexane, dodecane, DMSO, and ethanol were investigated for gelation behavior and interestingly it was found that only dodecane gave a gel (**Figure 3.12**). W899 was soluble in toluene and recrystallized from cyclohexane,dichloromethane and DMSO, while being only sparingly soluble in ethanol even at elevated temperatures. FFTEM of the gel after evaporation of the dodecane solvent revealed a network constructed of helical filaments, with

the filament size varying from several to single layers as was observed for the biphenyl dimers mentioned earlier.[46]

3.3.2 W900

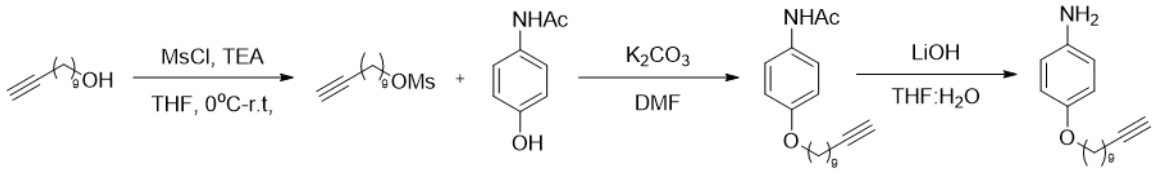

Figure 3.13 – Reaction scheme for the alkyne terminated tail.

Synthesis of the alkyne terminated tail was achieved by first activating the alcohol of 10-undecyn-1-ol with mesyl chloride followed by reaction with 4-acetamidophenol under Williamson ether conditions to give N-[4-(undec-10-yn-1-yloxy)phenyl]acetamide (**Figure 3.13**). Deprotection of the amide was then carried out with a solution of lithium hydroxide in THF:H_2O to give 4-(undec-10-yn-1-yloxy)aniline which was then reacted with the di-aldehyde core in the presence of ethanol and catalytic acetic acid at reflux to give W900.

Characterization

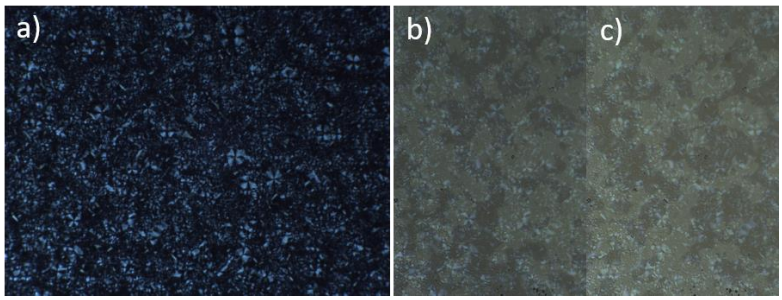

Figure 3.14 – POM micrographs of W900 in a glass planchette. (a) shows the formation of the characteristic low birefringent texture with blue color of the HNF phase upon cooling from the higher temperature B2 phase (not shown). (b,c) show the presence of chiral domains upon decrossing the plarizers in both directions.

DSC measurements of this compound revealed the formation of two phases upon cooling from the isotropic. When observed in a glass cell in the POM it was evident that the higher temperature

phase was one of the B2 phases as birefringent the focal conics and curving ribbon like domains quickly grew in from the isotropic. Upon further cooling, the birefringence dropped significantly giving way to a dark blue color and grainy domains. Upon uncrossing the polarizers, chiral domains were apparent as the oppositely handed areas interchanged depending on the sign of decrossing (**Figure 3.14**).

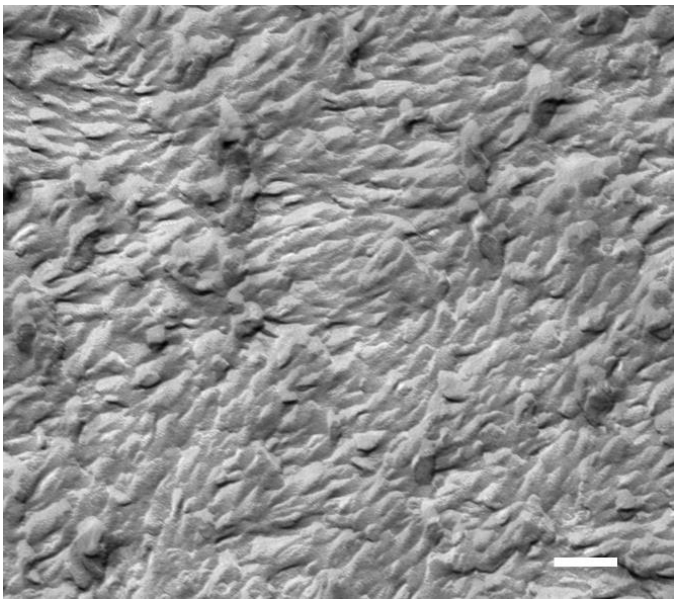

Figure 3.15 – FFTEM micrograph of W900 showing the traditional HNF morphology with areas of coherent twist and individual filaments. The scale bar represents 200 nm.

FFTEM images of the neat material clearly showed the formation of HNFs in the bulk and confirmed the phase assignment (**Figure 3.15**).

Gelation

Gelating conditions were investigated for a variety of solvents including, toluene, dichloromethane, ethanol, acetonitrile, DMSO, dodecane, decyl alcohol, 1-butanol. W900 appears to be a much stronger organogelator than W899 as gels were formed in all of these solvents except for ethanol. Interestingly the physical appearance of the gels depended on the polarity of the solvent used. In dodecane, an opaque, somewhat iridescent, white gel was formed upon cooling from the clear yellow sol. However, DMSO gave a more translucent yellow gel upon cooling from a similar yellow sol. FFTEM

images revealed that these two gels had drastically different nanoscale structures. The gel formed from dodecane gave nicely formed helical filaments as expected from an HNF forming material (**Figure 3.16**). Images from the gel formed in DMSO revealed a planar structure permeated by areas of solvent. This behavior is interesting as the traditional gel construction of an LMOG being comprised of semi-rigid filament structures was not observed. It is not clear how the gel is forming from this planar structure. Additionally, the change in structure and the difference in color of the two gels indicates a different arrangement of the molecules resulting in a bathochromic shift of the absorbance form the gel formed in DMSO. Due to this variation in gel structure and the activity of the DEAD towards the cycloaddition reaction, the gel phase reactions focused on using W899 as the gelator.

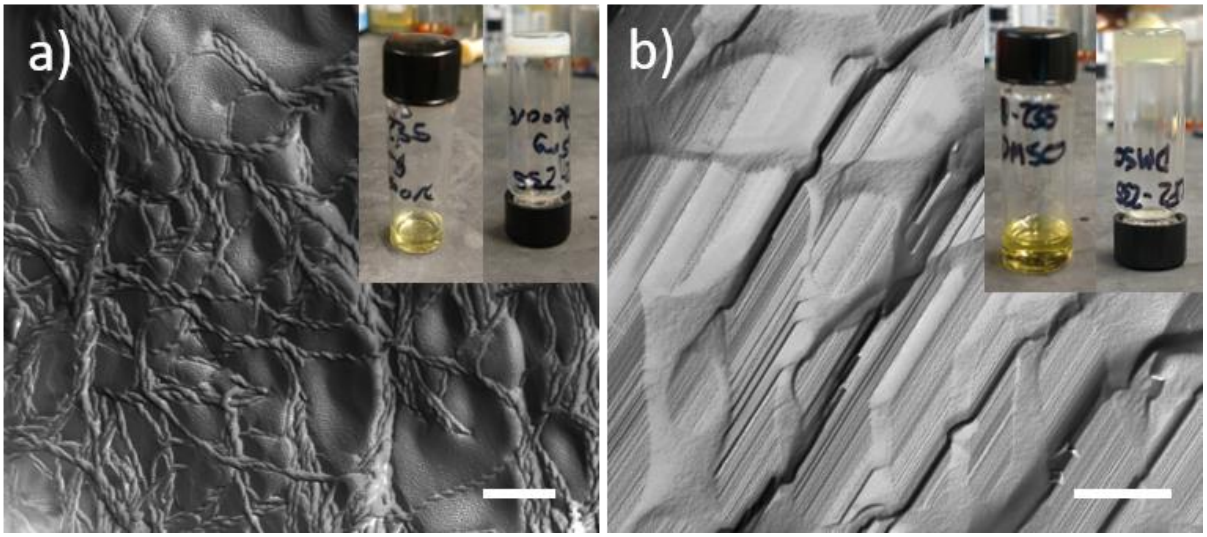

Figure 3.16 – FFTEM micrographs of the gel networks of W900 in dodecane (a) and DMSO (b). The inset images show the difference in the gel appearance for both systems. The gel in (a) is opaque and white, while the gel formed in (b) is much more translucent and yellow in color.

3.3.3 Gel Phase Reaction

The gel phase reactions were carried out using 1/2-dram glass vials with screw on caps. Approximately 5 mg of W899 was massed into a vial and dodecane was added via syringe with the concentration for all gelated samples being kept at 1 mg/100 µL. The cap was then screwed on tightly

and the vial heated carefully with a heat gun until W899 had dissolved completely giving a clear yellow sol. After the material was completely dissolved, the solution was cooled to room temperature and the samples were allowed to sit undisturbed for at least 30 minutes to ensure complete thermal equilibrium with the surroundings. Once the gel was completely formed, a solution of the diethyl acetylene dicarboxylate (DEAD) in dodecane was made by massing 7-10 mg of DEAD into another 1/2-dram vial and dissolving in 100 µL of dodecane. The solution was then taken up in a syringe and carefully deposited on the top of the gel surface, the system capped, and then covered to prevent light from entering (**Figure 3.17**). To test how quickly the DEAD solution would diffuse through the gel network, a solution of dodecane and an azulene dye was formed and deposited on top if a gel in the same manner as the reaction. The azulene solution had completely diffused through the entire gel in two hours, suggesting that the DEAD would have diffused through the sample in a similar amount of time (**Figure 3.17c**).

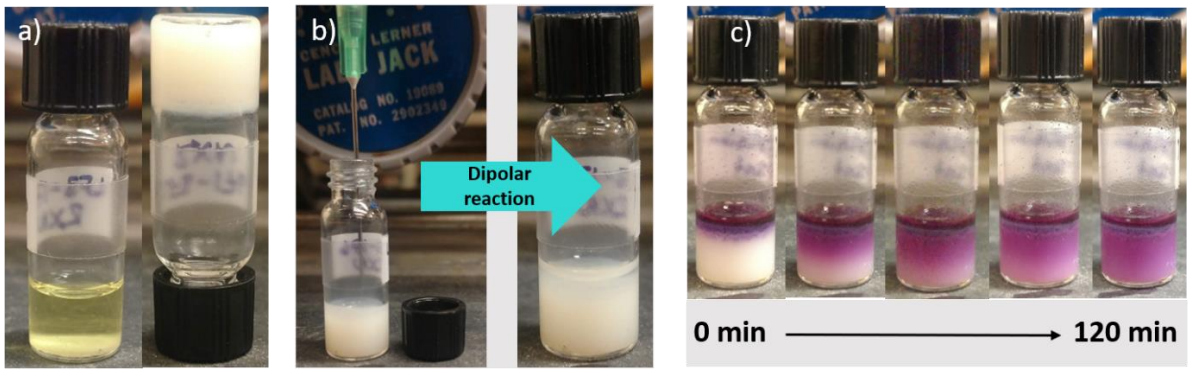

Figure 3.17 – Reaction set-up for the gel phase reaction of W899 with DEAD. (a) The left image is a picture of the sol fromed by heating W899 in dodecane, while the right image shows the formation of the gel after cooling to room temperature. (b) The reaction is initiated by carefully depositing the DEAD/dodecane solution to the gel surface via syringe. The reaction is then placed in the dark and allowed to proceed undisturbed. (c) shows the diffusion time required for a dye to diffuse through the enitre gel network. Complete diffusion was observed after 120 minutes.

The reactions were allowed to proceed overnight after which removal of the DEAD and solvent was carried out in a vacuum oven. In the oven, the cap was loosened, and the atmosphere evacuated at room temperature overnight to remove any excess DEAD. After 24 hours under vacuum at room

temperature, the system was then heated to 80 °C overnight to remove the dodecane solvent leaving behind the gel residue.

Characterization

Characterization of the gel phase reactions was carried out using NMR and mass spectrometry to identify the constituent molecules in the gel network. For the NMR experiments, dichloromethane-d2 was added to the 1/2 dram vail containing the gel residue, and the residue was completely dissolved. ^{1}H NMR experiments clearly show the formation of new proton environments indicating that a reaction had occurred (**Figure 3.18**). Prior to the reaction, the intensity of the methylene peaks corresponding to the alkoxy and azido methylene environments are equivalent and give integral ratios of 1:1. After the reaction, the azido methylene peak decreases in intensity and a new peak corresponding to the methylene adjacent to the newly formed ring appears with intensity that is equal to the intensity lost from the azido peak. The change in intensity of the azido methylene peak gives the percentage of azide groups that were reacted and shows that the reaction reliably gives a yield of 35-40% even after allowed to react form ten days. ^{13}C NMR shows the formation of new aromatic carbon peaks, further confirming the formation of the triazole ring (see Appendix).

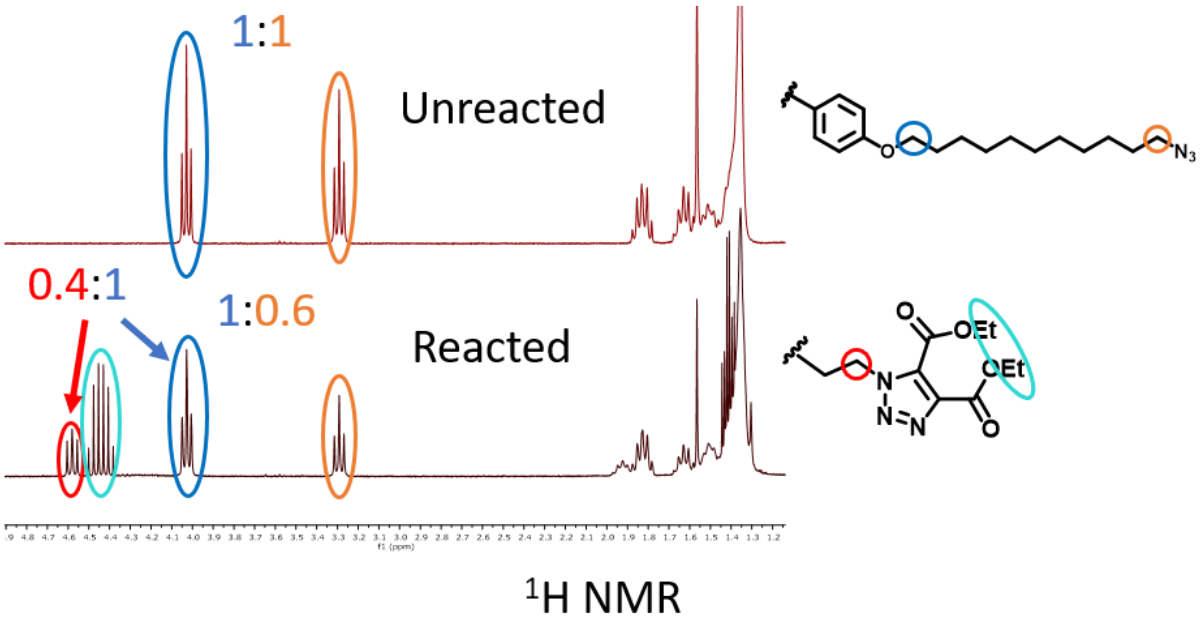

Figure 3.18 – Overlayed ^{1}H spectra of unreacted W899 and the gel residue after the DEAD and dodecane had been removed by evaporation. Only the aliphatic portion of the spectrum os shown. The azide methylene (orange) gives way to the formation of a new methylene peak (red) as the triazole ring is formed inidcating the reaction is occuring.

However, this data does not give information as to the structural nature of the reacted compounds. Mass spectrometry showed the presence of three separate compounds in the gel residue and the molecular ion peaks for the three compounds suggest those compounds are the unreacted, mono-reacted, and di-reacted products. DOSY NMR experiments were attempted to separate the compound structures by their diffusion coefficients in order to further confirm the identity of the three reaction products, however the materials limited solubility and similarity in molecular structure made the DOSY data difficult to interpret, although the spectrum seemed to corroborate the mass spectrometry data (see Appendix). FFTEM images of the gel network were obtained for the gel residue before and after the reaction in an attempt to visually see if there was a modification to the filament surface texture as an indication of reaction there. Unfortunately, the FFTEM images were inconclusive as areas of isolated filaments were not clearly observed (**Figure 3.19**). This may be remedied by allowing the solvent to evaporate naturally, perhaps under a stream of air, to prevent compaction of the gel

network. Additionally, it may be beneficial to simply try to image the gel network directly without first making the Pt/C replica.

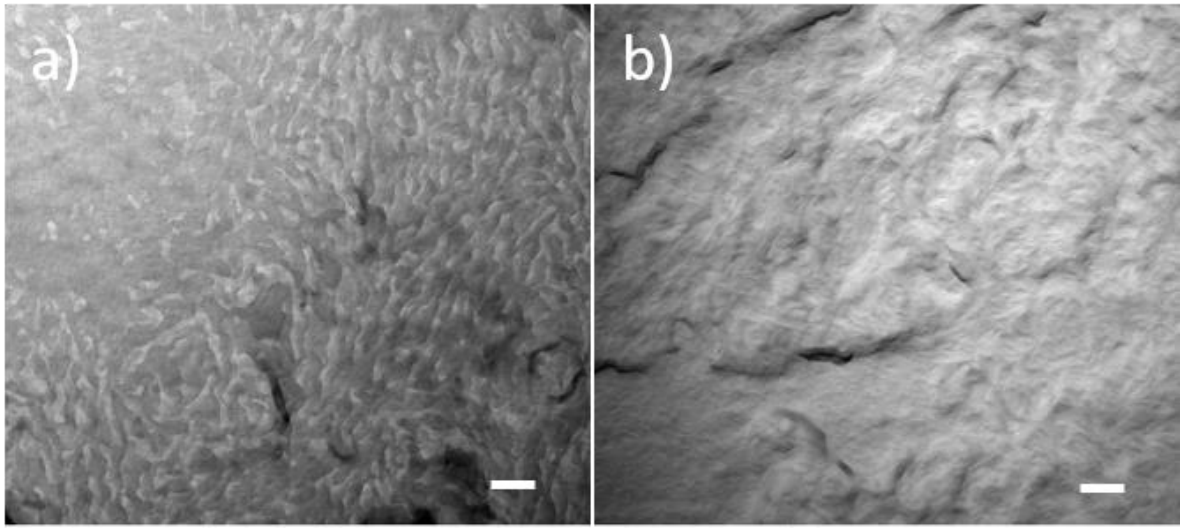

Figure 3.19 – FFTEM micrographs of the gel network residue after the evaporation of all liquid components for (a) the unreacted gel and (b) the gel after reaction. In both cases the surface of the filament network is not apparent. Issues with replica formation may have contributed to the lack of resolution within the images. Scale bars represent 500 nm.

3.4 Discussion

From the NMR experiments it is clear that the reaction is proceeding, but it isn't clear if the reaction is occurring at the filament surface or somewhere else, for example with any residually dissolved W899. Given that the filament surface is made up of crystalline layer edges and aliphatic layer ends, and W899 is symmetric with two azides available for reaction, only a fraction of the total azide population is expected to react. The number of reacted azides should decrease with filaments of increased layering and should obey the equation, $\left(\frac{1}{N}\right) \cdot \%\, yield$, where N represents the number of layers within a filament, since at any time only the layers at the surface of the filament will have half of their total azide population exposed to the solvent. In the bulk, the filaments are composed of five to six layers so the range for the reacted azides should range from 16.67% to 20% (assuming a 100% reaction yield) which is smaller than what is calculated from the integral ratios from the ^{1}H NMR. However, with

the report of HNF gel networks being constructed of mono- and bi-layer systems, and the observation that monolayer filaments are present in the gel from W899 in dodecane, the reaction yield would be larger than what would be expected form the neat case, and the observed 35-40% falls within a reasonable range for a gel network made up of filaments with varying number of layers. Additionally, without the presence of single layer filaments, the di-reacted product should theoretically not be possible assuming that 100% of the W899 molecules are accounted for in the filament network.

Figure 3.20 – A 0.002% by wieght solution of W899 in dodecane showing the formation of bundles of filaments after cooling to room temperature. This material appears to be only sparingly soluble at room temperature in dodecane.

To test the solubility of W899 in dodecane and see if a significant amount of material remains dissolved in the solvent at room temperature, a 0.002% by weight solution of W899 in dodecane was formed by dissolving the material in the hot solvent and then allowing it to cool. Even at this very dilute concentration, W899 appears to be completely insoluble and visually bundles of HNFs were observed to come out of solution even at this low concentration (**Figure 3.20**). This qualitatively suggests that the material is only sparingly soluble in dodecane at room temperature and is evidence for the di-reacted product forming as a result of the presence of mono-layer filaments.

3.5 Conclusions and Future Work

From these results it appears that the reaction is occurring at the filament surface. The invariance of the reaction yield, especially as a function of time, is evidence that the reaction effectively exhausts the available azide population. Additionally, unreacted W899 should be present as filaments made up of more than two layers will have azido groups buried within the filament structure inaccessible to the DEAD in the solvent. The presence of the doubly reacted product can be rationalized from the presence of mono-layer filaments in which all available azide groups would be present at the filament surface. However, direct evidence of the reaction at the filament surface is needed to prove where the reaction is taking place. FFTEM should help to clarify this issue but the sample conditions need to be modified to obtain clearer images. Careful evaporation of the gel solvent may help to prevent the network from collapsing and help provide a clearer image, and it may be beneficial to observe the gel directly in the microscope without the metallic replica to circumvent any issues with sample degradation from forming the replica.

The design and synthesis of coumarin derivatives with alkyne functionality were also considered and synthesized during the course of this project to serve as a fluorogenic probe that could be used as evidence for reaction success as well as imparting a degree of functionality to the gel network. The alkynyl-coumarins do not fluoresce on their own but become fluorescent upon formation of the triazole ring when reacted under Huisgen or CuAAC conditions.[48] Attachment to the filament surface would result in a fluorescent gel that could then be used in investigations of the dynamics of the HNFs both in solution and neat. Additionally, successful reactions of these types of compounds would serve as a platform for the design of new functional molecules showing that the activated alkyne is the only functionality needed for successful attachment to the azide decorate filament surface.

3.6 Synthesis

3.6.1 Total Synthesis of W899

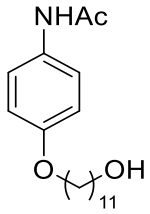

N-{4-[(11-hydroxyundecyl)oxy]phenyl}acetamide (**1**) **–** 4-acetamidophenol (9.07g, 0.060 mol) was massed into a 250 mL round bottomed flask equipped with a stir bar. DMF was added along with K_2CO_3 (9.82 g, 0.071 mol) and the mixture was stirred. 11-bromoundecanol (16.88 g, 0.070 mol) was then added along with a catalytic amount of KI. The reaction was allowed to stir overnight, poured into water and filtered. The crude material was then recrystallized in toluene to give 14.58 g of **1** as a white powder in a 74% yield. ^{1}H NMR (300 MHz, DMSO-d_6) δ 9.77 (s, 1H), 7.51 – 7.40 (m, 2H), 6.89 – 6.78 (m, 2H), 4.34 (s, 1H), 3.89 (t, *J* = 6.5 Hz, 2H), 2.00 (s, 3H), 1.75 – 1.60 (m, 2H), 1.40 (d, *J* = 12.6 Hz, 1H), 1.40 (s, 3H), 1.26 (d, *J* = 4.7 Hz, 13H). ^{13}C NMR (75 MHz, DMSO-d_6) δ 168.14, 154.88, 132.89, 120.94, 114.79, 67.96, 61.18, 33.01, 29.55, 29.47, 29.43, 29.26, 29.20, 26.00, 25.97, 24.25.

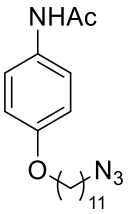

N-{4-[(11-azidoundecyl)oxy]phenyl}acetamide (**2**) **–** To a flame dried and argon purged 100 mL round bottomed flask equipped with a stir bar was added 50 mL of anhydrous DCM. Compound **1** (3.20 g, 0.010 mol) was added along with triethylamine (1.8 mL, 0.012 mol) to give an opaque white mixture. The mixture was then cooled to 0 °C in an ice bath and mesyl chloride (0.870 mL, 0.011 mol) was added dropwise. Upon the addition of the mesyl chloride the solution became clearer and was allowed to stir

at room temperature overnight. The reaction mixture was then poured into 100 mL water and extracted with DCM. The layers were separated, the organic portion was dried over $MgSO_4$, and the solvent removed *in vacuo* to give 3.51 g of an iridescent white solid that was used directly in the next step. The solid was dissolved in 45 mL of anhydrous DMF in a 250 mL round bottomed flask equipped with a stir bar. Sodium azide (0.640 g, 0.010 mol) was then added and the mixture was allowed to stir overnight. After completion of the reaction, the mixture was poured into 200 mL of water and filtered through a Buchner funnel. The crude material was then hot filtered in refluxing acetonitrile to give 1.80 g of **2** in a 58% yield. ^{1}H NMR (300 MHz, DMSO-d_6) δ 9.74 (s, 1H), 7.51 – 7.37 (m, 2H), 6.89 – 6.77 (m, 2H), 3.90 (t, *J* = 6.5 Hz, 2H), 3.31 (t, *J* = 6.8 Hz, 5H), 1.68 (p, *J* = 6.6 Hz, 2H), 1.52 (p, *J* = 7.1 Hz, 2H), 1.27 (s, 14H). ^{13}C NMR (75 MHz, DMSO-d_6) δ 168.12, 154.89, 132.90, 120.95, 114.81, 67.97, 51.08, 29.41, 29.34, 29.21, 29.19, 28.97, 28.69, 26.59, 25.97, 24.25.

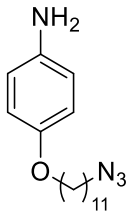

4-[(11-azidoundecyl)oxy]aniline (**3**) – Compound **2** (1.01 g, 0.0029mol) was massed into a 50 mL round bottomed flask equipped with a stir bar and reflux condenser. 200 proof ethanol (30 mL) was then added via syringe along with 3 mL of conc. HCl. The reaction was brought to reflux and allowed to react overnight. Upon completion, the reaction mixture was quenched by cooling to room temperature and carefully quenching with 40 mL of conc. $NaHCO_3$ solution. The aqueous portion was then extracted with ethyl acetate, and the organic layer separated and dried over $MgSO_4$. The solvent was removed *in vacuo* and the crude material purified via column chromatography using 3:1 hexanes/ethyl acetate as the elution solvent to give 0.425 g of **3** as an amber oil that slowly crystallizes on standing in a 48% yield. ^{1}H NMR (300 MHz, Methylene Chloride-d_2) δ 6.78 – 6.70 (m, 2H), 6.67 – 6.60 (m, 2H), 3.89 (t, *J* = 6.6 Hz,

2H), 3.46 (s, 2H), 3.29 (t, *J* = 7.0 Hz, 2H), 1.85 – 1.69 (m, 2H), 1.61 (q, *J* = 7.1 Hz, 4H), 1.53 – 1.26 (m, 14H). ^{13}C NMR (75 MHz, Methylene Chloride-d_2) δ 152.13, 140.27, 116.00, 115.49, 68.62, 51.52, 29.51, 29.44, 29.38, 29.11, 28.79, 26.68, 26.02.

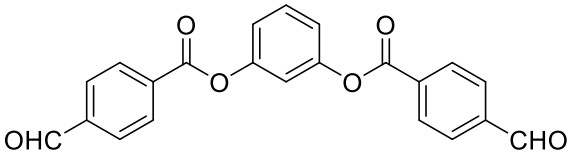

3-(4-formylbenzoyloxy)phenyl 4-formylbenzoate (**4**) – This compound has been previously reported. ^{1}H NMR (300 MHz, Methylene Chloride-d_2) δ 10.18 (s, 2H), 8.47 – 8.32 (m, 4H), 8.14 – 8.00 (m, 4H), 7.59 (tt, *J* = 7.6, 1.7 Hz, 1H), 7.32 – 7.21 (m, 3H). ^{13}C NMR (75 MHz, Methylene Chloride-d_2) δ 191.48, 163.91, 151.31, 130.70, 130.08, 129.56, 119.44, 115.68.

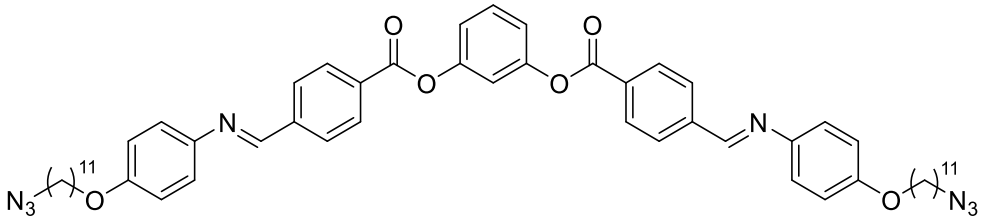

3-{4-[(E)-({4-[(11-azidoundecyl)oxy]phenyl}imino)methyl]benzoyloxy}phenyl-4-[(E)-({4-[(11-azidoundecyl)oxy]phenyl}imino)methyl]benzoate (**5**) **W899** – To a flame dried 25 mL round bottomed flask were added compound **3** (0.200 g, 0.00066 mol) and compound **4** (0.101 g, 0.003 mol). Absolute ethanol (10 mL) was then added via syringe along with two drops of acetic acid. The solution became progressively more opaque white after the addition of the acetic acid, and the reaction mixture was brought to reflux and allowed to react overnight. Upon completion of the reaction, the mixture was cooled in the freezer and filtered through a Buchner funnel. The solid was washed with cold ethanol and dried under a stream of air before being recrystallized in toluene to give 0.204g of **W899** as an off-white powder in an 80% yield. ^{1}H NMR (300 MHz, Methylene Chloride-d_2) δ 8.64 (s, 2H), 8.37 – 8.28 (m, 4H), 8.14 – 8.04 (m, 4H), 7.63 – 7.52 (m, 1H), 7.39 – 7.20 (m, 7H), 7.03 – 6.93 (m, 4H), 4.03 (t, J = 6.6 Hz, 4H),

3.29 (t, J = 7.0 Hz, 4H), 1.89 – 1.77 (m, 4H), 1.64 (d, J = 6.8 Hz, 4H), 1.36 (s, 29H). ^{13}C NMR (75 MHz, Methylene Chloride-d_2) δ 164.40, 158.59, 156.12, 151.51, 143.85, 141.29, 130.96, 130.45, 129.91, 128.45, 122.43, 119.35, 114.98, 68.33, 51.52, 29.51, 29.44, 29.35, 29.26, 29.12, 26.68, 25.99. HRMS [M-H]$^+$ -1.7 ppm off at 947.5184.

3.6.2 Total synthesis of W900

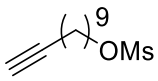

Undec-10-yn-1-yl methanesulfonate (**6**) – To a flame dried and argon purged 100 mL round bottomed flask equipped with a stir bar was added 40 mL freshly distilled THF. 10-undecenyn-1-ol (4.5 mL, 0.024 mol) was added and the solution was cooled to 0 °C in an ice bath. Triethylamine (6 mL, 0.043 mol) was added and the solution stirred for ten minutes. Mesyl chloride (2.5 mL, 0.033 mol) was then added dropwise via syringe resulting in the formation of a white precipitate. The solution was stirred over night at room temperature, after which the THF was removed *in vacuo* and the residue was dissolved in DCM and washed with water and brine. The layers were separated, and the organic portion was dried over $MgSO_4$. The solvent was removed *in vacuo* to give 5.39 g of **6** as a yellow oil in a 93% yield. ^{1}H NMR (500 MHz, Methylene Chloride-d_2) δ 4.22 (t, *J* = 6.6 Hz, 2H), 2.20 (td, *J* = 7.1, 2.7 Hz, 2H), 1.99 (t, *J* = 2.6 Hz, 1H), 1.80 – 1.71 (m, 2H), 1.58 – 1.50 (m, 2H), 1.46 – 1.27 (m, 11H).

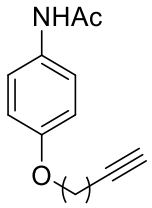

N-[4-(undec-10-yn-1-yloxy)phenyl]acetamide (**7**) – In a 100 mL round bottomed flask equipped with a stir bar was added compound **6** (5.39 g, 0.022 mol) and 40 mL DMF was added. K_2CO_3 (3.14 g, 0.022 mol) was then added followed by 4-acetamidophenol (3.13 g, 0.020 mol) and the solution was stirred for

three days. Upon completion of the reaction, the reaction mixture was poured into 300 mL water and extracted with ether. The layers were separated, and the organic portion was dried over $MgSO_4$. The solvent was removed *in vacuo* and the crude material was purified by recrystallization in acetonitrile to give 3.04 g of **7** as a white powder in a 51% yield. ^{1}H NMR (500 MHz, Chloroform-*d*) δ 7.41 – 7.35 (m, 2H), 7.23 (s, 1H), 6.87 – 6.83 (m, 2H), 3.93 (t, *J* = 6.6 Hz, 2H), 2.19 (td, *J* = 7.1, 2.6 Hz, 2H), 1.98 – 1.92 (m, 1H), 1.83 – 1.70 (m, 2H), 1.60 – 1.49 (m, 2H), 1.49 – 1.23 (m, 10H).

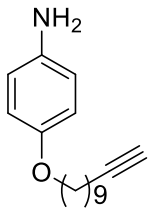

4-(undec-10-yn-1-yloxy)aniline (**8**) – Compound **7** (0.516 g, 0.0018 mol) was massed into a 25 mL round bottomed flask equipped with a stir bar. 10 mL of ethanol and 2 mL of water were then added along with $LiOH*H_2O$ (0.424 g, 0.010 mol) and the solution was brought to reflux for five days. Upon completion of the reaction, the mixture was cooled to room temperature and extracted with ether. The layers were separated, and the organic portion was dried over $MgSO_4$. The solvent was removed *in vacuo* and the crude material was purified using column chromatography with 90:5:5 hexanes/ethyl acetate/ethanol as the elution solvent giving 0.330 g of **8** as an amber oil in a 71% yield. ^{1}H NMR (500 MHz, Chloroform-*d*) δ 6.80 – 6.70 (m, 2H), 6.71 – 6.59 (m, 2H), 3.89 (t, *J* = 6.6 Hz, 2H), 3.43 (s, 2H), 2.20 (td, *J* = 7.1, 2.6 Hz, 2H), 1.96 (t, *J* = 2.6 Hz, 1H), 1.75 (dq, *J* = 7.9, 6.6 Hz, 2H), 1.54 (dtd, *J* = 8.8, 7.4, 5.9 Hz, 2H), 1.49 – 1.19 (m, 10H).

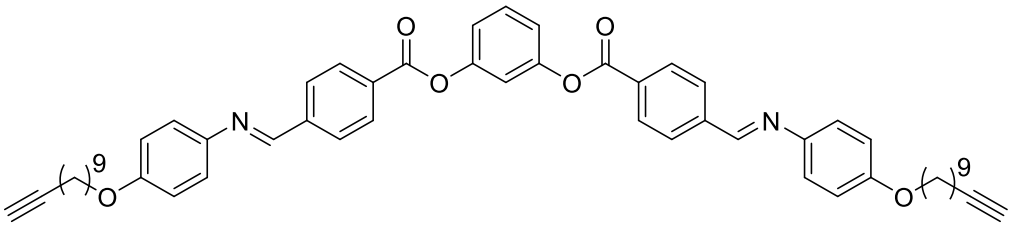

3-{4-[(E)-{[4-(dec-9-yn-1-yloxy)phenyl]imino}methyl]benzoyloxy}phenyl-4-[(E)-{[4-(dec-9-yn-1-yloxy)phenyl]imino}methyl]benzoate (**9**) **W900** – Compound **8** (0.580 g, 0.0022 mol) was added to a 50 mL round bottomed flask equipped with a stir bar and reflux condenser. 20 mL absolute ethanol was added giving a clear amber solution. Compound **4** (0.376 g, 0.001 mol) was then added along with a catalytic amount of acetic acid. The solution was brought to reflux and allowed to react for three hours. Upon completion of the reaction, the mixture was cooled to room temperature and filtered through a Buchner funnel. The solid was washed with cold ethanol and cold hexanes and dried. The crude material was purified by recrystallization in toluene to give 0.498 g of **W900** as an off-white powder in a 58% yield. ^{1}H NMR (500 MHz, Methylene Chloride-d_2) δ 8.63 (s, 2H), 8.36 – 8.27 (m, 4H), 8.13 – 8.04 (m, 4H), 7.62 – 7.53 (m, 1H), 7.38 – 7.29 (m, 4H), 7.29 – 7.22 (m, 3H), 7.02 – 6.93 (m, 4H), 4.02 (t, J = 6.6 Hz, 4H), 2.21 (td, J = 7.2, 2.7 Hz, 4H), 2.00 (t, J = 2.7 Hz, 1H), 1.87 – 1.77 (m, 4H), 1.62 – 1.30 (m, 24H). ^{13}C NMR (75 MHz, Methylene Chloride-d_2) δ 164.40, 158.58, 156.11, 151.52, 143.85, 141.29, 130.96, 130.45, 129.91, 128.45, 122.43, 119.35, 115.85, 114.98, 84.70, 68.32, 67.80, 29.40, 29.30, 29.26, 29.00, 28.71, 28.53, 25.97, 18.26.

4 Nanoconfinement of the Low Temperature Dark Conglomerate

4.1 Introduction

The inspiration for this project arose from the fact that the structure space for the HNF phase is very narrow. To design new materials, my goal was to address this issue *without* making small incremental changes to the molecular structure that are based solely on empirical data, which is cumbersome at best. The low temperature dark conglomerate phase (DC) phase of bent-core liquid crystals (BLCs) is closely related to the HNF phase, albeit with a much different phase morphology. Incorporating the DC phase materials into the HNF structure space would allow for additional design motifs and provide a larger foundation for a synthetic chemist working with these materials. Additionally, the underlying reason why a particular BLC material preferentially forms only one of the two morphologies is not well understood and probing the DC phase may help to illuminate the difference between the two phases.

4.2 The Dark Conglomerate Phase

Historically, spontaneous resolution of chiral conglomerates was first observed by Pasteur in his studies of racemic acid crystals.[49] Only within the past two decades has this same phenomenon been observed for fluid systems which was previously thought to be impossible because of the local environmental requirements for this type of discrimination.[3] Exclusion of enantiomers requires a high degree of molecular interaction to provide the energy needed for spontaneous chiral resolution and is generally found in crystalline systems. With the advent of bent-core liquid crystal (BLC) research, this same chiral behavior was observed in fluids and, remarkably, the molecules had no requirements to be chiral themselves.[4,50] The explanation for this phenomenon is a result of a broken symmetry that develops from the fact that these BLC molecules are inherently polar (due to the molecular bend) and

that they have a strong tendency to layer. This preference for layering is an intrinsic property of BLC structures that take advantage of strong molecular phase segregation. Traditionally the BLC is constructed of a rigid aromatic core that is coupled to flexible, aliphatic tails. These two molecular portions are mutually exclusive and drive the formation of layers where the cores and tails exist in their own distinct sublayers. Polarity and layering are not sufficient for chirality, however, and in order for chirality to develop, it is required that the molecules tilt within the layer as well.[3,4,8] This tilt is strongly promoted by the presence of two tails flanking the aromatic core. The volume taken up by the tails is large compared to the core, and to maximize the volume available for the tail to occupy, the cores tilt. The three characteristics of layering, polarity, and tilt combine to break the internal mirror plane of symmetry present in the layer and generate a chiral layer structure with the handedness of the layer determined by the direction of the molecular tilt (**Figure 4.1**).[4]

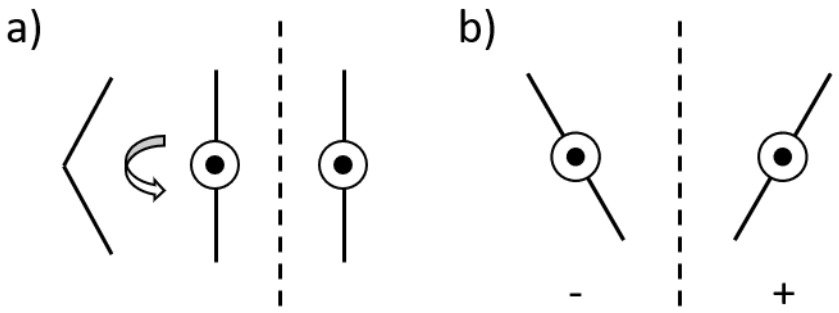

Figure 4.1 – BLCs (shown schematically to the left, 90° rotation of the BLC gives the circle /dot representation which indicates the molecule is bending out of the plane of the page) have a strong tendency to layer. When the molecules are un-tilted (a) the mirror plane within the layer is retained. In (b) the molecules are tilted in opposite directions showing the development of layer chirality.

This layer chirality is observed in many of the phases formed by BLC including the B2, HNF, B7, and the dark conglomerate (DC) phase with focus on the latter discussed here.[8,51] The DC phase is characterized by the formation of toric focal conic domains constructed of curved smectic layers that that form a three-dimensional interpenetrating network of tubes and is commonly referred to as the

"plumber's nightmare".[50] The mechanism by which this phase forms is again the result of the upper and lower halves of the constituent molecules tilted in orthogonal directions, destabilizing a planar

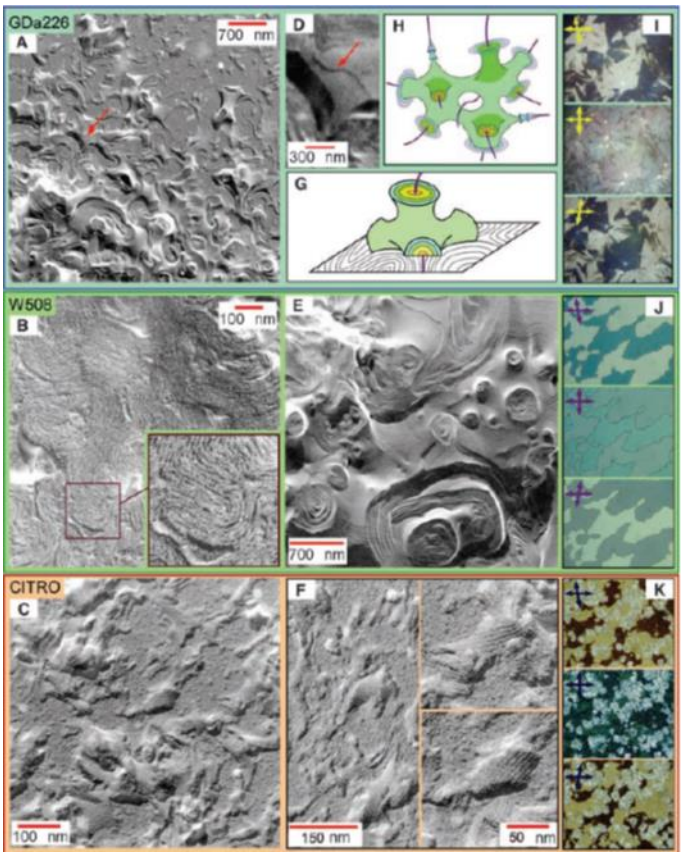

Figure 4.2 - FFTEM and POM images of three different DC forming compounds. In all cases, the curved smectic layers of toric focal conics were observed in the TEM and chiral conglomerate domains were seen in the POM.[51]

configuration of the layers, providing saddle deformed layers (hyperbolic paraboloids with negative gaussian curvature). In the polarized optical microscope (POM) the phase appears dark under crossed polarizers and reveals the formation of large chiral domains when the polarizers are de-crossed with the chirality arising from the layer.[50] The structure of the phase has been directly observed by freeze-fracture transmission electron microscopy (FFTEM) to reveal continuously curving smectic layers that construct the sponge-like structure of the phase (**Figure 4.2**).[50] Traditionally, this phase is observed directly upon cooling from the isotropic phase, in compounds that have B2 or B7 phases, and is fluid. In

some materials, application of a sufficiently strong electric field will yield a B2 phase from the DC indicating that the local environment is similar in both cases.[50] However, recently it was reported that a new type of DC phase exists and can appear below the B2 phase of certain molecules. This new phase is characterized by the formation of crystalline order within the layer and no longer responds to the application of an electric field. To distinguish this phase from the higher temperature DC phase, the label "low-temperature DC" phase was coined and is the phase considered for the rest of this chapter.[52]

4.2.1 The Low Temperature Dark Conglomerate Phase

The low temperature dark conglomerate (DC, again not to be confused with the high temperature fluid DC phase) phase is characterized by the formation of disordered toric focal conics that have crystalline in-plane ordering that was first reported for compound W624.[52,53] Initial work was conducted on W624 and its homologs and it was reported that the family was comprised of BLC materials all of which possessed a B4-to crystal transition that had not been observed before.[53] This was unusual as no other compounds had been reported as having other phases forming at a lower temperature than the B4, and the crystalline nature of the B4 phase would make this unlikely. Polarized optical micrographs for these materials revealed the characteristic blue color of the B4 phase but had a texture resembling the rings of trees, which was different from previously reported B4 forming compounds.[7,53] X-ray diffraction (XRD) experiments on these materials revealed a broad layer reflection peak coupled with three wide-angle peaks indicating crystalline structures with short layer correlation length scales, also reported in B4 forming materials.

When compound W624 was first reported, the structure of the B4 phase had not been confirmed, and it wasn't until the Boulder group utilized FFTEM, x-ray, and electron diffraction (XRD and ED) to directly observe the nature of the B4 phase (also referred to as the HNF phase). From the FF-TEM results, it was concluded that the phase was constructed by bundles of helical filaments with coherent twist giving racemic conglomerate domains.[7] The XRD and ED experiments revealed the orthogonal

orientation of the molecular halves and helped to prove the deformation of planar layers into saddles. This data eliminated any confusion as to the nature of the phase, removing the twist grain boundary (TGB) phase and other phase morphologies as possibilities, concluding that the phase is characterized by the formation of these filaments. With these results in hand, the same group at Boulder used these techniques to study the low temperature DC phase in order to understand its nanoscale morphology. FFTEM images confirmed that the phase assignment given to W624, in its initial

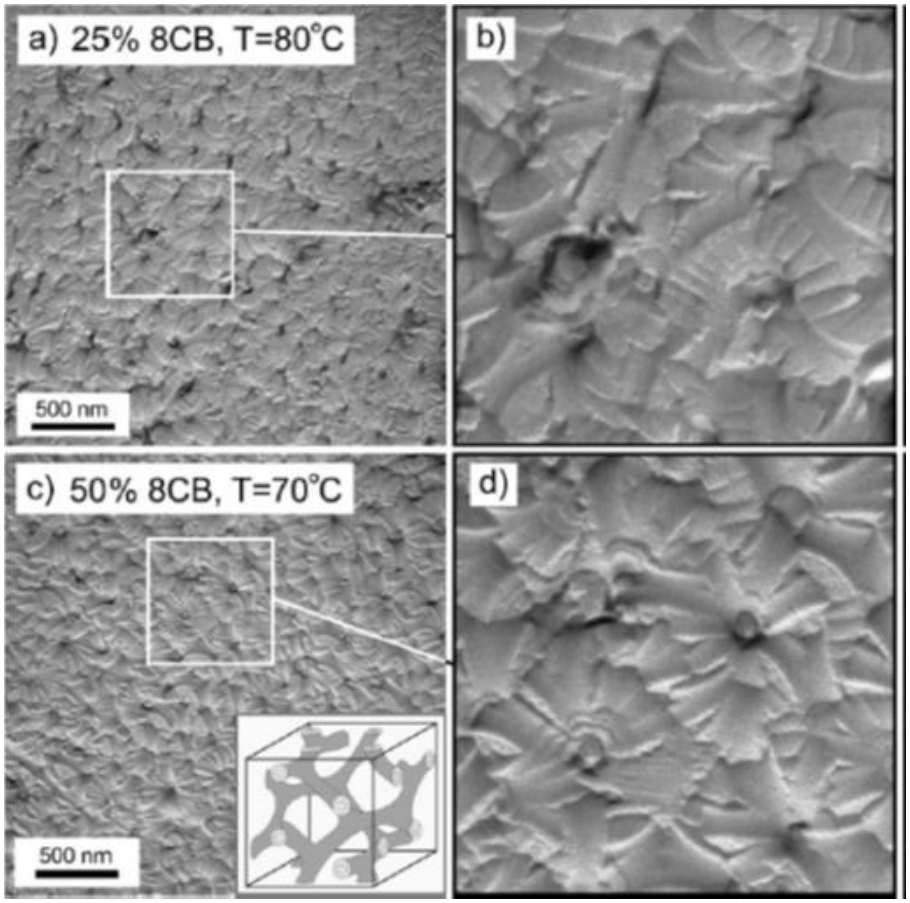

Figure 4.3 - FFTEM images of W624 diluted with 8CB. The images show the cubic bicontinuous network of the DC phase and filaments were not observed anywhere in the sample, indicating that W624 has a bulk phase morphology that differs from the HNF phase.[53]

reporting of forming the B4 (HNF) phase, was incorrect because filaments were not observed in the bulk sample. Dilution of the phase with a liquid crystal solvent (a technique commonly used to help elucidate the structure of complex phases) yielded a cubic bicontinuous network of saddle deformed layers as

further evidence that filaments were not being formed (**Figure 4.3**). This was the first documentation of a phase that is thermodynamically similar to the HNF phase with a distinctly different morphology. Both the HNF phase and the DC phase are stable at and below room temperature and both pass through a glass transition as they cool. The question then arose as to why certain materials would preferentially form one morphology, when there seems to be no clear difference between the two.

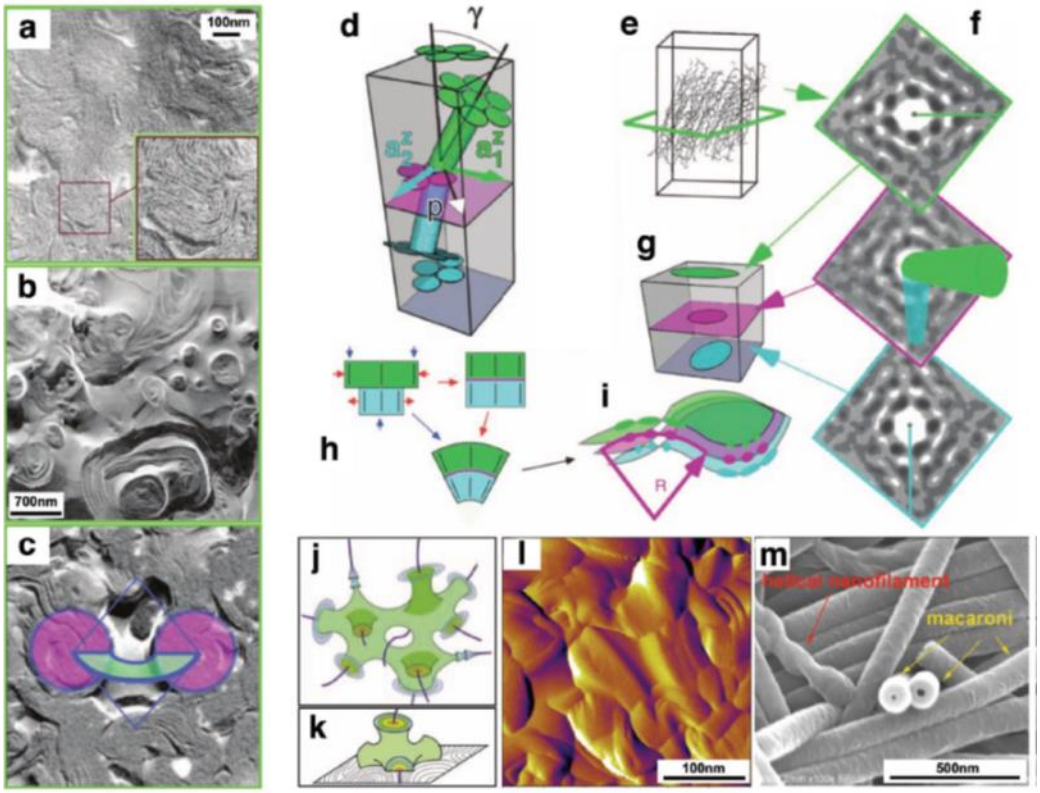

Figure 4.4 – (a-c) FFTEM images of the DC phase showing the toric focal conics structure. (d-i) an illustration showing the mechanism by which the DC phase forms. (j-m) AFM and SEM images of the trimorphic behavior of 12OAz5AzO12. The morphology changes as a function of dodecane solvent, giving the DC morphology as the bulk phase that then transitions to helical filaments and cylinders as the solvent concentration increases.[10]

To understand the nature of both phases and probe the difference in how these two phases are formed, experiments were conducted involving the blending of materials, where the DC/B4 phase assignment was ambiguous, with different solvents. For one material, 12OAz5OAz12, it was observed that the neat bulk morphology was “spongey” indicating that the thermodynamically favored

morphology was the DC (**Figure 4.4**l,m).[8] Upon addition of n-dodecane, the morphology changed first to HNFs, and finally to a cylindrical "macaroni" type morphology which depended on the concentration of the n-dodecane present.[8] This unprecedented tri-morphic behavior is interesting as both the DC and HNFs are formed from saddles which are minimal surfaces, whereas cylinders have positive curvature and are not. The presence of the non-polar solvent changes the growth mode of the forming phase and must stabilize the elastic strain present in the saddle-deformed layers, giving the cylindrical morphology. However, the thermodynamic differences are still not apparent. The most notable difference in the phases is the appearance of the structures formed. The sponge-like structure of the DC phase forms in a seemingly three-dimensional fashion since the structure forms a continuous network throughout the bulk, whereas the HNF phase is relatively one-dimensional giving filaments that have large aspect ratios. This led to the hypothesis that the kinetics of crystal growth for the DC phase must be more uniform in all three directions, unlike the HNFs which must grow much faster along the filament axis. To test this, it was decided to utilize the nanoscale pores of anodized aluminum oxide (AAO) membranes to study the growth of the phase under nanoconfining conditions.

4.2.2 Crystallization and LCs in Nanoconfinement

To understand the effects of confinement on the growth of crystals and liquid crystals, it is necessary to first understand the bulk (unconfined) behavior. Crystallization begins when a group of molecules aggregate to form a nucleus.[54] This nucleus is then subject to the competing effects of forming a new surface interface with its surroundings, and the energies associated with the interaction of the constituent molecules. The interaction of the molecules is a stabilizing effect and is known as the volume free energy (ΔG_{volume}), whereas the formation of a new surface is destabilizing and is labeled the surface free energy (γ).[55] Thus, the fate of the nucleus is determined by whether the volume free energy can outcompete the surface free energy, and is dependent on a critical nuclear radius, r (**Eqn. 1**).

$$\boldsymbol{Eqn.1} - \Delta G_{cryst} = \frac{4}{3}\pi r^3 \cdot \Delta G_{volume} + 4\pi r^2 \cdot \gamma$$

Once the nucleus reaches this critical radial size, the volume free energy dominates and crystallization is spontaneous (**Figure 4.5**).[56] The situation is complicated when a material forms more than one crystal habit, referred to as a polymorph. For a certain polymorph to be formed, the constituent nucleus must have the same form as the daughter crystal since the underlying molecular arrangement of the nucleus will be repeated throughout the entire crystal. This then leads to a competition between the relative stabilities of the possible forms of the crystal nuclei. One nucleus may be more stable overall but requires a larger critical radius (due, for example, to a larger surface tension γ) for the crystallization to become spontaneous, while the less stable polymorph may grow faster due to less stringent requirements for nuclear size (**Figure 4.5**).

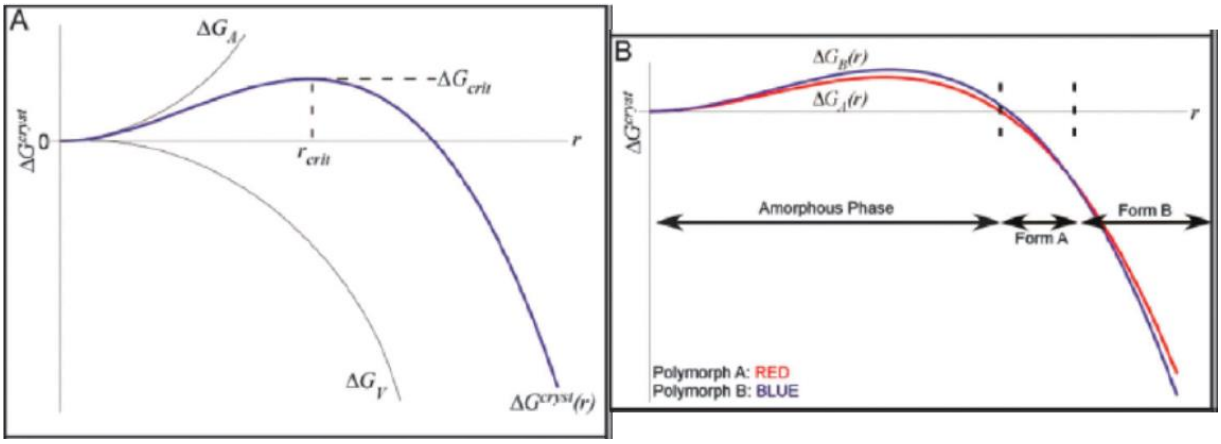

Figure 4.5 – (a) A plot of ΔG^{cryst} versus nuclear radius (r) showing the how spontaneous crystallization is dependent on a critical nuclear radius. (b) The competition of crystallization speed versus stability for two polymorphs. Form A requires a smaller critical radius for crystallization and therefore forms faster than Form B.[57]

This phenomenon is similar to thermodynamic versus kinetic products of chemical reactions. Since organic nuclei are on the tens of nanometer length scale, these competing effects become pronounced in confined geometries of nanoscale pores.[54]

Confinement in nanoscale geometries physically inhibits the size of the nuclei available to the system during a crystallization event. This often results in deviation from bulk behavior and different crystal polymorphs, even those never before observed for a material, may be formed.[55–57] Additionally, highly aligned porous systems such as AAO and block-copolymer monoliths allow for the study of crystal orientation within the pores.[56] It is observed that under these conditions the fast axis of crystallization is parallel to the pore axis and has been seen in various small molecule and polymeric systems.[57] As the crystal nucleus forms, if the fast axis of growth is aligned perpendicular to the pore axis, the physical boundary of the pore wall will be quickly encountered by the growing crystal front and, (in sufficiently small pores) the critical radius for crystallization will not be reached resulting in spontaneous dissolution of the nucleus. However, when the fast axis is aligned parallel to the pore, the crystal front is not impeded by the pore wall, and crystallization becomes spontaneous, an effect that has been compared to natural selection in nature.[56]

Nanoconfinement of the HNF Phase

The HNF phase has been studied under conditions of nanoconfinement in an attempt to generate a composite system in which individual pores are decorated with individual crystals for a variety of applications.[20] Apart from the fact that under these conditions, individual filaments populate each individual pore (ranging from 30-80 nm in diameter), the growth mode of the filaments was changed from the growth mode observed in bulk. Traditionally, the HNF phase is constructed of bundles of twisted layers with the central layer possessing negative gaussian curvature and center of mass lying along a straight line, and outer layers deviating from perfect negative curvature which results in a self-limiting of the filaments width.[9] However, within the pores it was observed that individual helical filaments were formed, this time with varying degrees of positive curvature, and widths up to twice the observed width for bulk samples (**Figure 4.6**).

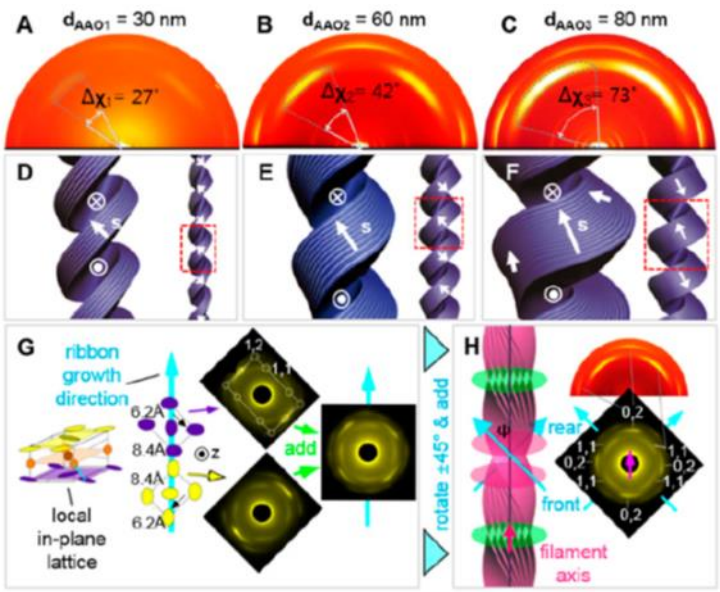

Figure 4.6 – (a-c) 2D GWAXS plots showing the molecular orientation with in the pores of AAO confined NOBOW ranging from 30-80nm. (d-f) Illustrations showing the orientation of the layers of the filaments within the AAO pores. (g,h) Comparison of the ED patterns of bulk NOBOW with the GWAXS scattering patterns of nanoconfined NOBOW.[20]

In bulk, the deviation from negatively curved layers imparts an elastic strain that promotes a bifurcation of the filament tip when the filament grows too wide.[9] Under confinement, the presence of the AAO pore surface acts as a heat sink through which the growing filament releases heat as crystallization occurs, this bypasses the bifurcation growth mode, and the crystallization front follows the curvature of the AAO pore.[20] The result is filaments with positive curvature and centers of mass that now lie along a helix instead of a straight line. This new type of helical filament may be a polymorph of the studied HNF materials and has not been observed under other conditions. Since the DC phase and HNF phase maintain the same underlying layer arrangement with different bulk phase morphologies, it was relevant to study the DC phase under the same nanoconfining conditions to see whether or not the sponge-like morphology would give way to the same helical morphology in the pores.

4.3 Hypothesis

The HNF and DC phases of BLC molecules show the same local layer structure but present different bulk morphologies. The DC phase is characterized by the formation of nanoscale toric focal conics while the HNF phase is constructed of bundles of twisted layers. Though the local layer structure is similar in both phases, materials that form these phases tend to form one morphology in preference to the other. Targeted control of the nanostructures would provide pathways to potential applications and insight into how conditions drive specific phase formation. Here, W624, a compound known to form the DC phase, is confined in nanometer scale channels of porous anodized aluminum oxide (AAO) membranes. Within each nanochannel, the DC phase is suppressed forming the HNF structure instead, indicating the nanoscale spatial limitation can control the phase structure of the DC phase.

4.4 Experimental

W624 was synthesized using the procedures reported by Nádasi et al. and the porous AAOs were synthesized with the electrochemical method as reported previously.[53,58,59] For the 60 and 100 nm pores, oxalic acid was used as electrolyte and malonic acid was used for the 200 nm pore. The channel length of the AAO membrane was set to be 5 µm. The morphological behavior of W624/AAO composites were characterized by scanning electron microscopy (SEM) to directly visualize the phase morphology in the pores and grazing incidence x-ray diffraction (GIXD) to give information on the orientation of the layers and their constituent molecules.[60] Two dimensional (2D) GIXD was conducted at the 9A U-SAXS and 6D C&S UNIST-PAL beamlines of Pohang Accelerator Laboratory. An X-ray beam with a focused energy of 11.04 keV was incident on the sample with an angle of 0.12°. The sample-to-detector distance (SDD) was set to be 200 mm and 400 mm for relatively small-angle and wide-angle measurements respectively. Diffraction patterns were recorded using a Rayonix 2D SX165 detector.

4.5 Results

4.5.1 GIXD

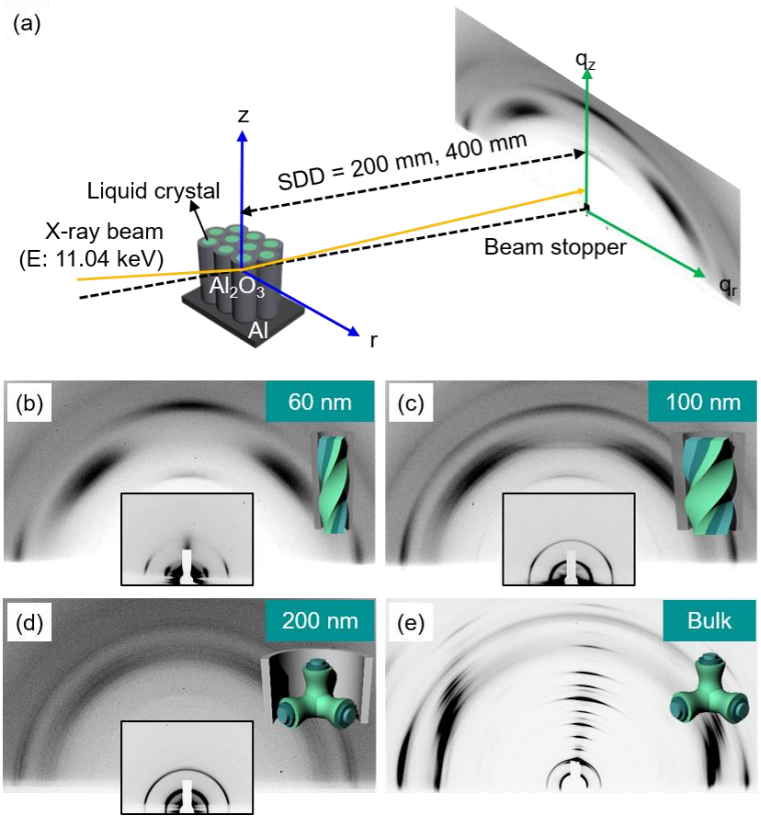

Figure 4.7 – (a) GIXD experimental set-up. (b-d) WAXS and SAXS (inset) plots of pourous AAO membranes ranging in diameter from 60-200 nm populated with W624. The plots in the 60 and 100 nm pores are nearly identical to those of HNF forming compound NOBOW indicating similar behavior of the two materials. The 200 nm pore shows a return to bulk behavior in W624. (e) A WAXS plot of a drop of W624 on alumina.

The bulk behavior of W624 was characterized by using GIXD to study a drop of the material on a flat aluminum oxide substrate which provides the same conditions as in the AAO channels. The GIXD pattern of bulk W624 shows sharp peaks instead of diffuse rings suggesting the formation of an ordered lamellar structure (**Figure 4.7**e). However, when W624 is confined in the AAO pores, a behavior similar to that of P-9-OPIMB (NOBOW, a prototypical HNF forming compound) is observed (**Figure 4.7**b-d). In the 60 nm and 100 nm pores, the wide-angle region gives strong reflections at 0°, 45°, 90°, 135° and 180° which are due to scattering off the core-arm and tail sublayers. Additionally, the small-angle region

gives scattering at 0° and 180° that indicates a vertical orientation of the layers. As the pore size increases, the change in the range of angle of scattering is observed indicating that the filament's structure is changing as it gets wider. The layers become more positively curved in the larger pores and the layer orientation changes from being vertical and parallel to the pore axis, to being tilted at some angle relative to this axis. In the 200 nm pore it can be clearly seen that the sharp reflection peaks are lost, and diffuse rings instead take their place. When compared to the GIXD patterns obtained from NOBOW (**Figure 4.6**a-c), both systems give nearly identical results, suggesting a similar behavior for both materials.

4.5.2 SEM

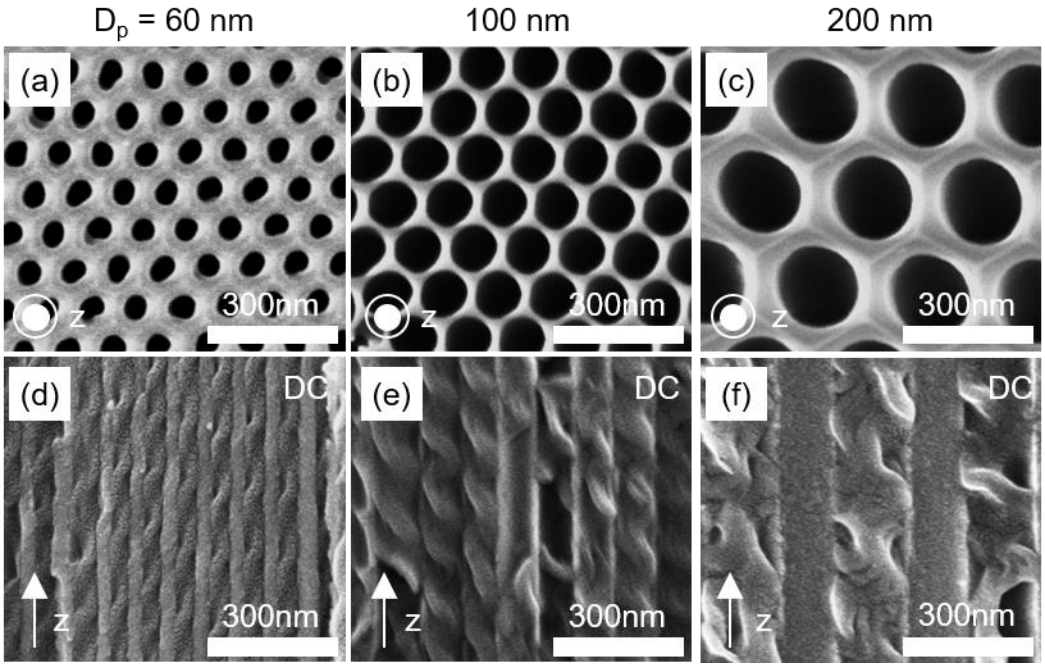

Figure 4.8 – (a-c) SEM images showing the bare pores of the AAO membranes ranging from 60-200 nm in diameter. (d-f) SEM images of the pores populated with W624. In (d) and (e), clear HNF structures are observed. In the 200 nm pore (f) a return to the bulk sponge-like morphology is seen.

SEM images of W624 in the 60 nm and 100 nm pores show the sole formation of individual filaments in the absence of other topological features (**Figure 4.8**). In the 60 nm pore it is observed that the filaments formed are constructed of layers that are nearly vertical, and the overall structure more

closely resembles a traditional helical filament observed in bulk HNF samples. These observations coincide with the GIXD data mention earlier. As the pore diameter widens, we can see behavior in W624 that mimics the nanoconfined HNFs. The filament layers deviate from being co-linear with the pore axis and negative curvature yields to positive, giving a filament that is twice the diameter of native bulk filaments. Again, when coupled with the GIXD results, these observations confirm the same morphological features for the DC phase and the HNF phase. When the pore diameter is widened to 200 nm a return to bulk behavior is observed and no filaments are seen. Instead, W624 forms the spongey features of the DC phase. These results from W624 are in very good agreement with the behavior of the previously reported nanoconfined HNF forming material P-9-OPIMB. This indicates the process of nanoconfining materials that form the DC phase (W624) forces a structural change in the morphology of the growing phase, eliminating the ability for the material to form the 3D disordered structure and instead requiring the material to adopt the HNF motif.

4.6 Discussion

Polymorphism is a phenomenon seen throughout nature including molecular crystals and liquid crystalline systems.[54] Nanoconfinement of molecular crystals can promote the formation of particular polymorphs over others, as well as polymorphs that have never been observed, providing a way to control morphology.[55–57] Since organic crystalline nuclei have radial sizes on the nanometer scale, this spatial limitation allows only for nuclei smaller than the pore diameter to be realized. Additionally, the anisotropic environment of the AAO pores induces alignment of the fast axis of crystal growth to be parallel to the pore axis. Here, the spatial confinement of the DC phase in the nanoscale AAO pores inhibits growth of the phase radially allowing for crystallization to occur only along the pore axis, effectively aligning the fast axis of growth with the pore. Additionally, confinement of the phase in pores up to 100 nm in diameter, prevents the phase from achieving the appropriate critical radius needed for

a crystal nucleus to realize the DC morphology. These effects combine to result in the formation of HNFs exclusively in the pores.

In the bulk, the DC phase forms a more three-dimensional "sponge-like" morphology requiring crystal growth to be effectively uniform in all directions. HNFs instead grow much faster in one direction due to increased strain associated with making the filament wider. Since the saddle deformed layers of the HNFs are doubly ruled surfaces with negative gaussian curvature, only the central layer has the ideal curvature. Adding additional layers deviates from this ideal curvature, costing energy. To minimize the elastic free energy that is required for lateral growth, HNFs would rather split forming a new filament instead of growing wider.[9] Thus, the lateral growth rate is slower compared to growth in the axial direction where this elastic strain cost is absent. Within the environment of the AAO pores, this bifurcation growth mode is bypassed due to the presence of a thermal gradient at the crystal growth front/pore wall interface. This lowers the free energy of nucleation at the pore wall relative to the bulk, localizing nucleation at the interface.[20] The AAO pore has a significantly higher thermal conductivity allowing for the heat expelled from the crystal front to be transferred away promoting growth along the pore wall. Since the both the DC and HNF phases experience the same layer deformation during phase formation, and the length scales of the deformation are similar, the DC phase must also experience the same elastic strain cost associated with making the layers wider. However, what differs, is the way a DC saddle grows when compared to the saddle of an HNF. Propagation of a saddle deformed layer in the DC occurs in two dimensions where as an HNF layer saddle grows more easily in one dimension, along the helix axis. Even though the bulk DC layer saddle can propagate in two dimensions, growth in both dimensions still operates under the tip splitting regime (familiar to the HNF system), and the disordered focal conic structure is formed. It follows that growth of the DC phase under confinement is then promoted by the same thermal gradient as seen for the nanoconfined HNF system reported before. As the layers of the DC deform into saddles and the material crystallizes, the growth mode is changed from

tip splitting to occurring along the pore wall, giving the helicoidal structures observed. Additionally, the spatial constraints physically prevent any growth radially. In the 200 nm pore a return to bulk behavior is seen because these constraints are looser, and growth can now occur away from the pore wall allowing for the traditional method for DC crystallization to occur.

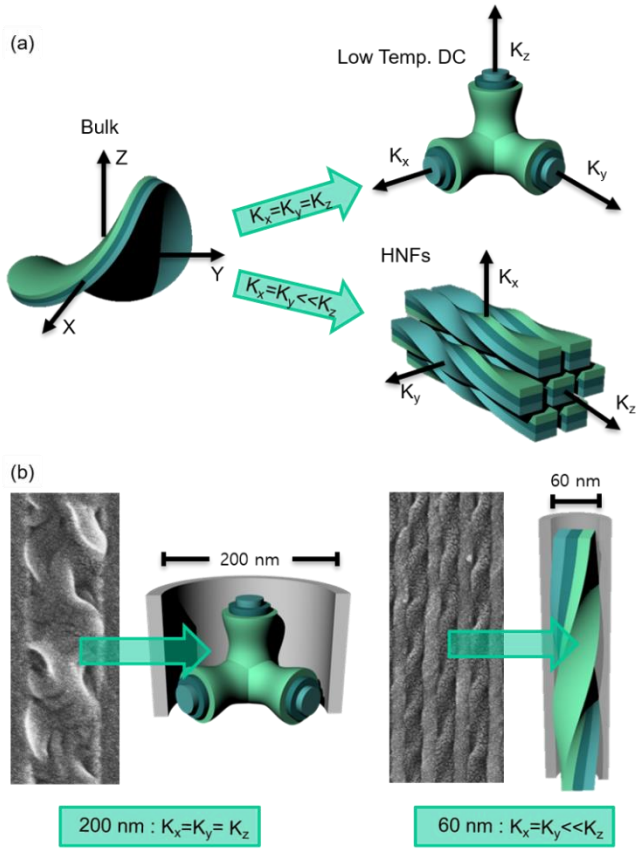

Figure 4.9 – (a) In the bulk, the saddles can give either the three-dimensional sponge structure of the DC phase or the one-dimensional helical structure of the HNF phase. From a kinetic stand point, growth of the DC phase must be more uniform in all three dimensions when compared to the HNFs which have a dominant growth direction. (b) Confinement of the DC phase forces the growth profile of the phase to adopt that of the HNF phase resulting in the formation of HNFs in pores with a diameter less than or equal to 100 nm.

Another explanation for these observations is to look at the system from a kinetic point of view. Confining the DC phase in the highly anisotropic environment of the AAO pores effectively forces the system to adopt the kinetic profile of a growing HNF, which could also result in the formation of filaments in the pores (**Figure 4.9**). As the nucleus of the DC phase fills the pore, the rate constants for

growth in the directions perpendicular to the pore axis become zero when the growth front contacts the pore wall, leaving only growth along the pore axis available. In the 200 nm pore, the spatial constraints are much looser. The formation of crystalline nuclei with the appropriate critical radius for DC formation are allowed, as well as a kinetic growth profile that matches bulk behavior, resulting in formation of the "sponge-like" morphology of the DC phase in the larger pore.

4.7 Conclusions/Future Work

Nanoconfining molecular crystals provides information on the thermodynamic and kinetic characteristics of a given system. It has been used to exploit the nanoscale features of crystal nuclei to understand crystallization events in a variety of systems including liquid crystals. Here, nanoconfining the DC phase of compound W624 shows that the DC system will form filaments identical to those of traditional HNF forming compounds (e.g. NOBOW). Apart from the fact that this is the first reported example of a material with the ability to form either the DC or HNF morphologies by directed use of nanoconfinement, it is also interesting as we have two polymorphs forming from the same saddle shaped nucleus. Traditionally, it is the underlying arrangement of molecules in the nucleus that determine the crystal habit. Therefore, one should expect to only one polymorph per nuclear type. However, geometrically, saddles can combine in multiple ways to give different minimal surfaces (e.g. helices and hyperboloids). Thus, in the case of the saddle shaped nuclei for both the DC and the HNF phases, both morphologies are possible. The confined conditions of the AAO pores provide the DC phase the appropriate environment for the formation of HNFs that is absent under bulk conditions. This is due to the physical prevention of the phase to propagate in two dimensions coupled with the bypassing of the tip splitting growth mode of the phase.

Molecular anchoring of the confined materials also has a profound effect on the behavior of the phase in the pores. In the AAO system, it has been observed that the bare pore wall strongly induces a planar anchoring of the BLC compounds giving layers that are oriented perpendicular to the pore axis in

the higher temperature smectic phases.[60] With W624 we were unable to observe the behavior of the material in its B2 phase, and due to time constraints with the beam line in Korea, these studies were postponed. It would be interesting to revisit this phase to observe whether the system behaves the same way as NOBOW in its own B2 phase and if the molecules are also planar aligned within the pores. Additionally, further work should include changing the surface energy of the pore wall by coating the pores with materials that promote homeotropic anchoring, for example OTS. Blends of NOBOW with 5CB in the AAO pores were also studied and remarkably the filaments formed with much more negative curvature, a behavior associated with the bulk material.[61] Blends of W624 with 5CB would also be an interesting investigation to see if W624 returned to forming a sponge-like morphology even in the pores less than 100 nm in diameter, or if HNFs are again formed with similar features as the NOBOW/5CB blends.

Finally, formation of the HNFs within the nanoconfined DC not only provides a new platform for understanding the behavior of these phases, but also yields a new scaffold for functional nanocomposites and has unified the structure space for all the phases formed by saddle deformed layers. Continued studies of these systems will undoubtedly lead to a more fundamental understanding of these phases and provide new applications for these materials.

References

[1] M. Todisco, T. P. Fraccia, G. P. Smith, A. Corno, L. Bethge, S. Klussmann, E. M. Paraboschi, R. Asselta, D. Colombo, G. Zanchetta, et al., *ACS Nano* **2018**, DOI 10.1021/acsnano.8b05821.

[2] Peter J. Collings, *Liquid Crystals Nature's Delicate Phase of Matter*, Princeton University Press, **1990**.

[3] R. A. Reddy, C. Tschierske, *J. Mater. Chem.* **2006**, *16*, 907–961.

[4] D. R. Link, G. Natale, R. Shao, J. E. Maclennan, N. A. Clark, E. Körblova, D. M. Walba, *Science* **1997**, *278*, 1924–1927.

[5] J. Szydlowska, J. Mieczkowski, J. Matraszek, D. W. Bruce, E. Gorecka, D. Pociecha, D. Guillon, *Phys. Rev. E* **2003**, *67*, 031702.

[6] D. A. Coleman, J. Fernsler, N. Chattham, M. Nakata, Y. Takanishi, E. Körblova, D. R. Link, R.-F. Shao, W. G. Jang, J. E. Maclennan, et al., *Science* **2003**, *301*, 1204–1211.

[7] L. E. Hough, H. T. Jung, D. Krüerke, M. S. Heberling, M. Nakata, C. D. Jones, D. Chen, D. R. Link, J. Zasadzinski, G. Heppke, et al., *Science* **2009**, *325*, 456–460.

[8] K. V. Le, H. Takezoe, F. Araoka, *Adv. Mater.* **2016**, 1602737.

[9] D. Chen, J. E. Maclennan, R. Shao, D. K. Yoon, H. Wang, E. Korblova, D. M. Walba, M. A. Glaser, N. A. Clark, *J. Am. Chem. Soc.* **2011**, *133*, 12656–12663.

[10] D. Chen, C. Zhu, H. Wang, J. E. Maclennan, M. A. Glaser, E. Korblova, D. M. Walba, J. A. Rego, E. A. Soto-Bustamante, N. A. Clark, *Soft Matter* **2013**, *9*, 462–471.

[11] R. A. Callahan, D. C. Coffey, D. Chen, N. A. Clark, G. Rumbles, D. M. Walba, *ACS Appl. Mater. Interfaces* **2014**, *6*, 4823–4830.

[12] A. W. Hains, Z. Liang, M. A. Woodhouse, B. A. Gregg, *Chem. Rev.* **2010**, *110*, 6689–6735.

[13] C. W. Tang, *Appl. Phys. Lett.* **1986**, *48*, 183–185.

[14] J. Kim, K. Kim, S. Hwan Ko, W. Kim, *Sol. Energy Mater. Sol. Cells* **2011**, *95*, 3021–3024.

[15] A. Mishra, P. Bäuerle, *Angew. Chem. Int. Ed.* **2012**, *51*, 2020–2067.

[16] G. Yu, J. Gao, J. C. Hummelen, F. Wudl, A. J. Heeger, *Science* **1995**, *270*, 1789–1791.

[17] K. M. Coakley, M. D. McGehee, *Chem. Mater.* **2004**, *16*, 4533–4542.

[18] J. S. Kim, Y. Park, D. Y. Lee, J. H. Lee, J. H. Park, J. K. Kim, K. Cho, *Adv. Funct. Mater.* **2010**, *20*, 540–545.

[19] B. Kannan, K. Castelino, A. Majumdar, *Nano Lett.* **2003**, *3*, 1729–1733.

[20] H. Kim, S. Lee, T. J. Shin, E. Korblova, D. M. Walba, N. A. Clark, S. B. Lee, D. K. Yoon, *Proc. Natl. Acad. Sci.* **2014**, *111*, 14342–14347.

[21] D. K. Yoon, Y. Yi, Y. Shen, E. D. Korblova, D. M. Walba, I. I. Smalyukh, N. A. Clark, *Adv. Mater.* **2011**, *23*, 1962–1967.

[22] Eric D. Carlson, Lee M. Foley, Edward Guzman, Eva Korblova, Rayshan Visvanathan, SeongHo Ryu, *Proc SPIE 10361 Liq. Cryst. XXI* **2017**, *1036118*, DOI 10.1117/12.2280569.

[23] J. Michl, E. W. Thulstrup, *Tetrahedron* **1976**, *32*, 205–209.

[24] H. Xin, X. Gao, *ChemPlusChem* **2017**, *82*, 945–956.

[25] S. V. Shevyakov, H. Li, R. Muthyala, A. E. Asato, J. C. Croney, D. M. Jameson, R. S. H. Liu, *J. Phys. Chem. A* **2003**, *107*, 3295–3299.

[26] Y. Yamaguchi, K. Ogawa, K. Nakayama, Y. Ohba, H. Katagiri, *J. Am. Chem. Soc.* **2013**, *135*, 19095–19098.

[27] Y. Yamaguchi, M. Takubo, K. Ogawa, K. Nakayama, T. Koganezawa, H. Katagiri, *J. Am. Chem. Soc.* **2016**, *138*, 11335–11343.

[28] A. G. Anderson, J. A. Nelson, J. J. Tazuma, *J. Am. Chem. Soc.* **1953**, *75*, 4980–4989.

[29] K. Hafner, H. Weldes, *Justus Liebigs Ann. Chem.* **1957**, *606*, 90–99.

[30] R. N. McDonald, H. E. Petty, N. L. Wolfe, J. V. Paukstelis, *J. Org. Chem.* **1974**, *39*, 1877–1887.

[31] K. Kurotobi, M. Miyauchi, K. Takakura, T. Murafuji, Y. Sugihara, *Eur. J. Org. Chem.* **2003**, *2003*, 3663–3665.

[32] T. Nozoe, *Proc Jpn Acad* **1952**, 483–487.

[33] Klaus Hafner, Klaus-Peter Meinhardt, *Org. Synth.* **1984**, *62*, 134.

[34] P.-W. Yang, M. Yasunami, K. Takase, *Tetrahedron Lett.* **1971**, *12*, 4275–4278.

[35] E. Amir, R. J. Amir, L. M. Campos, C. J. Hawker, *J. Am. Chem. Soc.* **2011**, *133*, 10046–10049.

[36] K. Kurotobi, A. Osuka, *Org. Lett.* **2005**, *7*, 1055–1058.

[37] S. E. Estdale, R. Brettle, D. A. Dunmur, C. M. Marson, *J. Mater. Chem.* **1997**, *7*, 391–401.

[38] A. Zep, M. Salamonczyk, N. Vaupotič, D. Pociecha, E. Gorecka, *Chem. Commun.* **2013**, *49*, 3119–3121.

[39] E. Tsai, J. M. Richardson, E. Korblova, M. Nakata, D. Chen, Y. Shen, R. Shao, N. A. Clark, D. M. Walba, *Angew. Chem. Int. Ed.* **2013**, *52*, 5254–5257.

[40] D. Pociecha, D. Kardas, E. Gorecka, J. Szydlowska, J. Mieczkowski, D. Guillon, *J. Mater. Chem.* **2003**, *13*, 34–37.

[41] J. Kumar, T. Nakashima, T. Kawai, *J. Phys. Chem. Lett.* **2015**, *6*, 3445–3452.

[42] T. Lummerstorfer, H. Hoffmann, *J. Phys. Chem. B* **2004**, *108*, 3963–3966.

[43] V. V. Rostovtsev, L. G. Green, V. V. Fokin, K. B. Sharpless, *Angew. Chem. Int. Ed.* **2002**, *41*, 2596–2599.

[44] J. E. Hein, V. V. Fokin, *Chem. Soc. Rev.* **2010**, *39*, 1302–1315.

[45] S. R. Raghavan, J. F. Douglas, *Soft Matter* **2012**, *8*, 8539–8546.

[46] J. Matraszek, N. Topnani, N. Vaupotič, H. Takezoe, J. Mieczkowski, D. Pociecha, E. Gorecka, *Angew. Chem. Int. Ed.* **2016**, *55*, 3468–3472.

[47] D. Chen, M.-S. Heberling, M. Nakata, L. E. Hough, J. E. Maclennan, M. A. Glaser, E. Korblova, D. M. Walba, J. Watanabe, N. A. Clark, *ChemPhysChem* **2012**, *13*, 155–159.

[48] K. Sivakumar, F. Xie, B. M. Cash, S. Long, H. N. Barnhill, Q. Wang, *Org. Lett.* **2004**, *6*, 4603–4606.

[49] "Maison de Louis Pasteur à Arbois - Publications de Louis Pasteur dans les Comptes rendus (1)," can be found under http://www.academie-sciences.fr/archivage_site/fondations/lp_publi.htm, **n.d.**

[50] L. E. Hough, M. Spannuth, M. Nakata, D. A. Coleman, C. D. Jones, G. Dantlgraber, C. Tschierske, J. Watanabe, E. Körblova, D. M. Walba, et al., *Science* **2009**, *325*, 452–456.

[51] M. Alaasar, M. Prehm, C. Tschierske, *Chem. – Eur. J.* **2016**, *22*, 6583–6597.

[52] D. Chen, Y. Shen, J. Aguero, E. Korblova, D. M. Walba, N. Kapernaum, F. Giesselmann, J. Watanabe, J. E. Maclennan, M. A. Glaser, et al., *ChemPhysChem* **2014**, *15*, 1502–1507.

[53] H. Nádasi, C. Lischka, W. Weissflog, I. Wirth, S. Diele, G. Pelzl, H. Kresse, *Mol. Cryst. Liq. Cryst.* **2003**, *399*, 69–84.

[54] J. Bernstein, *Polymorphism in Molecular Crystals*, Oxford University Press, **2007**.

[55] B. D. Hamilton, J.-M. Ha, M. A. Hillmyer, M. D. Ward, *Acc. Chem. Res.* **2012**, *45*, 414–423.

[56] Q. Jiang, M. D. Ward, *Chem. Soc. Rev.* **2014**, *43*, 2066–2079.

[57] M. D. Ward, *Isr. J. Chem.* **2017**, *57*, 82–92.

[58] S. H. Ryu, D. K. Yoon, *Liq. Cryst.* **2016**, *43*, 1951–1972.

[59] C. R. Martin, *Science* **1994**, *266*, 1961–1966.

[60] S. H. Ryu, H. Ahn, T. J. Shin, D. K. Yoon, *Liq. Cryst.* **2017**, *44*, 713–721.

[61] H. Kim, S. H. Ryu, M. Tuchband, T. J. Shin, E. Korblova, D. M. Walba, N. A. Clark, D. K. Yoon, *Sci. Adv.* **2017**, *3*, e1602102.

Appendix

Table of Compounds

Compound	Pg#
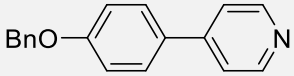	**39**
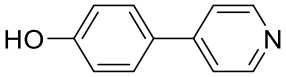	**39**
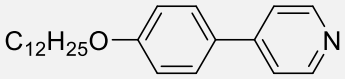	**40**
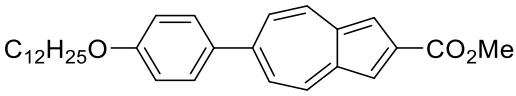	**41**
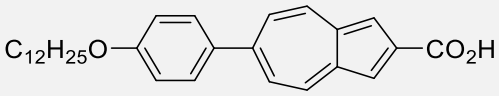	**42**
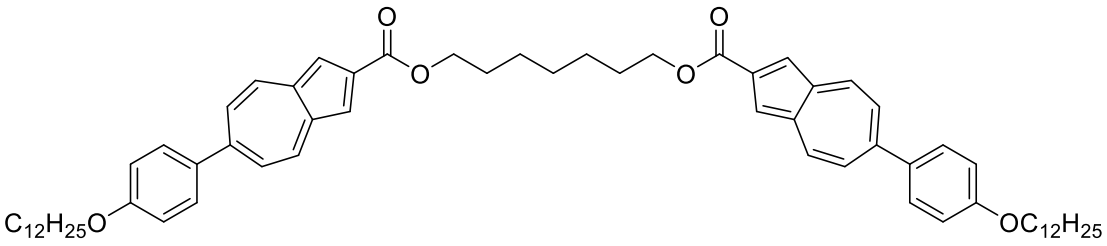	**42**
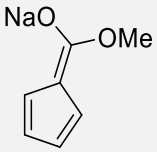	**43**
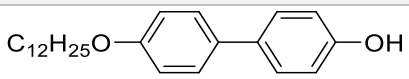	**44**
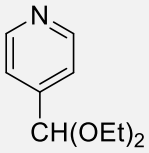	**44**

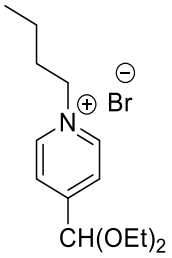	**45**
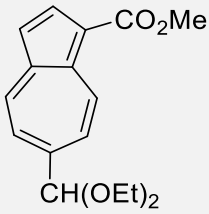	**45**
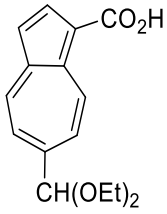	**46**
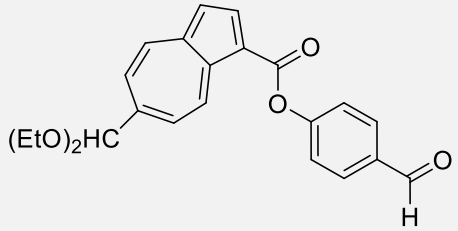	**47**
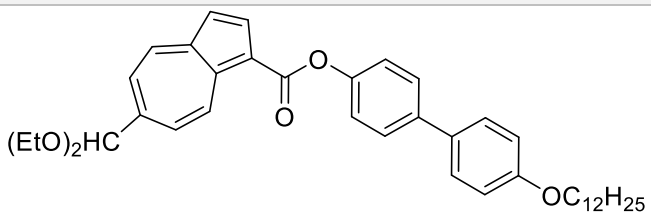	**47**
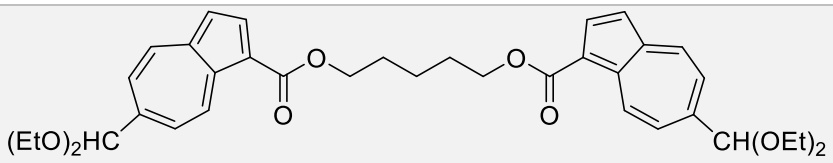	**48**
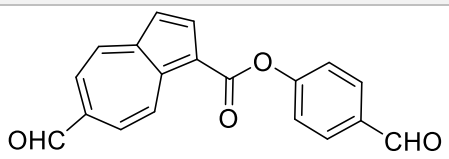	**49**

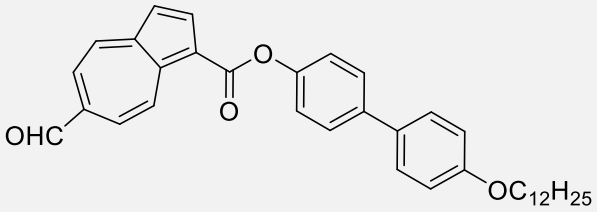	**49**
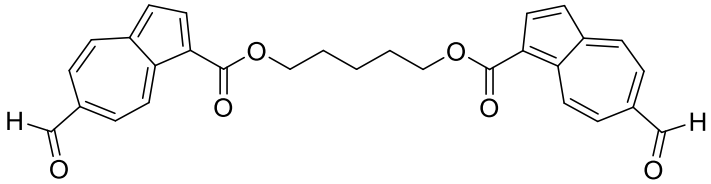	**50**
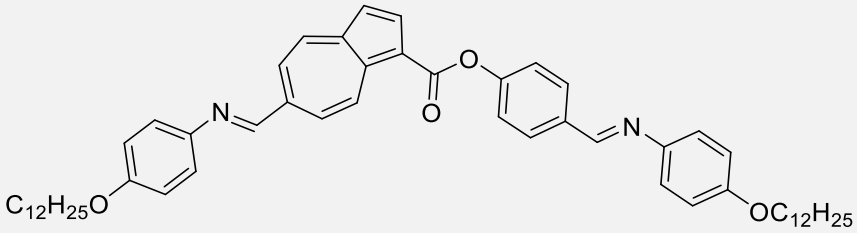	**50**
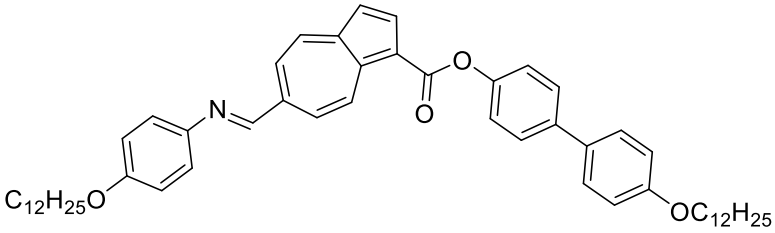	**51**
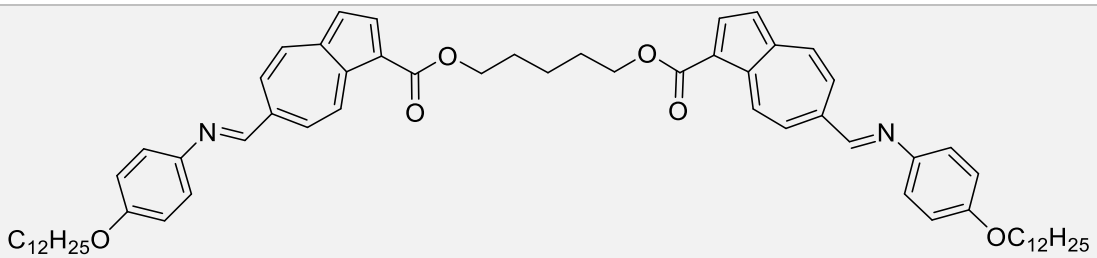	**52**
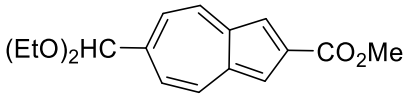	**53**
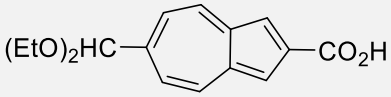	**53**
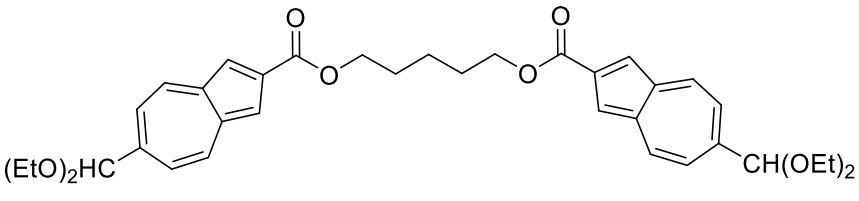	**54**

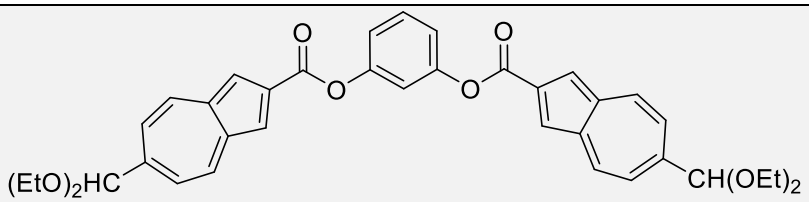	**55**
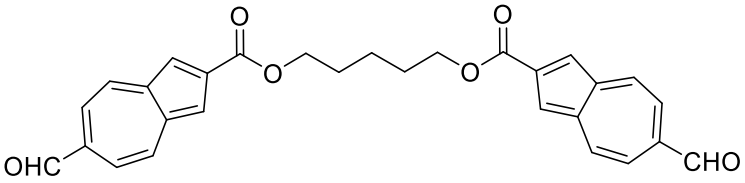	**55**
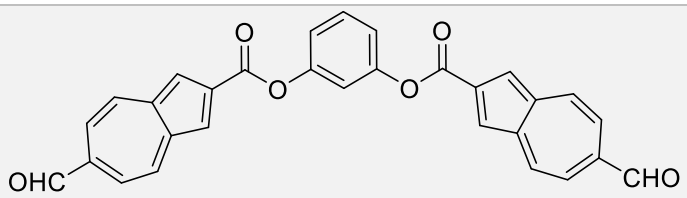	**56**
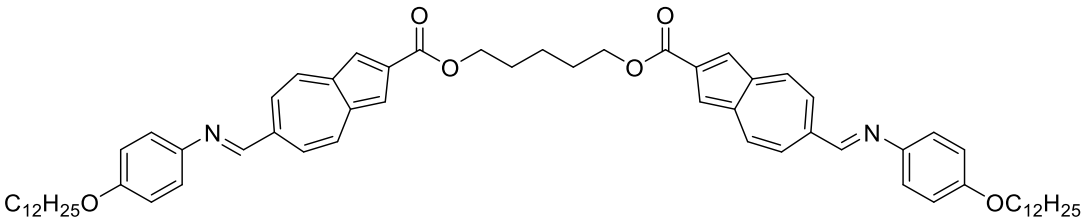	**56**
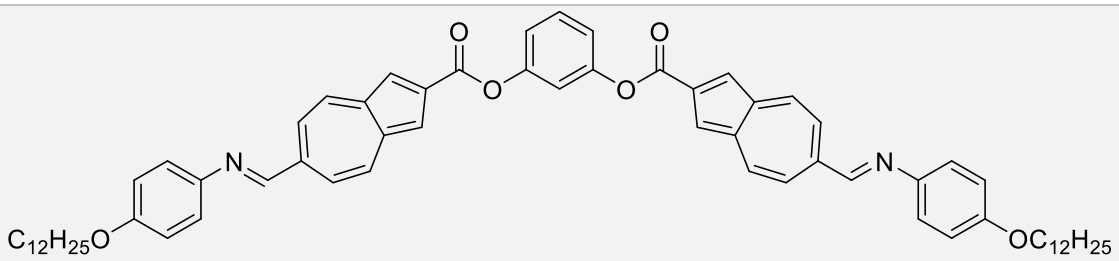	**57**
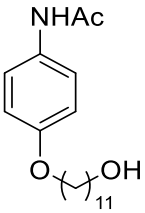	**81**
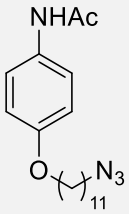	**81**

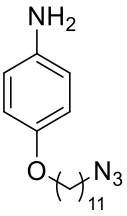	**82**
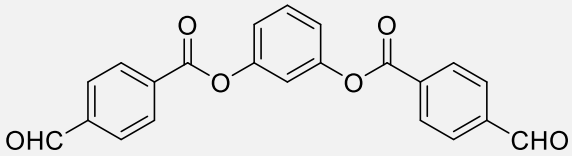	**83**
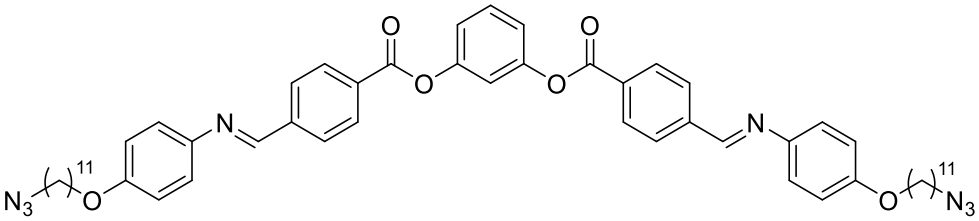	**83**
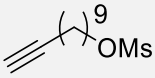	**84**
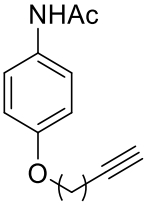	**84**
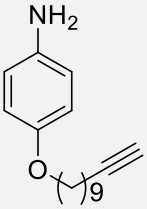	**85**
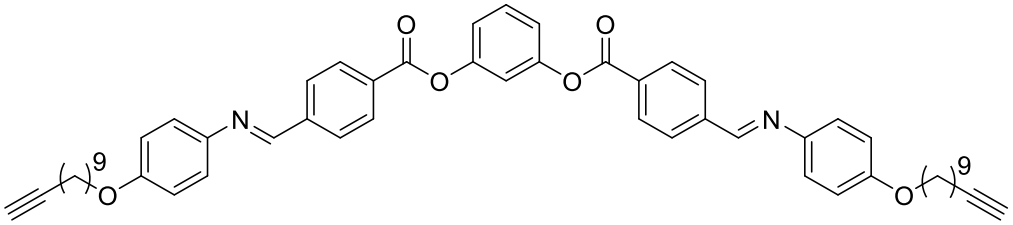	**86**

Azulene BLC Appendix

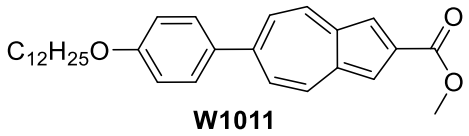

W1011

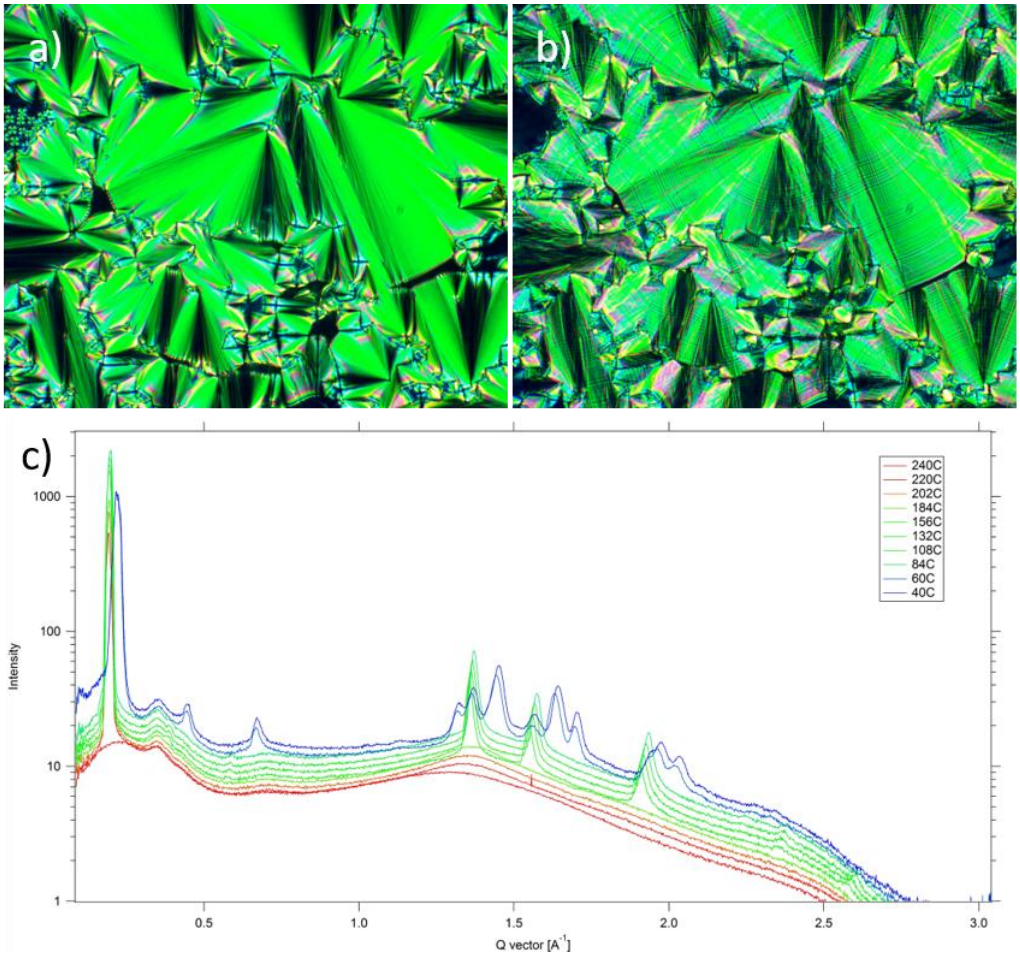

Figure 0.1 – POM and XRD data for W1011. a) The typical focal conic and batonette structure for the SmA phase was observed to grow in from the isotropic phase for W1011 at 220 °C. b) Further cooling led to the formation of stripes within the texture indicating the formation of in-plane ordering. This image was taken at 100 °C. c) The 1D plot of the XRD shows the layering peak for W1011 at approximately 0.2 $Å^{-1}$ corresponding to the molecular length. Continued cooling results in the formation of stripes in the wide-angle region indicating the formation of intralayer ordering. These results confirm the formation of the SmA and SmE phase for this material.

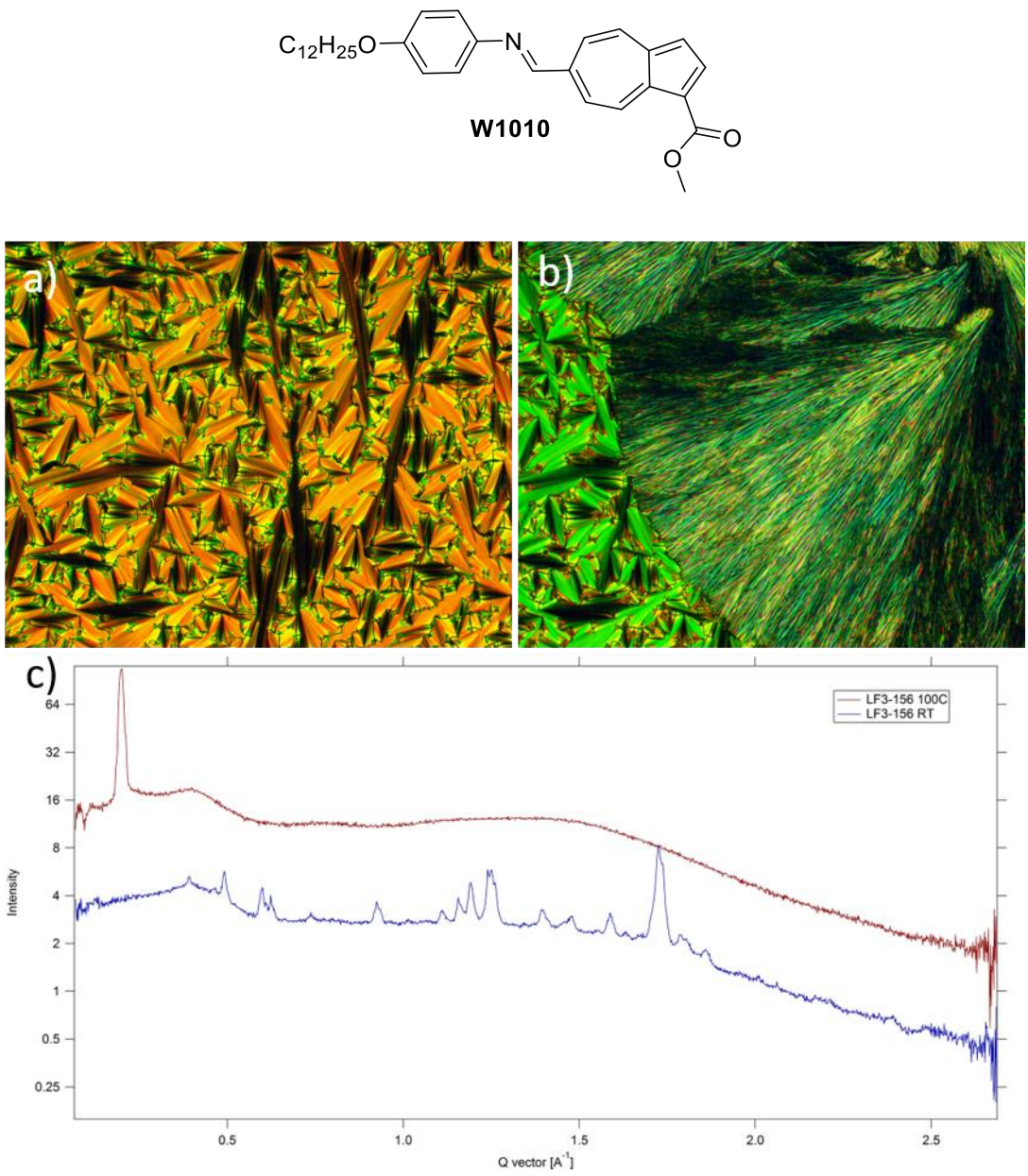

Figure 0.2 – POM and XRD data for W1010. a) Shows the formation of the SmA phase at 107 °C. b) Cooling further results in the formation of a glassy solid phase that grows in slowly over taking the SmA texture. c) The XRD plot shows the formation of the layer peak at 100 °C corresponding to the molecular length, indicating the formation of the SmA phase. Further cooling results in the loss of coherent layers with the formation of crystalline in-plane ordering, suggesting the formation of crystalline domains held in a glassy environment.

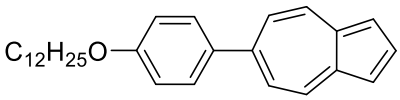

LF2-302

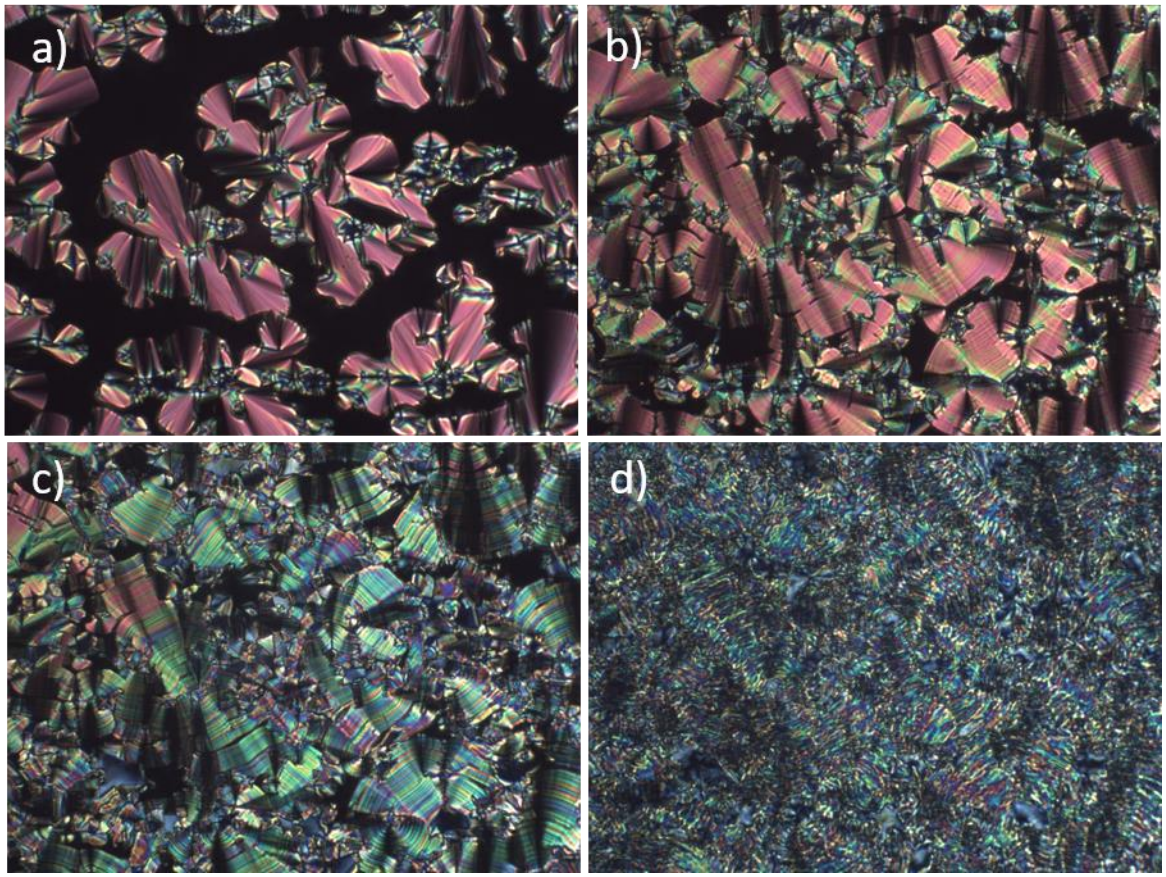

Figure 0.3 – POM images for LF2-302 showing the rich LC behavior of the material. a) Cooling from the isotropic results in the formation of a short lived SmA phase that quickly develops stripes possibly indicating the formation of the SmB phase. Further cooling results in the formation of more pronounced stripes along with a significant change in birefringence, suggesting the formation of the SmE phase. Finally, a broken, grainy texture is observed to quickly grow in indicating crystallization.

HNF Surface Functionalization Appendix

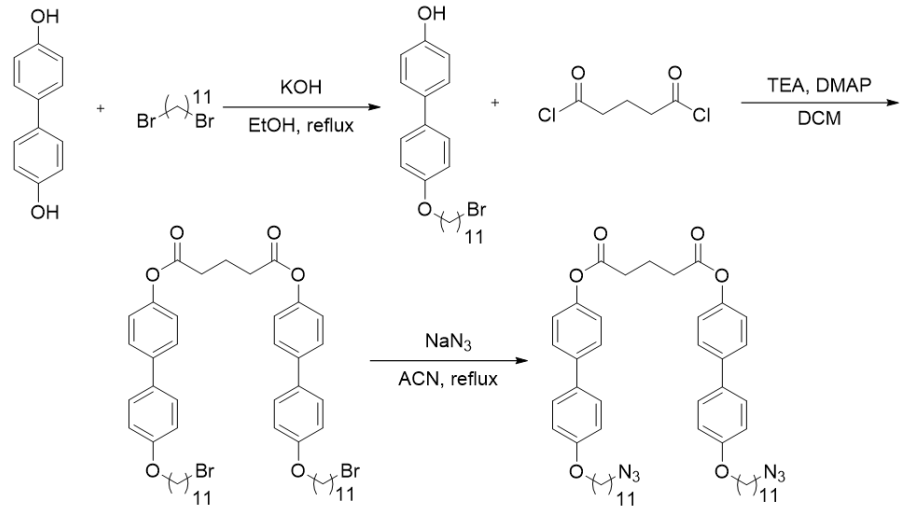

Figure 0.4 – Synthesis of LF3-069, the azide terminated version of Ewa Gorecka's HNF forming dimer molecule, for gel phase click reactions

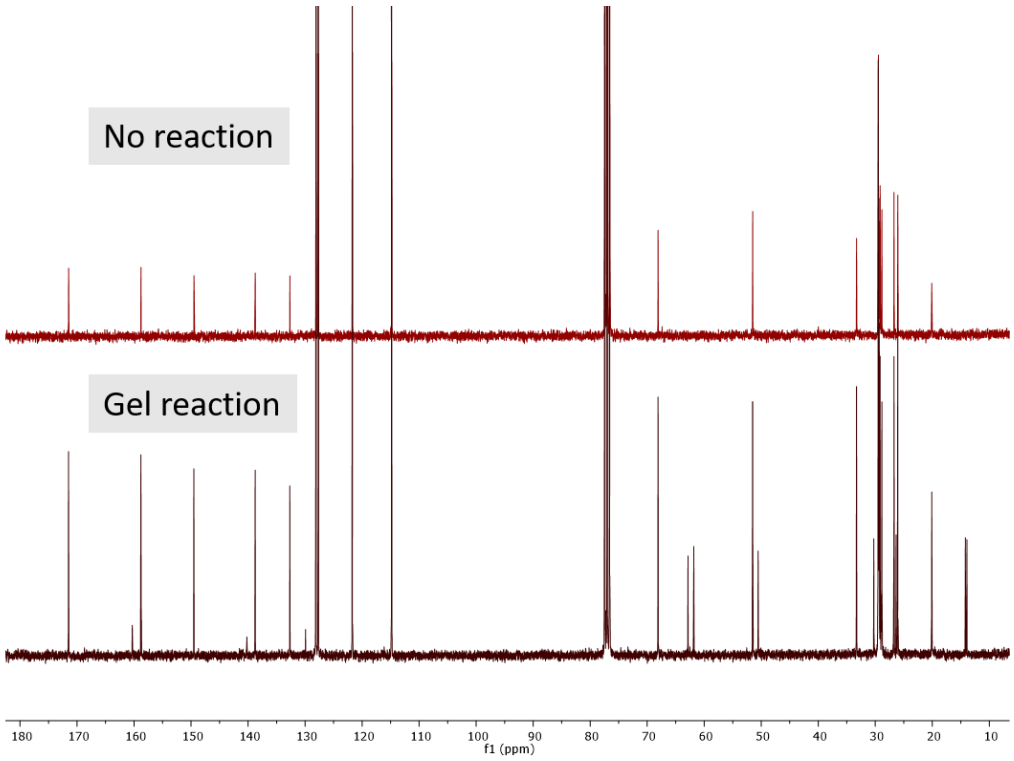

Figure 0.5 – ^{13}C NMR of LF3-069 before and after the gel phase reaction with DEAD.

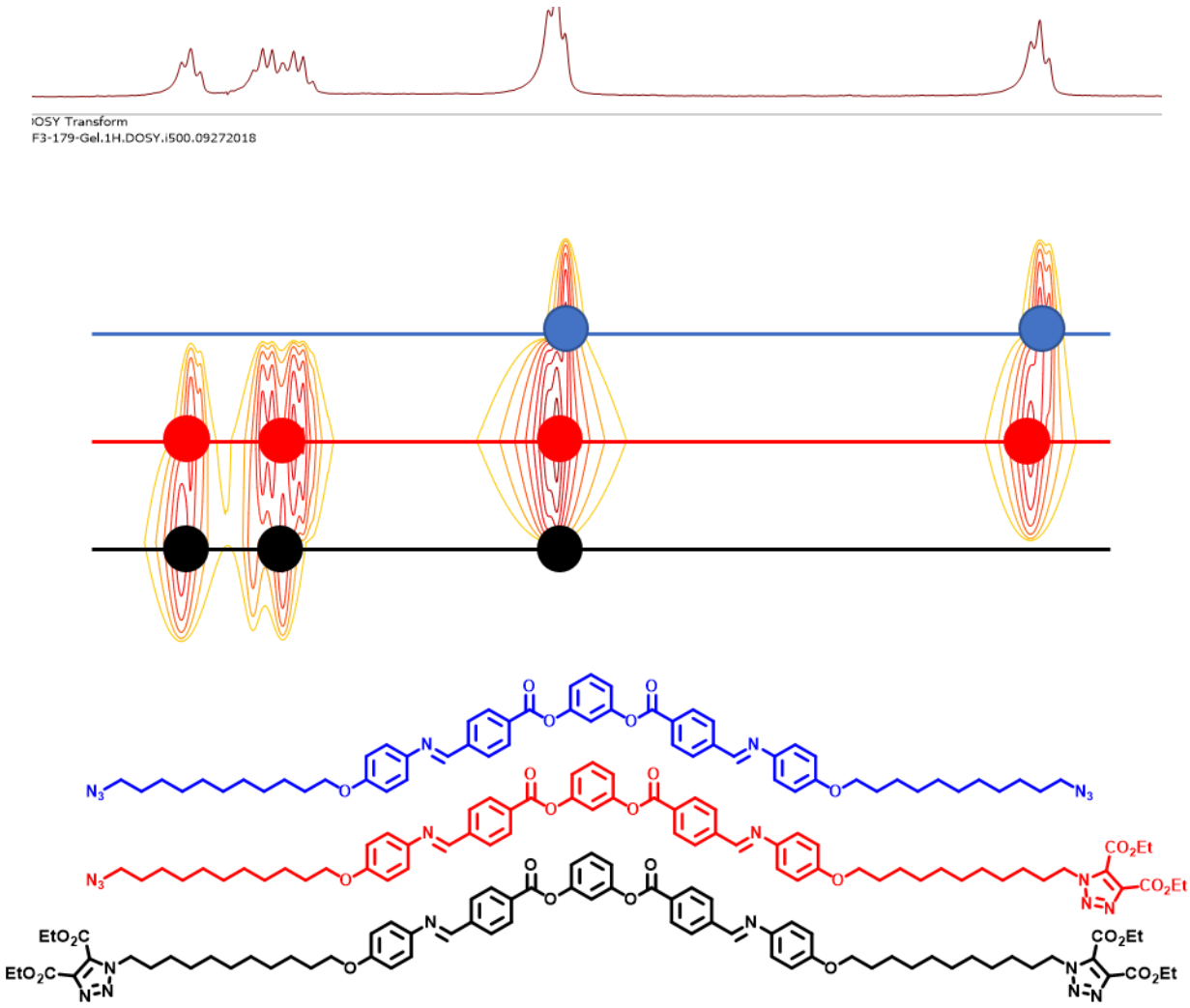

Figure 0.6 – Section of the DOSY spectrum obtained for a gel phase reaction showing the alkoxy, azido, and triazole methylene peaks. Three different sets of peaks are observed suggesting the presence of three different molecular species in solution.

Nanoconfinement of the Low temperature DC Appendix

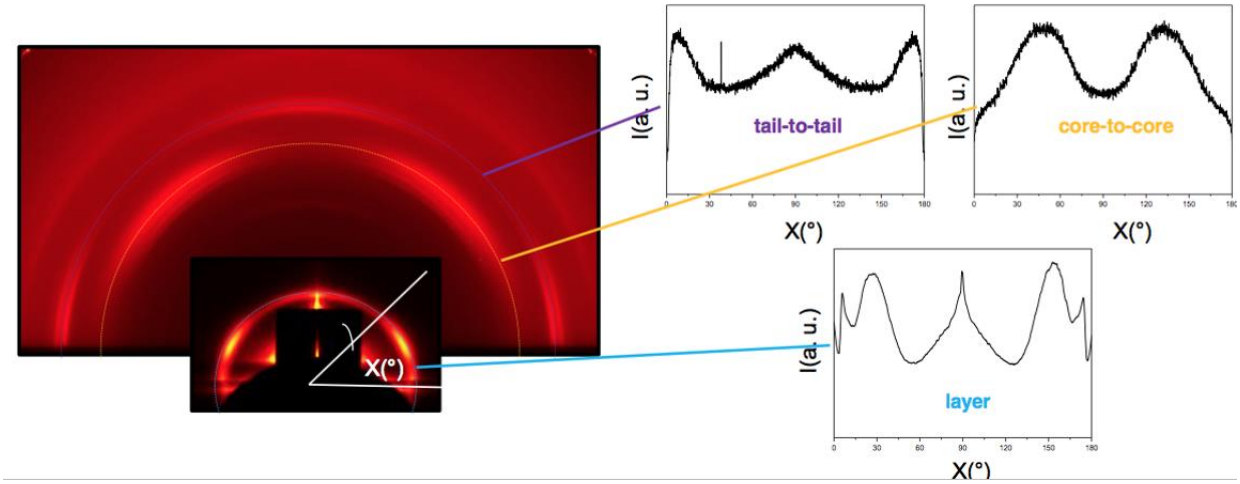

Figure 0.7 – GXRD data for P-12-OPIMB a material that shows coexistence of the HNF and DC phases. Nanoconfinement forces the material to adopt only the HNF in the pores.

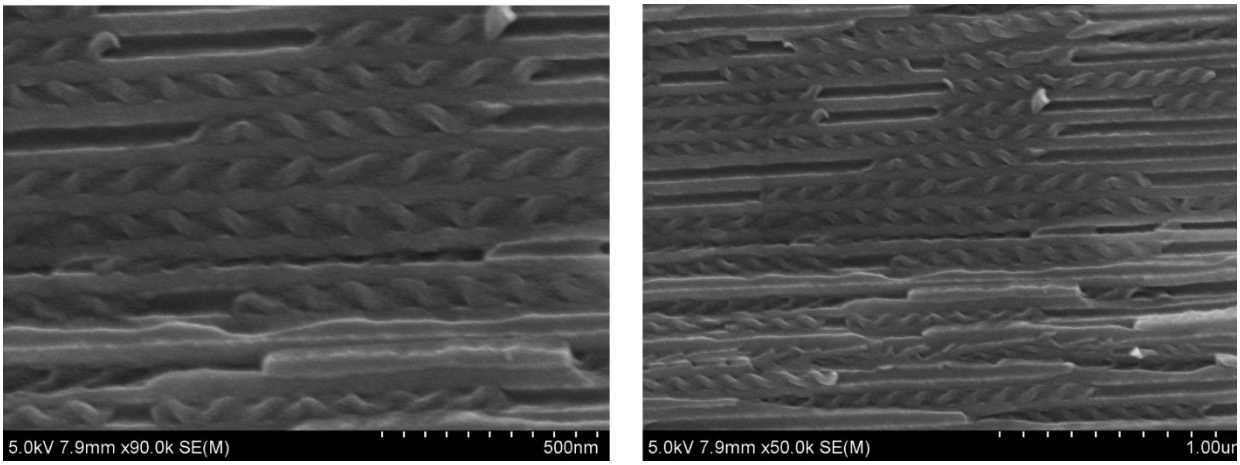

Figure 0.8 – SEM images of P-12-OPIMB in the 60 nm pores of AAO membranes. Both right and left handed filaments are observed to form in the absence of the DC phase